BERGISCHE
UNIVERSITÄT
WUPPERTAL

Improvements to gravity wave physics from an observational perspective

Dissertation

zur Erlangung des Grades
Doktor der Naturwissenschaften (Dr. rer. nat.)

von

Markus Geldenhuys

vorgelegt der

Bergischen Universität Wuppertal

Fakultät für Mathematik und Naturwissenschaften
Institut für Atmosphären und Umweltforschung

Abstract

Atmospheric gravity waves (GWs) are important for turbulence and for driving large-scale circulations in the mid to upper atmosphere. Global circulation models (weather and climate models) do not properly resolve part of the GW spectrum and therefore can not properly reproduce the atmospheric circulations. The models use parameterisation schemes in an attempt to capture the effect of the unresolved GWs. However, parameterisation schemes oversimplify the physical effects in the atmosphere and more complex theories are needed to describe the GWs more realistically. It is widely known that the GW drag amount and the location there-of are incorrect in the general circulation models. This dissertation relies on observations to better understand GWs, which leads to suggestions for improvements in general circulation models. Observations consist of GLORIA (Gimballed Limb Observer for Radiance Imaging of the Atmosphere) and ALIMA (Airborne LIdar for the Middle Atmosphere) instruments onboard the German High Altitude LOng range (HALO) research aircraft. This allows high-resolution measurements from about 5 km to 80 km.

Firstly, this work analysed the current orographic GW drag parameterisation schemes. The current schemes are shown to be inadequate in the vicinity of low-level blocking. In contrast to the current implementation, observational studies show that the GW drag amount should not be reduced in the presence of blocking.

Secondly, observations are used to show that horizontal refraction makes an important contribution to the GW drag location and amount. GWs interact with the background wind through refraction. Observational data were collected around the Andes and Drake Passage in the South-TRAC campaign on 12 September 2019. Refraction is identified in two different GW packets (one of orographic and one of non-orographic origin) as low as $\approx$4 km and as high as 58 km. Observations are supplemented by the Gravity-wave Regional Or Global Ray Tracer (GROGRAT) and high-resolution model data. Contrary to some previous studies it is shown that refraction makes a noteworthy contribution to the amount and the location of GW drag. This case study provides compelling arguments that models should account for refraction.

Thirdly, a new GW source mechanism is identified with the help of observations, GROGRAT and a numerical experiment. To better understand the impact of GWs on the middle atmosphere, it is essential to understand their excitation mechanisms. Here a new process for GW excitation by orography-jet interaction is identified, in a POLSTRACC case study over Greenland on 10 March 2016. The GW packet has a slow vertical group velocity, which causes the GW packet

to spread over a large area while remaining constrained to a narrow vertical layer. It is shown that flow over a broad ridge cause compression of air above Greenland. The orography modifies the wind flow and pushes the Coriolis and pressure gradient forces out of balance. The out of balance jet then excites GWs while bringing the flow back into balance. This is the first observational evidence of GW generation by such an orography-jet mechanism. The work presented here addresses three distinctly different issues in the GW community to improve the knowledge and the physics behind GWs.

Kurzfassung

Atmosphärische Schwerewellen sind wichtig für die Erzeugung von Turbulenz und für den Antrieb der großräumigen Zirkulation in der mittleren und oberen Atmosphäre. Globale Zirkulations-Modelle (Wetter- und Klimamodelle) lösen einen Teil des Schwerewelle-Spektrums nicht vollständig auf und können daher die atmosphärische Zirkulation nicht richtig wiedergeben. Die Modelle verwenden daher Parametrisierungen, um die Auswirkungen von nicht-aufgelösten Schwerewellen zu erfassen. Allerdings vereinfachen die existierenden Parametrisierungen die physikalischen Effekte in der Atmosphäre zu sehr, so dass komplexere Darstellungen erforderlich sind, um Schwerewellen genauer zu beschreiben. Es ist allgemein bekannt, dass weder die Magnitude noch der Wirkungsort des Windantriebes durch Schwerewellen in den allgemeinen Zirkulationsmodellen korrekt sind. Diese Dissertation stützt sich daher auf Beobachtungen, um Schwerewellen besser zu verstehen und daraus Vorschläge zur Verbesserung ihrer Darstellung in globalen Zirkulationsmodellen abzuleiten. Diese Beobachtungen wurden von den beiden Instrumenten GLORIA (Gimballed Limb Observer for Radiance Imaging of the Atmosphere) und ALIMA (Airborne LIdar for the Middle Atmosphere) an Bord des deutschen Forschungsflugzeugs HALO (High Altitude LOng range) durchgeführt. Dies ermöglicht hochauflösende Messungen im Höhenbereich von etwa 5 bis 80 km.

Zunächst wurden die derzeitigen Verfahren zur Parametrisierung des orographischen Windantriebs durch Schwerewellen analysiert. Es wurde gezeigt, dass die derzeitigen Verfahren in der Nähe von Low Level Blocking unzureichend sind. Im Gegensatz zur derzeitigen Modellierung zeigen Beobachtungsstudien, dass der Windantrieb durch Schwerewellen in der Nähe von Blocking nicht reduziert werden sollte.

Zweitens wird anhand von Beobachtungen gezeigt, dass die horizontale Refraktion einen wichtigen Beitrag zum Ort und zur Magnitude des Schwerewellen-Widerstands leistet. Schwerewellen interagieren mit dem Hintergrundwind durch Brechung. Die Beobachtungsdaten wurden im Rahmen der SouthTRAC-Kampagne am 12. September 2019 im Gebiet der Anden und der Drake-Passage gesammelt. Die Refraktion wird anhand zweier verschiedener Schwerewellen-Pakete, eines orographischen Pakets bei etwa 4 km Höhe und eines nicht-orographischen Pakets bei etwa 58 km Höhe untersucht. Die Beobachtungen werden durch den Gravity-wave Regional Or Global Ray Tracer (GROGRAT) und hochauflösende Modelldaten ergänzt. Im Gegensatz zu einigen früheren Studien wird gezeigt, dass die Refraktion einen deutlichen Beitrag zur Größe und zum Ort des Windantriebs durch Schwerewellen leistet. Diese Fallstudie liefert zwingende

Argumente dafür, dass Modelle Refraktion berücksichtigen sollten.

Drittens wird mit Hilfe von Beobachtungen, GROGRAT und einem numerischen Experiment ein neuer Schwerewellen-Quellmechanismus identifiziert. Um die Auswirkungen von Schwerewellen auf die mittlere Atmosphäre besser zu verstehen, ist es wichtig, ihre Anregungsmechanismen zu verstehen. Hier wird ein neuer Prozess zur Schwerewelle-Anregung durch Orographie-Jet-Wechselwirkung südlich von sowie über Grönland in einer POLSTRACC-Fallstudie für den 10. März 2016 identifiziert. Das Schwerewellen-Paket hat eine langsame vertikale Gruppengeschwindigkeit, die dazu führt, dass sich das Schwerewellen-Paket über ein großes Gebiet ausbreitet, während es vertikal auf eine schmale Schicht beschränkt bleibt. Es wird gezeigt, dass die Quelle eine Strömung über einem breiten Bergrücken über Grönland ist. Die Orographie komprimiert die Windströmung und bringt dadurch die Coriolis- und Druckgradientenkräfte aus dem Gleichgewicht. Der so aus dem Gleichgewicht geratene Jet regt dann Schwerewellen an, um die Strömung wieder ins Kräfte-Gleichgewicht zu bringen. Dies ist der erste Beobachtungsnachweis für die Erzeugung von Schwerewellen durch einen solchen kombinierten Orographie-Jet-Mechanismus. Zusammenfassend, werden in dieser Arbeit drei Aspekte der Schwerewellenphysik anhand neuartiger Messungen detailliert und ein besseres Verständnis der Anregung und Ausbreitung von Schwerewellen erreicht.

Contents

Chapter 1

Introduction

Waves have been of interest to humanity since the first Polynesians started surfing. However, waves are not only present in the ocean but also in the atmosphere. In 1853, George Cayley built the first successful glider plane (Crouch, n.d.). From then onward gravity waves (GWs) in the atmosphere have been surfed by glider planes. In fact, after being discovered by Wegener (1906) and Trey (1919), Küttner (1938) used a glider plane to conduct one of the first systematic scientific investigations of a mountain wave — a type of GW (Wildmann et al., 2021).

The most straightforward example of a GW is a wave excited by a mountain. Airflow in mountainous terrain can take multiple patterns. Flow with little momentum is blocked by the orography and forms a strong low-level wind (called a blocking jet) blowing along the mountain ridge. Airflow with sufficient momentum to ascend the orography will excite a propagating mountain wave (Fig. 1.1). At the top of the mountain, the parcel is colder and denser than its environment and gravity pulls it down, completing the full wavelength of the GW (trough to trough). A gravity wave is excited when an air parcel is more (or less) dense than its surrounding environment and is returned to the equilibrium point and deflected beyond it due to its inertia.

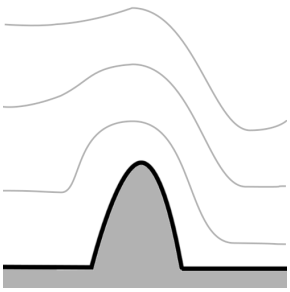

Figure 1.1: A GW excited over orography. The grey filled region represent topography, the thin solid lines represents lines of equal potential temperature showing the atmospheric wave.

Upon excitation, the GW takes energy from the background flow. This results in GW momentum flux (GWMF), which is transported with the GW until it dissipates or breaks. A breaking GW is characterised by regular, non-turbulent flow turning into turbulence, whereby the energy is transferred to heat (Zhou et al., 2002). A GW propagating against the wind will slow down (or sometimes speed up) the background wind upon dissipation — called GW drag. This slow down in the wind will trigger a small force perpendicular to the mean flow which acts to drive large-scale atmospheric circulations in the stratosphere and mesosphere (Alexander and Rosenlof, 1996). Gravity waves impact us through the production of turbulence (Fritts and Alexander, 2003; Bramberger et al., 2018; Geldenhuys et al., 2019), atmospheric mixing (Holton, 2004), affecting the ozone hole, inducing drag to change the movement speed of weather systems and driving circulations in the stratosphere and mesosphere (Kidston et al., 2015).

Society heavily relies on meteorological forecasts generated by computerised atmospheric models, which simulate atmospheric circulations. An atmospheric general circulation model solves equations according to the conservation laws of physics to predict a future state (AMS, 2018). The time evolution of the model is achieved by integrating the governing equations with respect to time and starting from an initial condition — yesterday's weather. Most general circulation models solve the equations on a defined 3-D grid (e.g. latitude, longitude, altitude), this grid spacing defines the model resolution. Due to the complex nature of the atmosphere and due to limited computation capacity the achievable resolution is still too coarse to properly represent all relevant processes. Adding the effect of these unresolved processes back into the simulation requires the creation of parameterisation schemes. Parameterisation schemes are a sort of sub-model which oversimplify the physical effects in the atmosphere that can not be resolved in the model. Communication between model grid points (in the latitude and longitude direction) breaks the parallelisation and takes computation time, thus, parameterisation schemes in current weather and climate models are applied column-wise (with altitude) to minimise this communication and hence minimise computation time.

General circulation models require GW drag to drive mid-atmospheric circulations despite not resolving all GWs due to resolution constraints. Thus, models need to use parameterisation schemes to add, to the simulation, the missing GW drag required to drive the circulations. State-of-the-art GW model parameterisations are divided into orographic GW drag (OGWD) and non-orographic GW drag (NOGWD) schemes. The OGWD scheme represents the drag exerted by waves from mountains alone (Lott and Miller, 1997; Kim and Arakawa, 1995; Xie et al., 2020).

The NOGWD scheme is a generalised and simplified scheme and developed to represent all other sources (e.g. Charron and Manzini, 2002; de la Camara et al., 2014a), for example, fronts, convection, jet streams, inertial instabilities, wind shear, GW breaking, etc. The fact that all non-topographical GW sources are combined into one parameterisation, which launches a constant and uniform GW drag globally (ECMWF, 2015) highlights the non-physical nature of the scheme.

Literature suggests that two of the largest shortcomings of GW parameterisation schemes in general are the fact that it produces drag in a single column (Lott and Miller, 1997) (due to keeping the implementation efficient) and the drag can only decrease with altitude as a result of oversimplified physics (ECMWF, 2015). In reality, GWs can propagate for 100's or even 1000's of kilometres horizontally, making the single-column approach at best an improvement of the model representation of dynamics but not representing reality. During its propagation the GW orientation can change (called refraction), whereby changes in the wavelength in the x- and y-direction (Durran, 2009) occur. When GWs are such refracted they exchange momentum with the background flow, which would influence background winds at a different place than the interaction via breaking (Buehler and McIntyre, 2003). However, some studies (e.g. Hasha et al., 2008; Preusse et al., 2009) argue the effect of refraction is not noteworthy. Hasha et al. (2008) goes further in saying that meridional propagation is also negligible. Both of these studies used a very coarse resolution and the realistic nature of this has not been evaluated for refraction. Literature states that the importance of refraction is that GWs are refracted into the vortex and thus a focusing effect is generated (Sato et al., 2009). This contributes to a general tendency for lateral propagation (Jiang et al., 2004; Sato et al., 2009). The GW orientation (Strube et al., 2021) and lateral propagation allows GWs to avoid critical layers (Preusse et al., 2009; Kalisch et al., 2014) and GWs thus can reach regions where they otherwise would be filtered at lower altitudes. Up to now literature has only provided indirect proof of refraction, but direct observational evidence for GW refraction is still missing. During the lifetime of a GW, refraction can affect its GWMF, the GW can be modulated by the air blocked by the mountain or it can exchange energy with other waves; none of these effects are included in the oversimplified physics of current conventional parameterisation schemes.

The large number of assumptions in the parameterisation schemes make GWs a large source of uncertainty in general circulation models. This uncertainty affects seasonal predictions (Scaife et al., 2016), climate projections (Sandu et al., 2016) and ozone hole predictions (Alexander and Barnet, 2007; Garcia et al., 2017). One method of improving parameterisation schemes in models is by finding better constraints for the model parameters by observations (e.g Plougonven et al.,

2020).

Direct observational evidence for the relative importance of different GW sources is rare. Hence, often the effect on the atmospheric circulation is used to infer properties on the nature of GWs and their parameterisations (Manzini et al., 1997). A good example is a recent debate on the question, which shortcomings in the GW physics are responsible for the missing GW drag around the latitude circle 60° S (McLandress et al., 2012).

McLandress et al. (2012) found that the model winds are too strong at the polar vortex located at 10 hPa and 60° S. They attributed this to the model having an inadequate amount of GW drag. This sparked several studies aimed at finding the missing GW drag, all of which came up with a different solution. McLandress et al. (2012) theorised the solution to the missing drag can be meridional (northwards-southwards) GW propagation. de la Camara et al. (2016) found that the sporadic nature (called intermittency) of their NOGWD parameterisation scheme solves the 60° S problem. Garcia et al. (2017) suggested that increased topographical sources are the key to solving the missing GW drag in models. On the other hand, Garcia et al. (2017) did state that NOGWD can also be a solution. The European Centre for Medium-Range Weather Forecasts (ECMWF) employed a stronger NOGWD with favourable results (Polichtchouk et al., 2018b). Moreover, Charron and Manzini (2002) showed that increased GW emission from cold fronts provides good results in the Northern Hemisphere, but are less effective in the Southern Hemisphere. Later, Richter et al. (2010) confirmed this by increasing convective and frontal GW sources. Clearly attempts to improve on the realism and employ physical GW sources (Richter et al., 2010; Kim et al., 2013) or mimic natural non-orographic GW source intermittency (de la Camara et al., 2014b) are still experimental to date. The main concerns are that such parameterisations use their own assumptions and adjustable parameters, which are only weakly constrained by observations. Charron and Manzini (2002), Richter et al. (2010) and Kim et al. (2013) all agree that the trend is toward replacing NOGWD parameterisation schemes by source-specific schemes. Since Charron and Manzini (2002) stated that no global GW source climatology exists, a lot of progress is still required to address this GW uncertainty observationally.

Observational evidence of GWs is required to guide parameterisation schemes (Richter et al., 2010; Plougonven et al., 2020) and improve our understanding of the underlying physics. Many GW observation methods exist, namely glider planes (Grubisic and Lewis, 2004; Rapp et al., 2021; Wildmann et al., 2021), radiosondes (Guest et al., 2000; Geldenhuys et al., 2019), dropsondes (Koch et al., 2005), lidars (Doyle et al., 2009; Reichert et al., 2019), radars (Doyle et al.,

2009; Reichert et al., 2019), airglow imagers (Reichert et al., 2019), superpressure balloons (Hertzog et al., 2008), satellites (Ern et al., 2004, 2006; Orr et al., 2010; Ern et al., 2016), aircraft based in-situ measurements (Doyle et al., 2009; Mallaun et al., 2015), and limb imagers (Krisch et al., 2017). Of all the above mentioned methods, only radar, and limb imagers provide 3-D data — which is required to fully characterise a GW. For non-3-D observational datasets, some part of the GW characteristics needs to be assumed or inferred via equations (Krisch, 2018). This dissertation will use and combine data from the ALIMA lidar (Rapp et al., 2021) and the GLORIA limb imager (Gimballed Limb Observer for Radiance Imaging of the Atmosphere (Friedl-Vallon et al., 2014; Riese et al., 2014)).

GLORIA is an infrared limb sounder that is flown on the German research aircraft HALO (High Altitude LOng range). GLORIA retrievals provide a high-resolution 3-D dataset. Placed on an aircraft the measurements can be taken to the desired locations for the observation, as opposed to satellites and ground-based radars whose observation location is predetermined. GLORIA is situated in the belly pod of HALO and only measures during campaigns. Both campaigns discussed in this dissertation had GLORIA onboard HALO — GLORIA is discussed in detail in Chapter 4 and the campaigns in Chapter 5 and 6. During SouthTRAC, ALIMA (Airborne LIdar for the Middle Atmosphere — discussed in detail in Chapter 4) was also mounted on HALO. ALIMA is an upwards looking iron resonance and Rayleigh lidar. ALIMA measures from 2 km above flight altitude to 80 km. Combined, the two instruments provide a data coverage throughout the atmosphere from 5 km to 80 km altitude; GLORIA below flight altitude and ALIMA above flight altitude. In this dissertation, the complexities of GWs from an observational point of view is examined to improve the knowledge base of GW physics. In this dissertation we gain process understanding that is currently being implemented into a model parameterisation scheme in a project in the framework of the BMBF priority programme ROMIC (Role if the Middle Atmosphere in Climate), which focuses on SouthTRAC. Thus, the results from this dissertation make contributions to GW knowledge which can be implemented in models.

Literature (summarised from above) states that to improve the knowledge base of GW physics we need to look at the following key points:

1. Models require more GW drag
    1.1. More OGWD is required (Garcia et al., 2017)
    1.2. More NOGWD is required (Charron and Manzini, 2002; Richter et al., 2010; Polichtchouk et al., 2018b)

2. McLandress et al. (2012) speculate models require meridional propagation, while literature disagrees whether refraction is important for the amount and location of GWMF deposition (Durran, 2009)

3. Observations of GWs and its sources are required (e.g Plougonven et al., 2020).

This dissertation aims to improve the knowledge of GW physics by addressing the key points listed above. The improved knowledge can be used to make recommendations to improve GW physics in atmospheric models. This aim is achieved by the following objectives:

- **Objective 1: Analyse the orographic GW physics employed in the models in the vicinity of low-level blocking.** Models reduce the GWMF exponentially depending on the depth of the blocking jet (Geldenhuys, 2022). This can result in zero GWMF in some cases. However, some observational studies show that the blocking jet simply acts as an extension of the barrier and that wind will still pass over the barrier, favouring the formation of GWs. To achieve this objective the equations governing the orographic GW drag parameterisations are studied and the realism of it evaluated. This objective addresses key point 1.1 and is discussed in Chapter 3 (see also Geldenhuys, 2022).

- **Objective 2: Investigate meridional propagation and the effect of refraction through a case study.** Literature is divided on the impact of meridional propagation and refraction. Hasha et al. (2008) found that meridional propagation and refraction does not make a noteworthy contribution and current GW physics in the models are adequate. Durran (2009) criticised the study by Hasha et al. (2008) saying that under certain conditions refraction will make a noteworthy contribution to GWMF, but the effect will probably average out over time. Other studies like Sato et al. (2009) and Ehard et al. (2017) have shown that refraction can be important for meridional propagation and affects the location of GWMF deposition. Studies like (e.g. Preusse et al., 2009; Kalisch et al., 2014; Strube et al., 2021) found the orientation (and hence refraction) is important for GW filtering. However, no observational study has looked at the effect refraction has on GWMF. Chapter 5 (see also Geldenhuys et al., 2022) use high-resolution SouthTRAC observations to characterise refraction and determine the effect there-of. This chapter address key points 1, 2 and 3.

- **Objective 3: Investigate key points 1.2, 2 and 3 by use of observations from a non-orographic GW case study with an unknown source.** Observations are very important to compare to model results. Studies have shown that GWs in the model are very dependent

on model characteristics, for example, its resolution (Lane and Knievel, 2005). For reasons like this, observations are of the utmost importance. Even more important for the community is to obtain knowledge of specific GW sources. Without knowledge of GW sources, the source can not be included in GW physics. The results from this objective identified a new GW source combination, which is discussed in Chapter 6 (see also Geldenhuys et al., 2021).

Chapter 2 includes an in-depth overview of our knowledge of the lifecycle of GWs and its sources. Chapter 3 heavily relies on past literature and apply this in a new way to address Objective 1. Hence, for a natural flow, Chapter 3 follows the GW lifecycle overview chapter. In Chapter 4 observational campaigns, instruments, tools for analysis and model data are discussed. Chapter 5 discusses Objective 2 and Chapter 6 discusses Objective 3. The final chapter (Chapter 7) consist of a summary and the contributions to science originating from this dissertation.

Chapter 2

The Gravity Wave lifecycle

This chapter discusses gravity wave (GW) theory and the equations that governs GW existence. Figure 2.1 is used to summarise the lifecycle of a GW, each shape forms a section in the chapter and the figure can be used to navigate the chapter. The lifecycle of a GW can be grouped into different stages, namely *excitation*, *growth* and *dissipation*. The GW can propagate freely in the growing and partial dissipation stages. Refraction can constantly affect the GW during propagation by contributing to growth or dissipation. The discussion of refraction is deferred to Chapter 5. When a GW dissipates it can excite a new GW (secondary GW), forming a complete cycle which renews itself.

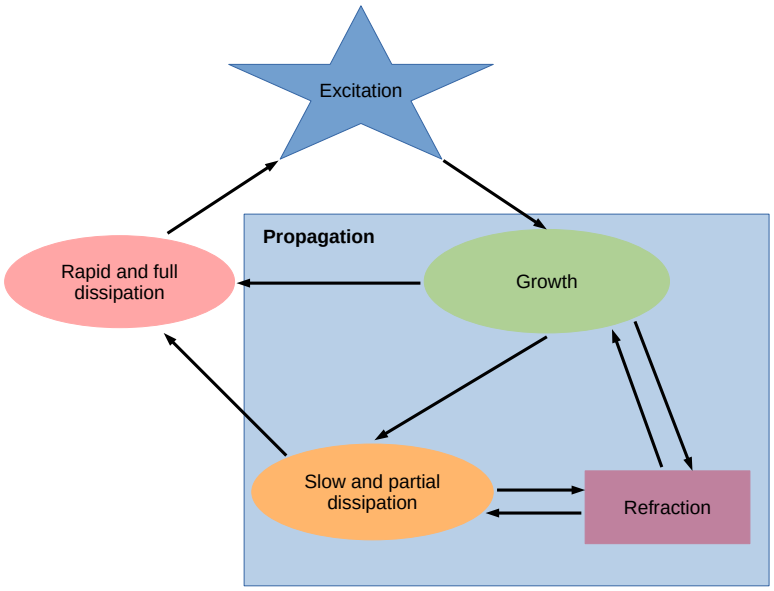

Figure 2.1: The lifecycle of a GW from excitation to dissipation.

2.1 GW excitation

Atmospheric GWs are waves that take shape with buoyancy acting as the restoring force (Fritts and Alexander, 2003). An air parcel with a different density than its surrounding tends to return to its level of neutral buoyancy (Fig. 1.1). Its neutral buoyancy position is the first location it can reach where the environment has the same density as the parcel before displacement. The parcel temperature and pressure determines its density via the ideal gas law:

$$\rho = \frac{p}{RT}, \tag{2.1}$$

where ρ is the density, p is the pressure and R is the gas constant for a dry (286.9 J kg^{-1} K^{-1}) or moist (461.4 J kg^{-1} K^{-1}) air. An environmental temperature gradient smaller than the moist adiabatic temperature gradient represent a stable atmosphere. In a stable atmosphere, a displaced parcel will move vertically to reach a state where its density is the same as its surroundings. During this vertical movement a GW is formed. Frequently GWs take shape in response to an external forcing (Fritts and Alexander, 2003; Dunlop, 2012), but certain sources (e.g. the jet or katabatic winds) do not require this external forcing. An unstable environment can't contain GWs as described by linear theory. If a parcel moves upward in an unstable atmosphere, it will continue to rise and buoyancy will not act to force the parcel down.

Gravity waves are emitted in the troposphere by flow over orography (e.g. Bacmeister et al., 1994; Eckermann and Preusse, 1999; Durran, 2003; Geldenhuys et al., 2019), katabatic winds (Yu and Cai, 2006; Watanabe et al., 2006; Vignon et al., 2020), convection (Pfister et al., 1993; Alexander and Pfister, 1995; Chun and Baik, 1998; McLandress et al., 2000; Beres et al., 2004; Choi et al., 2012; Trinh et al., 2016) and fronts (Snyder et al., 1993; Ralph et al., 1999; Charron and Manzini, 2002). Other sources, such as an out-of-balance jet (O'Sullivan and Dunkerton, 1995; Zülicke and Peters, 2006; Plougonven and Zhang, 2014), wind shear (Lott, 1997), inertial instabilities (Rowe and Hitchman, 2015) and a planetary wave induced critical layer in the polar vortex (Polichtchouk and Scott, 2020) occur both in the troposphere and middle atmosphere. Secondary wave generation from breaking GWs (Vadas and Fritts, 2002; Vadas and Becker, 2019; Heale et al., 2020) is another possible source of GWs throughout the atmosphere.

2.1.1 Types of GWs

Following excitation, a GW has several characteristics that defines the wave. GWs are described by their wavevector, intrinsic[1] frequency and by their wavenumber in the x, y, z -directions which are k, l, m, where wavenumber:

$$\text{wavenumber} = \frac{2\pi}{\text{wavelength}}. \tag{2.2}$$

The wavevector points perpendicularly to the GW phase orientation — it can be both in the direction of or against the wind. The magnitude of the GW wavevector is determined by the phase speed. The phase speed of a GW in a Eulerian system is described by (Marks and Eckermann, 1995):

$$\frac{dx}{dt} = C_{gb_x} = u + \frac{k(N^2 - \hat{\omega}^2)}{\hat{\omega}(k^2 + l^2 + m^2 + \frac{1}{4H^2})}, \tag{2.3}$$

$$\frac{dy}{dt} = C_{gb_y} = v + \frac{l(N^2 - \hat{\omega}^2)}{\hat{\omega}(k^2 + l^2 + m^2 + \frac{1}{4H^2})}, \tag{2.4}$$

$$\frac{dz}{dt} = C_z = -\frac{m(\hat{\omega}^2 - f^2)}{\hat{\omega}(k^2 + l^2 + m^2 + \frac{1}{4H^2})}, \tag{2.5}$$

where C is the group speed and $_{gb}$ indicate with respect to the ground. Finally, GWs are often classified according to their intrinsic frequency:

$$\hat{\omega}^2 = \frac{(k^2 + l^2)N^2 + f^2(m^2 + \frac{1}{4H^2})}{k^2 + l^2 + m^2 + \frac{1}{4H^2}}. \tag{2.6}$$

Where f is the Coriolis parameter:

$$f = 2\Omega \sin\phi. \tag{2.7}$$

Ω is the angular velocity of Earth ($7.292 \times 10^{-5}\,\text{rad}\,\text{s}^{-1}$), ϕ is the latitude, H is the density height

[1] as seen by an observer moving with the background wind

scale, N the Brünt-Väisälä frequency (Holton, 2004):

$$N = \sqrt{\frac{g}{\bar{\theta}} \frac{\partial \theta}{\partial z}}, \tag{2.8}$$

g is the gravitational acceleration at 9.8 m s^{-1} and $\bar{\theta}$ is the layer averaged potential temperature ($\theta = T \frac{1000}{p}^{\frac{R}{C_p}}$). A literature overview reveals GW types like low-, mid- and high-frequency GWs, stationary GWs, trapped GWs, evanescent GWs, horizontally propagating GWs, and vertically propagating GWs.

Trapped GWs — Reflective, critical and turning layers

A critical layer, turning layer and reflective layer all restrict upward GW propagation. This can prevent proper measurement of the GW or prevent the GW from reaching higher altitudes (for the case in Chapter 6) where it has a more pronounced impact. The effect of all three layers are similar, but the processes are distinctly different. A critical layer exists when the horizontal ground-based group velocity (obtained by combining Eqs 2.3 and 2.4) of the GW approaches the background wind speed projected along the wavevector (Huang et al., 2010). Once this happens the intrinsic frequency approaches zero and the vertical wavenumber approaches infinity. Longer horizontal wavelengths correspond to a GW with a faster phase speed (and thus approach the background wind speed earlier) and will be more readily affected by critical layers. Short horizontal wavelengths correspond to a GW with a slower phase speed, which is usually far below the wind speed. For this reason a critical layer affects short horizontal wavelength GWs more rarely in the stratosphere.

Turning layers mainly reflect GWs with short horizontal wavelengths (Preusse et al., 2008). Reflected and trapped GWs occur when a GW is flanked by two lower stability regions (e.g. Durran, 2003; Van der Mescht, 2013; Geldenhuys, 2018). A turning layer is identified by assuming GWs are reflected where m^2 approaches 0 (Preusse et al., 2008). By this, the horizontal critical wavelength can be calculated where GWs will be reflected. This approach uses GW characteristics and stability to diagnose trapping. This method is useful as it directly uses GW characteristics, but it does not consider the background wind shear.

Stability and wind layers in the atmosphere act to reflect and trap GWs below a layer. Trapped GWs lose very little energy and can form a wave train that extends 100's of kilometres downwind.

A reflective layer is diagnosed by using the background stability and wind to determine the Scorer parameter (Durran, 2003):

$$\text{Scorer}^2 = \frac{N^2}{\bar{U}^2} - \frac{1}{\bar{U}}\frac{\partial^2 \bar{U}}{\partial z^2}, \tag{2.9}$$

where $\bar{U}$ is the wind perpendicular to the GW phase fronts and z is the altitude.

A general decrease in the Scorer parameter with altitude indicates that some part of the GW spectrum will be reflected (Durran, 2003). A trapped GW will satisfy: $Scorer_L > k > Scorer_U$ (where $Scorer_L$ and $Scorer_U$ denote Scorer of the lower layer and Scorer of the upper layer respectively). This means if wavenumber $k > Scorer$ then the GW would propagate through the layer and become a vertical propagating GW. If wavenumber $k < Scorer$ then that part of the GW spectrum is reflected and become a trapped/reflected GW.

Following reflection, an upward propagating GW will propagate downwards. The superposition of the downward propagating and the still upward propagating GWs will form a wave with vertical phase lines (Holton, 2004) or a chequerboard pattern. A GW with a single reflecting layer at the top is called a reflected GW, while a GW with a reflecting layer above and below is called a ducted GW. Reflected GWs have mainly been studied for turbulence applications and were generally regarded as unimportant for middle atmosphere dynamics (Fritts and Alexander, 2003). However, recent studies have found that not all the energy is trapped and some energy passes through the reflected layer (Huang et al., 2010; Mixa et al., 2021). For the reflected part of the spectrum, the energy that pass through the reflective layer form a wave which is called an **evanescent GW** (Fritts and Alexander, 2003). Evanescent GWs are known to have vertical phase fronts with altitude and transmit GW energy in the vertical. The upward transmission of GW energy in the evanescent region is called GW tunnelling (Mixa et al., 2021).

Stationary GWs

Mountain waves which do not meet a reflective layer is known to be an upward propagating, but horizontally stationary GW (an example of these GWs are observed and discussed in Chapter 5). Once a GW is excited it has a phase speed in the direction of the wavevector. Most frequently the GW phase speed points into the wind. Once the GW intrinsic phase speed matches the wind speed with an opposite sign, the groundbased phase speed becomes zero and the wave is called stationary (Fritts and Alexander, 2003). This changes as soon as the background wind or stability changes and thus the GW characteristics change, thereby altering the GW phase speed.

Stationary GWs only refer to stationarity in the horizontal with respect to ground and all GWs (except reflected GWs) still propagate in the vertical.

Propagating GWs

A propagating GW has a non-zero ground-based phase speed and is a GW that propagate in time with respect to the ground. These GWs normally have a non-orographic source; Chapter 5 and 6 discuss observations of these GWs. GWs can propagate in the horizontal or in the vertical. In the horizontal the GW can propagate upstream or downstream (Drobinski et al., 2001). Upstream propagating GWs have a wavevector pointing opposite to the wind, however the community only calls it upstream propagation if the GW propagates upstream with reference to the ground (meaning if the GW ground-based phase speed is faster than the environmental wind speed). A GW with a phase speed slower than the background wind propagates against the wind (propagate in an upstream direction), but relative to the ground will move in a downstream direction. GWs propagating with the wind (the wavevector pointing with the wind) are rapidly swept downwind and are rarely observed as they move rapidly out of the observation regime. GWs have been observed to propagate over 2 000 km in the horizontal (Krisch et al., 2017).

Another distinction being made in literature is between upwards and downwards propagating GWs (Fritts and Alexander, 2003). A GW source located at the surface (e.g. mountains) can only excite upward propagating GWs. A source located in the middle atmosphere will most likely generate GWs propagating both upwards and downwards. Downward propagating GWs dissipate at a faster rate since the density increases exponentially downwards, reducing its amplitude. This means the amplitude shrinks exponentially with a decrease in altitude. Upward propagating GWs propagate vertically until they reach a critical layer or break (Huang et al., 2010; Preusse et al., 2008) (for detail on GW breaking refer to Sect. 2.4). GWs have been observed to propagate as high as $\sim$300 km (Ejiri et al., 2019).

Low-, mid-, high-frequency GWs

All vertically propagating GW oscillations have an intrinsic frequency smaller than the Brünt-Väisälä frequency and larger than the absolute Coriolis parameter (Fritts and Alexander, 2003). Upon excitation, a GW will obtain a frequency. The intrinsic frequency is constantly modified as the GW propagates through gradients in temperature and wind (Fritts and Alexander, 2003). **Low-frequency** GWs are very generally characterised as $\hat{\omega} \approx f$ (the GWs discussed in Chap-

ter 6 is an example of this GW type). Arguably **Mid-frequency** GWs represent most of the GWs we work with and satisfies $N \gg \hat{\omega} \gg f$ (Chapter 5 discuss a case study with this GW type). **High-frequency** GWs are known to satisfy $\hat{\omega} \gg f$. High-frequency GWs have a shorter horizontal wavelength and are much more likely to be trapped and to break. The frequency of the GW depends on the background atmosphere and the source of the GW.

2.1.2 GW sources

This section describes topography and the jet as GW sources. Only these two are discussed here in detail in order to lay the groundwork for Chapters 5 and 6. However, for completeness a more elaborate section on different GW sources exist in the Appendix.

GW sources: Topography (Mountain waves)

Topographically induced GWs (called mountain waves) are emitted at the surface by flow over topography (Bacmeister et al., 1994; Eckermann and Preusse, 1999; Durran, 2003; Geldenhuys et al., 2019). Mountain waves are a good example of stationary GWs, where the phase speed of the GW matches the background wind speed. Wind approaching terrain will either be deflected by the terrain or it will rise over the terrain (Chapter 3 discusses this in more detail). An air parcel will pass over the terrain if the flow has sufficient momentum. The flow then accelerates down the lee slope in order to return to its level of neutral buoyancy. This process forms a single wavelength GW, from the trough upwind of the mountain to the trough on the lee side (Gabersek and Durran, 2004; Geldenhuys, 2018).

A useful parameter to diagnose when mountain waves can occur is the Froude number (Wallace and Hobbs, 2006):

$$\mathrm{Fr} = \frac{\bar{u}_{perp}}{N h_m}, \tag{2.10}$$

where $\bar{u}_{perp}$ is the wind perpendicular to the mountain averaged from surface to mountain top and h_m is the observable mountain height (valley floor to peak). When $Fr > 1$ the airflow is supercritical and can pass over the mountain and a propagating mountain wave is generated. Each mountain height has its own set of conditions that will induce mountain waves. We can calculate this by setting Fr to 1, plug in the stability and thereby calculate the required wind speed that will have enough momentum to pass over the barrier. As an example, the model stability (for SouthTRAC

flight 8 that is discussed in Chapter 5) averaged from surface to 1 000 m is 0.0057 s^{-1}. By setting h_m = 1 000 m we calculate the required wind to pass over the barrier at 6 m s^{-1}. This is remarkably close to the generalised (for all atmospheric stabilities) 7 m s^{-1} for a mountain of 1 000 m height identified in literature (e.g. ICAO, 2007; Barry, 2008). This means all perpendicular wind speeds greater than 6 m s^{-1} will pass over the barrier and will form a GW if the static stability permits it. Mountain waves are known to fall in the high-frequency to mid-frequency range and have been observed with horizontal wavelengths varying from only a few kilometers (Geldenhuys et al., 2019) to in excess of 400 km (Smith and Kruse, 2017).

GW sources: Jet stream

A jet stream is defined as a narrow region of relatively strong winds in the atmosphere, which frequently stretches around the globe (AMS, 2018). The overview paper by Plougonven and Zhang (2014) provides an overview of GWs emitted by the jet stream. The jet stream is a dynamically active region with multiple possible GW source mechanisms. The jet stream can induce GWs by wind shear (see Appendix Sect. A.2), by Lighthill-radiation for balanced flow (Plougonven and Zhang, 2014) or by an out-of-balance jet stream (O'Sullivan and Dunkerton, 1995; Zülicke and Peters, 2006; Plougonven and Zhang, 2014). It has been shown that when a jet emits a GW the Wentzel-Kramers-Brillouin (WKB) parameter is frequently violated (Hertzog et al., 2001) for the emitted GW. The WKB parameter is violated once the scales of change of the wavenumber is large compared to the wavelength of the GW (Marks and Eckermann, 1995). For a full description on this, refer to Sect. 4.4.

A wind with all its forces in balance can emit weak GWs by Lighthill-radiation. The mechanism of GW excitation is modelled after a theory by Lighthill (1952) on the generation of acoustic waves from turbulent motions. Plougonven and Zhang (2014) state that GWs are only emitted by this mechanism for flows in balance with a Rossby number > 1 and a Froude number $\ll 1$. Analytically, it has been shown that the GWs have scales one order of magnitude larger than the small-scale balanced motion — which only occurs in compact regions. GWs emitted from this mechanism are weak and interaction with the background flow is minimal. Given that the background flow does not change, this mechanism can continuously radiate GWs for extended periods, contrary to GWs emitted by an out-of-balance jet.

The excitation of GWs from an out-of-balance jet by spontaneous adjustment has been studied thoroughly and is usually associated with strong Rossby waves and potentially Rossby wave

breaking (e.g. Ford et al., 2000; Snyder et al., 2007; Zülicke and Peters, 2006; McIntyre, 2009; Mirzaei et al., 2014; Plougonven and Zhang, 2014; Ern et al., 2016; Geldenhuys et al., 2021). A jet stream is governed by the geostrophic balance equation in the x-direction (Holton, 2004):

$$fv = -\frac{1}{\rho}\frac{\partial p}{\partial x}, \tag{2.11}$$

and in the y-direction:

$$fu = -\frac{1}{\rho}\frac{\partial p}{\partial y}, \tag{2.12}$$

where u is the zonal wind component and v is the meridional wind component. The left-hand side of the equation represent the Coriolis force and the right-hand side the pressure gradient force. Geostrophic balance assumes the left-hand side and right-hand side are equal, resulting in the wind to blow along lines of constant pressure.

When the two sides of the equations are not in balance the jet is said to be out-of-balance and can generate GWs (Zülicke and Peters, 2006). The area of imbalance normally occurs in the jet exit region and can radiate GWs spontaneously in an attempt to balance the Coriolis and pressure gradient forces. The process is also called geostrophic adjustment. The cross-stream ageostrophic wind speed or the cross-stream Lagrangian Rossby number can be used to diagnose an out-of-balance jet (e.g. Zülicke and Peters, 2006; Mirzaei et al., 2014; Plougonven and Zhang, 2014). Mirzaei et al. (2014) found that similar results are obtained for both parameters, with less noise when using the cross-stream ageostrophic wind speed. The cross-stream ageostrophic wind speed is defined by:

$$U_c = \frac{u_a v - v_a u}{(u^2 + v^2)^{1/2}} \tag{2.13}$$

where subscript $_a$ denotes ageostrophic wind component (for more information on how to apply this formula refer to Chapter 6).

To explain geostrophic adjustment we assume a jet blowing from west to east at constant latitude. For this jet the geostrophic balance equation holds for the greater part of the jet with exception of the entrance and exit regions. In the entrance (exit) region of the jet the wind converges

(diverges). During convergence (divergence) the pressure lines similarly converges (diverges) and entails a change in the pressure gradient (right-hand side of Eqs 2.11 and 2.12). However, the Coriolis force remains relatively constant given that the jet is still aligned along the same latitude line. To bring the left-hand and right-hand side of the equations (Eqs 2.11 and 2.12) back into balance, the jet needs to get rid of its excess energy. For an unbalanced flow to achieve a balanced state, a redistribution of energy, momentum and potential vorticity is required, frequently combined with a release of GWs.

The characteristics of GWs originating from adjustment processes are closely linked to the size and timescale of the source region (Fritts and Alexander, 2003). Vertical wavelengths are typically a few km's and horizontal wavelengths are ≈10–100 times larger. In cases of an elongated source, the orientation of the GW wave vectors are perpendicular to the source axis. An adjustment process is known to emit low-frequency GWs and literature has found horizontal wavelengths ranging from 50 km to 500 km (Uccellini and Koch, 1987; Plougonven and Zhang, 2014). The jet emits GWs above and below the jet as upward and downward propagating GWs (Zülicke and Peters, 2006; Geldenhuys et al., 2021). A vertical cut through these GWs form a characteristic fishbone structure.

Multiple processes can contribute to convergence and divergence in the jet (e.g. pressure gradient changes, friction, cold air advection, topography, inertial instabilities, etc.), affecting balanced forces in the jet and ultimately leading to GW excitation. Some literature treat inertial instabilities as a separate source of GWs (e.g. Rowe and Hitchman, 2015), however inertial instabilities and the jet are linked. Fritts and Alexander (2003) state another example of a GW source mechanism linked to the jet: 'The adjustment processes ... closely analogous to the radiation of GWs by a collapsing mixed layer due to shear instability examined by Buehler et al. (1999)...'. Both inertial instabilities and shear layers are treated here as separate sources and is discussed in detail in the Appendix.

2.2 GW propagation

Irrespective of the GW source excitation mechanism the GW starts to propagate through the atmosphere following excitation (blue box in Fig. 2.1). In physics the movement of any object can be described by the terms ∂x, ∂y, ∂z and ∂t in a cartesian coordinate system. Similarly GW propagation in a Eulerian system is described by Eqs 2.3, 2.4 and 2.5 (Marks and Eckermann, 1995).

These equations temporarily assume constant GW characteristics; the change of GW characteristics due to interaction with the background flow is discussed later in this section. According to Marks and Eckermann (1995) (and references there-in) one can calculate Eqs 2.3, 2.4 and 2.5 using a Cartesian coordinate system and transform this onto a sphere by geometric conversion. These equations can be used to forecast where the GW will propagate to and at what speed.

Basic physics principles suggest that GWs with a longer wavelength travel at a faster speed and can reach further in a shorter time. This is confirmed by the GW propagation Eqs 2.3 to 2.5 where the wavenumber is squared in the denominator. By reworking the dispersion relation (Eq. 2.6) and applying four criteria:

- $N \gg f$ in the stratosphere — this means term $f^2(m^2 + \frac{1}{4H^2})$ can be neglected,
- $\frac{1}{4H^2} \ll m$ — this means term $\frac{1}{4H^2}$ can be neglected,
- $\hat{c} = \frac{\hat{\omega}}{k_h}$ where $k_h = \sqrt{k^2 + l^2}$,
- $\hat{c} = c_{gb} - U_{||}$ where $U_{||}$ is the wind speed parallel to the wavevector,

the following equation is obtained:

$$\lambda_z = \left| 2\pi \left(\frac{c_{gb} - U_{||}}{N} - \frac{1}{k_h} \right) \right|, \tag{2.14}$$

where λ_z is the vertical wavelength. Eq. 2.14 shows the dependency of the vertical wavelength on the background wind and stability. From this equation it becomes evident that if the GW ground-based phase speed approaches the wind speed perpendicular to the phase front, the vertical wavelength will approach 0. Such a decreasing wavelength will slow the upward propagation and keep the GW below a level, which is called a critical level (see Sect. 2.1.1 for a further discussion on critical levels). A decreasing wavelength also indicate the GW is breaking and its characteristics are changing.

The changing GW characteristics means GW propagation is much more complex than simply solving Eqs 2.3 to 2.5. The GW characteristics are constantly changing due to exchanges with the background flow, which is not captured by these equations. Similarly the background flow is changing due to exchanges with the GW. Eqs 2.3 to 2.5 assume the GW and the background flow do not interact. To solve this we temporarily ignore GW damping and determine the influence of the background atmospheric data on the GW characteristics by solving (Marks and Eckermann,

1995):

$$\frac{dk}{dt} = -k\frac{\partial u}{\partial x} - l\frac{\partial v}{\partial x} - \frac{1}{2\hat{\omega}(k^2+l^2+m^2+\frac{1}{4H^2})}\left[\frac{\partial N^2}{\partial x}(k^2+l^2) - \frac{\partial}{\partial x}\frac{1}{4H^2}(\hat{\omega}^2-f^2)\right], \tag{2.15}$$

$$\begin{aligned}\frac{dl}{dt} = &-k\frac{\partial u}{\partial y} - l\frac{\partial v}{\partial y} - \frac{1}{2\hat{\omega}(k^2+l^2+m^2+\frac{1}{4H^2})}\left[\frac{\partial N^2}{\partial y}(k^2+l^2) - \frac{\partial}{\partial y}\frac{1}{4H^2}(\hat{\omega}^2-f^2)\right] - \\ &\frac{f\frac{\partial f}{\partial y}}{\hat{\omega}(k^2+l^2+m^2+\frac{1}{4H^2})}\left(m^2+\frac{1}{4H^2}\right),\end{aligned} \tag{2.16}$$

and,

$$\frac{dm}{dt} = -k\frac{\partial u}{\partial z} - l\frac{\partial v}{\partial z} - \frac{1}{2\hat{\omega}(k^2+l^2+m^2+\frac{1}{4H^2})}\left[\frac{\partial N^2}{\partial z}(k^2+l^2) - \frac{\partial}{\partial z}\frac{1}{4H^2}(\hat{\omega}^2-f^2)\right]. \tag{2.17}$$

Equations 2.15 to 2.17 show how the background flow affects the GW characteristics through time. The vertical wavelength is influenced by vertical wind shear. Similarly, the horizontal wavelength and orientation is influenced by the horizontal wind shear. The change in orientation of the GW (called refraction) is discussed through the use of Eqs 2.15 and 2.16 as well as observational data in Chapter 5. Up to this point the equations still assume the GW has no effect on the background atmospheric conditions. To include this effect, we need to study GW dissipation (see Sect. 2.4 and Appendix Sect. A.6) and GW growth.

2.3 GW growth

Gravity wave growth takes place due to changes in the background atmospheric state. GWs have many properties that can grow (Fig. 2.1), i.e. horizontal wavelength, vertical wavelength and amplitude. GWs most frequently grow due to interactions with the background wind and stability, but have also been observed to grow via different processes. Mirzaei et al. (2014) found that when latent heat is released the GW energy increase. The latent heat changes the enthalpy, which triggers a change in the kinetic energy of the GW. A GW with less energy (typically a smaller GW) can also grow at the expense of a GW with more energy (typically a larger GW)

through non-linear processes (Fritts and Rastogi, 1985b, and references there-in).

A small amplitude GW will transfer energy slowly and a large amplitude GW is much more likely to transfer energy (Fritts and Alexander, 2003). Multiple processes exist in literature that dictates wave-to-wave energy exchanges. *Firstly*, GWs with similar wavenumbers and frequencies can exchange energy — called three-wave resonant interactions. *Secondly*, elastic scattering entails the transfer of energy through scattering between upward and downward propagating GWs with comparable vertical wavenumbers. *Thirdly*, energy is transferred from one GW to another with comparable wavenumbers, but requires a much smaller vertical wavenumber. The most important mechanism (and *fourthly*) is known as PSI (parametric subharmonic instability) where energy is exchanged from one dominant higher frequency GW to another GW (sometimes two GWs) having half the frequency and nearly opposite large wavevector compared to the primary GW.

The background wind and stability arguably influence the GW characteristics the most. Eqs 2.15 and 2.16 show which variables can lead to a horizontal wavelength growth. The change in wavelength is influenced by horizontal gradients in the wind, stability and the scale-height. The scale-height remains approximately constant in one atmospheric layer and can be neglected. A negative wind gradient will turn the $-k\frac{\partial u}{\partial x}$ and $-l\frac{\partial v}{\partial x}$ terms in Eq. 2.15 to positive, which will enhance the wavelength in the x-direction (this similarly applies to the wavelength in the y-direction). Similarly a negative gradient in the stability (a GW propagating from a higher stability to a lower stability) will lengthen the horizontal wavelength.

According to Eq. 2.17, growth of the vertical wavelength depends on vertical gradients in the wind, stability and the scale-height. In the stratosphere, changes in the scale-height is small at the vertical propagation speed of GWs and is expected to have little influence. A negative wind gradient (if the GW propagates from a strong wind to a weak wind) and a negative stability gradient will result in a longer vertical wavelength. Throughout most of the atmosphere wind speed and stability is increasing with altitude, this creates a positive gradient. For upwards propagating GWs m is negative, this implies that m is becoming smaller with a positive gradient, and the vertical wavelength becomes larger. This implies that the GW is becoming larger, and is growing, with vertical propagation.

Amplitude is well known to grow exponentially with altitude (e.g. Marks and Eckermann, 1995; Vadas et al., 2018). Density decreases exponentially with altitude and hence the disturbance in the density (the amplitude) grows at a similar rate. Eckermann (1995) found in a theoretical study that the GW temperature variance (which is loosely relatable to amplitude) is governed by

(Eckermann, 1995; Fritts and Alexander, 2003):

$$\overline{(T'/\bar{T})^2} \propto (N^3/N_0)(\rho_0/\rho), \tag{2.18}$$

where T represents temperature, subscript 0 indicates the value at reference level, the large overbar indicates variance and the short bar indicates smoothed background data. Here we can see that temperature variance (and hence amplitude) is dependent on stability and density. The faster the decrease in density, the faster the growth in amplitude. Marks and Eckermann (1995) found that in the absence of dissipation and large gradients in the background flow the horizontal wind amplitude increases consistently with $\rho_0^{-1/2} \propto exp(\frac{z}{4H^2})$. Vadas et al. (2018) mentions that the amplitude grows nearly exponentially at $\approx exp(z/2H)$.

Recently observations revealed that the increase in GW amplitude in the stratosphere and mesosphere is larger than expected and can not only be described by the decrease in density only (Gabriel, 2022). The study by Gabriel (2022) revealed a curious dependence of the amplitude growth on ozone. It was found that the GW amplitude increases by a greater amount during day compared to night time. This was attributed to the fact that in the GW updraft the amount of ozone is increased due to displacement. During daytime, the increased ozone results in an increase in the heating rate compared to the environment, which results in an amplification of the initial uplift. The amplitude of the GW will continue to increase up until the amplitude plus background temperature becomes unstable. Once unstable, instability sets in, the GW starts to break and the amplitude starts dissipating.

2.4 GW dissipation

Gravity wave dissipation takes place through a variety of processes, namely radiative damping, wave-wave interactions, GW breaking and instability processes (Fritts and Alexander, 2003). Spreading of the GW packet reduce the amplitude (Mixa et al., 2021) and can be seen as dissipation, but, the total energy of the GW packet remains intact. Here only the processes that reduce the total energy are considered. Wave-wave interactions were briefly discussed in the above section, this section will deal with GW dissipation by breaking and instability.

Gravity wave breaking is the process whereby a GW deposits all (rapid and full dissipation – Fig. 2.1) or part of its energy (slow and partial dissipation – Fig. 2.1). The deposited energy

is in the form of GWMF and the drag acts in the direction of the wavevector. If the wavevector was pointing opposite (with) to the wind the background wind is forced to slow down (speed up). Dissipation can take place due to shear or due to convective instability. Dissipation by shear slowly and partially weakens the GW. Convective instability can cause overturning and often results in a large reduction in amplitude.

2.4.1 Dissipation by shear

A GW that encounters a strong wind layer and can not propagate through this layer will start to dissipate (Pierrehumbert, 1986). This layer is frequently referred to as a critical layer (Sect. 2.1.1) (Fritts and Alexander, 2003). Such a dissipation mechanism is seen in Chapter 6 where the GW amplitude reduces as the wave meets a critical layer. If the wind shear between the GW and the background becomes too large Kelvin-Helmholtz waves are excited (see Appendix for a description on this and see Fig. 2.2 for photos of this mechanism) (Pierrehumbert, 1986).

Figure 2.2: Lenticular clouds of mountain waves. Note the Kelvin-Helmholtz structures on the top of the lenticular clouds which points to increased wind shear and GW dissipation. The left photo shows a more ragged cloud in the Kelvin-Helmholtz structure. This is presumably because the Kelvin-Helmholtz waves are busy transitioning to turbulence. Photos were taken on 13 December 2017 along the south coast of South Africa.

Kelvin-Helmholtz waves will grow if the local Richardson number becomes critical (normally < 0.25) (Fritts and Rastogi, 1985b, and references there-in):

$$\mathrm{Ri} < k^2 d^2 (1 - k^2 d^2), \tag{2.19}$$

where d is the length of the region that is considered. Energy cascades from the large-scale wave to the small-scale Kelvin-Helmholtz waves (Fritts and Rastogi, 1985b; Fritts and Alexander, 2003). This reduces the amplitude of the primary GW partially dissipating its energy (Fig. 2.1).

Fritts and Rastogi (1985b) derived an equation that determines at which temperature amplitude Kelvin-Helmholtz instability will set in:

$$\hat{T}_{max} = \frac{1}{2}\sqrt{16\left(\frac{\hat{\omega}^2}{f^2}-1\right)^2 + 16\left(\frac{\hat{\omega}^2}{f^2}-1\right)} - 2\left(\frac{\hat{\omega}^2}{f^2}-1\right). \tag{2.20}$$

Fritts and Rastogi (1985b) state that this weakening of the primary GW by Kelvin-Helmholtz waves can be the reason why the amplitude do not grow at small vertical phase speeds. The turbulence generated by the break down of the Kelvin-Helmholtz waves is transformed into a diffusion of heat, which acts to slow down the background wind (Zhou et al., 2002).

Shear breaking is known to exist in low-, mid- and high-frequency GWs (Fritts and Alexander, 2003), but is more frequently observed in low-frequency GWs (Fritts and Rastogi, 1985a). Woiwode et al. (2018) observed GW overturning and partial breaking in the polar front jet (the jet indicating it was most likely shear generated breaking). Geldenhuys et al. (2021) similarly observed a GW with a reduction in amplitude below a critical layer (as described in Chapter 6).

2.4.2 Dissipation by convective instability

Gravity wave breaking due to convective instability mostly affects high-frequency GWs (Fritts and Rastogi, 1985b). Convective instability represent a temperature lapse rate that is superadiabatic. A high-amplitude GW that superimpose on the background temperature frequently results in a superadiabatic lapse rate. Convective instability takes place for the condition (Vadas et al., 2018):

$$\left|\frac{{u_h}'}{C_{gb_H} - \bar{U}}\right| \approx 0.7 - 1.0, \tag{2.21}$$

where ${u_h}'$ is the total wind speed amplitude and C_{gb_H} is the horizontal phase speed and $\bar{U}$ is the horizontal wind along the wavevector ($(ku+lv)/k_h$). If this condition is satisfied the amplitude of the GW will decrease (slow and partial dissipation — Fig. 2.1) as convective instability sets in. Once convective instability sets in, the 2-D laminar flow erupts into a 3-D turbulent field (Fritts and Rastogi, 1985b, and references there-in). The turbulence acts to mix the atmosphere and thereby reduce the background density gradient. The turbulent field have also been observed to generate other wave motions.

Literature makes reference to full rapid overturning and breaking (Dörnbrack et al., 1995) and slow partial dissipation (Fritts and Rastogi, 1985b) (Fig. 2.1). If the lapse rate becomes superadiabatic, depending on the Reynolds number, the GW will partially break (as described above) or it can fully overturn and break turning into 3-D turbulence as described in Dörnbrack et al. (1995). However, Eckermann et al. (1995) states that the GW will only shed enough energy to remain at a stable amplitude.

Observational evidence of GW dissipation is discussed by Mixa et al. (2021). They observed vortex rings that followed the GW breaking, which propagated down along the warm phase fronts. They attributed this process to convective GW breaking. Mixa et al. (2021) also showed observationally and numerically that convective and shear induced dissipation can co-exist.

2.5 Summary

This chapter discussed the lifecycle of GWs as depicted in Figure 2.1. Different GW types are briefly discussed followed by the excitation of GWs with its mechanisms and sources. Sources that are discussed includes topography and out-of-balance jet streams. Other sources like inertial instability, katabatic winds, convection, fronts, GW breaking, Rossby waves / tropopause folds, volcanoes, wind shear and Kelvin-Helmholtz instability are discussed in the Appendix. The chapter also discuss the propagation, growth and multiple dissipation mechanisms. The GW lifecycle (Fig. 2.1) form a complete circle and can renew itself to remain ongoing throughout the atmosphere. Following dissipation a new GW is excited by secondary generation (see Appendix A.6) making the process renewable. Refraction is not discussed in this chapter since Chapter 5 is dedicated to refraction.

Chapter 3

New implications on GW physics due to blocking

In this chapter GW physics in the vicinity of low-level blocking is analysed. Literature states that models require more GW drag. In this chapter the orographic GW physics is analysed in order to evaluate the realism of the subgrid physics in the parameterisation scheme. A common misconception by the GW community and an incorrect implementation of the physics is discussed. This chapter discusses the outcome from Objective 1 (see Chapter1; Geldenhuys (2022)).

3.1 Subgrid GW representation in models and future relevance

Given the importance of GWs for the dynamics (Fritts and Alexander, 2003; Sato and Hirano, 2019), it is disconcerting that models differ by as much as 20% in their surface parameterised drag (Sandu et al., 2016). It is well known that to have an accurate model, GW drag needs to be represented realistically (Plougonven et al., 2020). To represent reality, GW parameterisation schemes are required to represent the effect of GWs not explicitly resolved in the general circulation model. Every model is different concerning the amount of drag produced, this reveals uncertainty in the parameterisation schemes. Some models adjust the GW drag by looking at basic variables, and others have a 'knob' in their equations which can be used to increase or decrease the drag (Kim and Doyle, 2005; Sandu et al., 2016; Polichtchouk et al., 2018a). This reveals the lack of physical realism in these schemes and that different models have found different ways to unphysically approximate the effects of the missing GWs.

The parameterised part of the GW spectrum is ever-shrinking with increases in model resolutions, however, Berner et al. (2007) suggest that in the future, computational resources can likely be directed to running more ensemble members or running an Earth system model in contrast to further increasing resolution. Recently Lang et al. (2021) doubled the operational Integrated Forecast System (IFS) vertical resolution and still the model required parameterisation schemes. This means, at the highest currently feasible resolution the whole GW spectrum is far from being resolved. With these trends and the restriction on computational growth in mind, parameterisation schemes are expected to be around for some time to come.

Recently Plougonven et al. (2020) highlighted the remaining unaccounted GW phenomena in parameterisation schemes, namely secondary emission, lateral propagation and transience. The community is actively addressing these issues for orographic GWs. For example, a new transient GW parameterisation scheme is currently being developed (Boeloeni et al., 2021; Kim et al., 2021), and the WASCLIM project (BMBF's priority programme ROMIC II) develops a mountain wave model based on Bacmeister et al. (1994) to help address lateral propagation. Recently, Van Niekerk and Vosper (2021) implemented a 'scale-aware' orographic GW drag scheme that represents the whole sub-grid GW spectrum. Many other studies exist with constant improvements being made in GW parameterisation schemes (Lott et al., 2012; McLandress et al., 2012; de la Camara et al., 2016; Garcia et al., 2017; Polichtchouk et al., 2018a; Xie et al., 2019; Plougonven et al., 2020). Currently, an International Space Science Institute Team exists focusing only on identifying constraints on orographic GW drag (ISSI, 2022). Even observational campaigns have dedicated objectives to improve understanding of GWs for improvement of parameterisation schemes (Fritts et al., 2016; Serafin et al., 2020; Rapp et al., 2021). In spite of all these activities, an important issue of low-level blocking has so far been overlooked.

3.2 Current implementation of GW physics near low-level blocking

Wind flow is blocked by a mountain barrier if it does not have enough momentum to ascend the barrier. Blocking is found in all mountainous areas, as long as the stability and wind requirements are met (Smith, 2019). Blocking takes place when cold stable air does not have sufficient momentum to pass over a barrier and is deflected (Neiman et al., 2010; Geldenhuys et al., 2019; Smith, 2019). Locally this results in a higher pressure with an increase in the pressure gradient

and in turn a stronger wind. The mountain deflects the wind and a low-level wind is formed parallel to the mountain barrier (Fig. 3.1d). This stronger (and deflected) wind is called the blocking jet — although it is called a jet it merely acts as a reference to the stronger wind. This low-level jet is characterised by a higher pressure, stronger winds and a deflected wind direction. This jet continues to build upwind and has been observed to extend up to 200 km upwind of the barrier (Loescher et al., 2006).

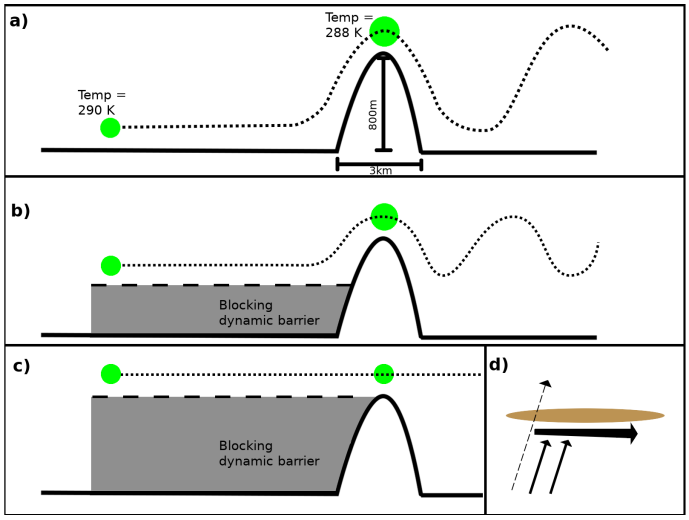

Figure 3.1: Mountain wave excitation as assumed by the physics in the model parameterisation schemes. Mountain dimensions are based on the case of Geldenhuys et al. (2019), but can take any values. Green circles indicate the air parcels being uplifted and dotted lines indicate the wind perpendicular to the mountain ridge. Panel (a) shows the typical mountain wave excitation. Panel (b) and (c) show what the model assumes different stages of blocking (shaded part) and what its corresponding mountain wave looks like. Note that panel (c) represents a complete blocking layer up to mountain height. Here the model perceives no vertical displacement, thus producing no GW drag. Panel (d) shows the blocking situation from above. The light brown ellipse represent the mountain. The large arrow represents the blocking jet (dynamic barrier), the solid arrows represent the incoming low-level winds and the dashed arrow indicates the wind $\approx$ 500 m above the terrain. In Eq. 3.1, the dashed arrow projected onto the large arrow form U_{ref}. The figure is not to scale.

Most mountain wave parameterisation schemes (Pierrehumbert, 1986; Kim and Arakawa, 1995; Lott and Miller, 1997; Kim and Doyle, 2005; Sandu et al., 2016; Xie et al., 2019) have the GW drag dependent by some means on low-level blocking. Schemes building on Pierrehumbert (1986) (e.g Kim and Arakawa, 1995; Kim and Doyle, 2005; Xie et al., 2019) scale the GW drag at reference level with the wind projected onto the low-level wind direction (the blocking wind direction). The GW drag is determined by (Eq. 6 from Kim and Doyle (2005)):

$$\tau_{GWD} = \rho_0 E \frac{m_{no}}{\lambda_{eff}} G \frac{|U_{ref}|^3}{N_0} \tag{3.1}$$

where τ_{GWD} is the calculated GW drag, E is the enhancement factor, m_{no} is the number of mountains, λ_{eff} is the grid length or acts as a tuning coefficient, G is the asymptotic function to facilitate a smooth transition between 2-D blocking and non-blocking cases, U_{ref} is the horizontal wind speed at reference level that is projected onto the low-level wind direction (blocking jet) and N_0 is the the low-level Brünt-Väisälä frequency (For an in-depth explanation of the formula and its terms refer to (Kim and Doyle, 2005)). In a typical blocking case, the wind direction at low levels and the reference level (above the terrain) can differ by anything from a few degrees to ≈90°. This means that the wind entering the GW drag equation (Eq. 3.1) can be reduced drastically, reducing the resultant GW drag. To illustrate the maximum reduction, a blocking case from Geldenhuys et al. (2019) is represented in Fig. 3.1d. If the wind at reference level (dashed arrow) is projected to the blocking jet direction the wind speed, and hence the GW drag, would reduce to ≈0.

In schemes building on Lott and Miller (1997) (e.g. ECMWF, see Sandu et al. (2016)), the GW drag is reduced exponentially depending on the blocking layer depth. ECMWF employs (ECMWF, 2015):

$$\tau_{GWD} = \rho_0 b G_s B(\gamma) N U H_{eff}^2 \tag{3.2}$$

where b is the mountain height variation in the along-ridge direction, G_s is the function of mountain sharpness, γ is the represents mountain anisotropy and B is the function of γ which can vary from 1 for a 2-D ridge and $\pi/4$ for a circular mountain. H_{eff} is the effective mountain height represented by:

$$H_{eff} = 2(H - Z_{blk}) \tag{3.3}$$

where h_m is the ridge height and Z_{blk} is the depth of the blocking layer. Eqs 3.2 and 3.3 show that the GW drag depends exponentially on the blocking layer depth. The models assume that with an increase in the blocking layer depth the layer of wind approaching the terrain is reduced, and the GW field is reduced (Fig. 3.1b as opposed to the normal case of Fig 3.1a). Many idealised 2D models also follow this approach and reduce the GW field depending on the depth of the wind approaching the barrier. This assumption reduces the amplitude of the GW (it is important to take note of this, as the rest of the chapter will frequently refer to this reduction). This means that the assumed GW depends only on the wind from the blocking layer top to the mountain top. It is

argued that this can cause the model to underestimate the GW drag. In the following sections of this chapter, it is suggested that a more realistic approach would be if parameterisation schemes account differently for the blocking layer during GW generation.

3.3 Why do parameterisation schemes account for the blocking layer?

Compared to the environmental conditions, the blocking region is characterised by a higher pressure, stronger wind and a deflected wind direction (Neiman et al., 2010; Smith, 2019; Geldenhuys et al., 2019). This blocking region with different characteristics forms a dynamic barrier (Neiman et al., 2010; Geldenhuys et al., 2019). The dynamic barrier takes a variety of different names in literature, for example Bell and Bossart (1988) refer to it as a cold dome with a low-level wind maximum while it is called flow blocking in Barry (2008) and barrier jet in Smith (2019).

This dynamic barrier represents a mountain-like structure. Parameterisation scheme approximations assume that the dynamic barrier reduces the depth of the wind component perpendicular to the mountain (Fig. 3.1). This means that a parcel of air will be displaced a shorter vertical distance (Fig. 3.1b) compared to the normal case (Fig. 3.1a), meaning a 'smaller' mountain wave will form with a lower amplitude (H_{eff} in Eq. 3.2 and Eq. 3.3 show this). If the blocking layer is at maximum depth (up to ridge height — Fig. 3.1c) then the parameterisation scheme assumes no mountain waves will be excited, since it assumes there was no displacement. This approach seems correct, but incorrectly assumes the width of the blocking layer to be infinite.

The width of the blocking layer will depend on the barrier and meteorological conditions in question. The width of blocking layers has been observed in many parts of the world, for example 50 km in British Columbia (Overland and Bond, 1995), 80 km in South Africa (Geldenhuys et al., 2019), 81 km in the Gulf of Mexico (Luna-Nino and Cavazos, 2017) and 1 up to 200 km in Alaska (Loescher et al., 2006). The width of the blocking jet can be anything from a few kms to a few hundred kms. This means the blocking layer width is within the same to 1 order of magnitude higher than the mountain width, but certainly not infinitely wide. The model approaches discussed in this chapter focus on the direct vicinity of the mountain and fail to capture the characteristics of the larger system. However, it is the characteristics of the larger system that is relevant for the excitation of mountain waves.

3.4 Considerations of the blocking layer influence on determining model GW drag

The blocking layer is known to be a narrow-sloping layer (Parish, 1982; Bell and Bossart, 1988; Neiman et al., 2010; Geldenhuys et al., 2019) as long as no upwind topography exists in the close vicinity. The dynamic barrier will have a maximum depth at the mountain face and will slope in the upwind direction (Fig. 3.2). This means that an air parcel approaching the sloping barrier will either help build the blocking jet outwards or will be forced to rise above this 'mountain-like' structure. As early as Bell and Bossart (1988) it was suggested that the air parcel will rise above the sloping blocking layer (Fig. 3.3). The air parcels passing over the dynamic barrier will be forced to rise from the surface to mountain height. The displacement height and the required work is the same as in the traditional mountain wave case (Fig. 3.1a). At the mountain top, the air parcels in Fig. 3.2 will not be at equilibrium altitude and will fall to the lee side, exciting a mountain wave. The mountain wave forming during blocking conditions will have an amplitude comparable to the case without a blocking layer, and should not be reduced as Eq. 3.2 and Eq. 3.3 suggests.

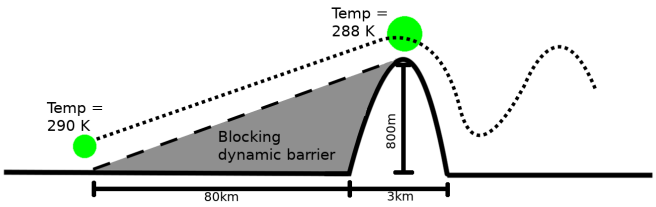

Figure 3.2: Airflow as expected in the vicinity of a blocking region. The blocking layer (shaded) is complete and extend up to ridge height while taking the form of a sloping dynamic barrier. Green circles indicate an air parcel being uplifted and the dotted line indicates wind flow projected perpendicular to the ridge. The figure is not to scale.

It should be kept in mind that although the vertical displacement remains the same in the two cases (no blocking, Fig. 3.1a, and realistic blocking layer, Fig. 3.2), the GW field will differ. Multiple reasons are the cause of this. Firstly, the width of the mountain has changed from a narrow ridge to a broad barrier — as the blocking layer adds to the width of the barrier. Secondly, the blocking jet can produce its own mountain waves. The blocking jet blows parallel to the main ridge but perpendicular to the side ridges leading up to the main ridge. These have been observed to excite mountain waves and can cause different GWs to interfere, which forms a complex pattern (Van der Mescht and Geldenhuys, 2019). The blocking air can also spill over the mountain exciting a mountain wave or a hydraulic jump (Geldenhuys et al., 2019).

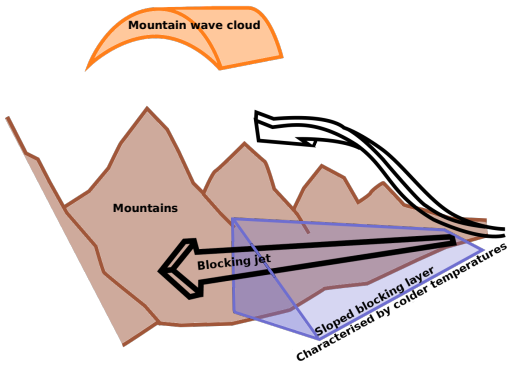

Figure 3.3: Adapted from Bell and Bossart (1988) who first suggested that the airflow will flow over the sloping blocking region. The incoming stable flow is deflected by the mountains to produce a blocking jet (black arrow parallel to the mountain ridge). The blocking region is known to be more stable, with a colder temperature and higher pressure. This region is indicated by the blue sloping dynamic barrier. Note the winds upwind of the blocking layer ascends the dynamic barrier as well as the mountains. The mountain wave cloud is not present in the original drawing, but was added here to show that the wind flowing over the barrier can induce GWs.

The width of the barrier (mountain + dynamic barrier) will effect the GW field. In the blocking case, the horizontal wavelength of the GW will be longer since the displacement starts further upwind (Fig. 3.2). A longer horizontal wavelength will reduce the GWMF, but not nearly as much as the temperature amplitude. This is evident in the GWMF equation for a single gravity wave (Ern et al., 2015):

$$\mathrm{GWMF} = \frac{1}{2}\rho_0 \frac{\lambda_z}{\lambda_h}\left(\frac{g}{N}\right)^2\left(\frac{\hat{T}}{T}\right)^2 \tag{3.4}$$

where λ_h is the horizontal wavelength. The effect of the temperature amplitude dominates as the GWMF can be brought to zero for a full blocking layer with a temperature amplitude of 0 K. A longer horizontal wavelength reduce the GWMF slightly compared to zero GWMF for an amplitude of 0 K. The fact that H_{eff} is squared in Eq. 3.2 show that the displacement height (directly proportional to the amplitude) affects the GWMF exponentially in the model. Hence, it can be said that an incorrect horizontal wavelength is not nearly as bad as an incorrect temperature amplitude.

A blocking jet blowing parallel to the main ridge forms ideal conditions for short horizontal scale mountain waves. The strong wind in a stable environment will blow over all the side ridges running up to the main ridge and has been linked with short-wavelength GWs (first instance how blocking can help excite GWs) producing severe turbulence (Van der Mescht and Geldenhuys, 2019). Models using an anisotropy parameterisation scheme with a high-resolution orographic field can theoretically account for this.

A second mechanism in which a blocking layer can directly produce mountain waves is by air spilling downwind. Once the blocking layer reaches the altitude of the mountain ridge the blocking layer will continuously weaken by air spilling to the lee side. The spilt cold blocking air will accelerate down the lee slope and can adjust forming a hydraulic jump. The air rushing down the lee side has many implications (e.g. displacing cold pools (Lareau and Horel, 2014)) but the important one here is the hydraulic jump that can excite a propagating GW (second instance how blocking can help excite GWs). The top of the blocking layer is characterised by a transitional Froude number (≈ 1). Such a Froude number has long been linked with producing waves in the lee of mountains (Fig. 3.4). Such a mechanism has been observed from katabatic winds in Antarctica (Yu and Cai, 2006; Watanabe et al., 2006; Vignon et al., 2020), over Greenland (Tollinger et al., 2019) and in the blocking regime in South Africa (Geldenhuys et al., 2019).

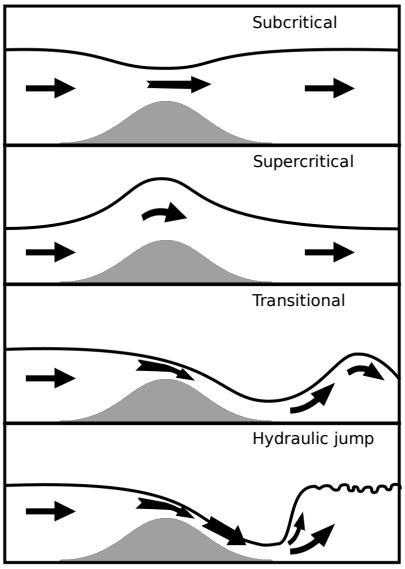

Figure 3.4: Flow over mountainous terrain with a subcritical (< 1), supercritical (> 1) and transitional Froude number (≈ 1). The hydraulic jump can take place during transitional flow. Adapted from (Bradbury, 1991).

Figure 3.5 is the result of an idealised modelling study and shows good evidence of GWs originating from air spilling downwind. Note how the potential temperature lines indicate no upward displacement of isolines directly upwind of the barrier. This most likely indicates a blocking layer, inhibiting the air to be displaced in the normal manner. Also note the GW structure directly downwind of the barrier similar to what Fig. 3.2 suggests. The GW structure is visible up to 8 km in Fig. 3.5, highlighting the importance of this mechanism.

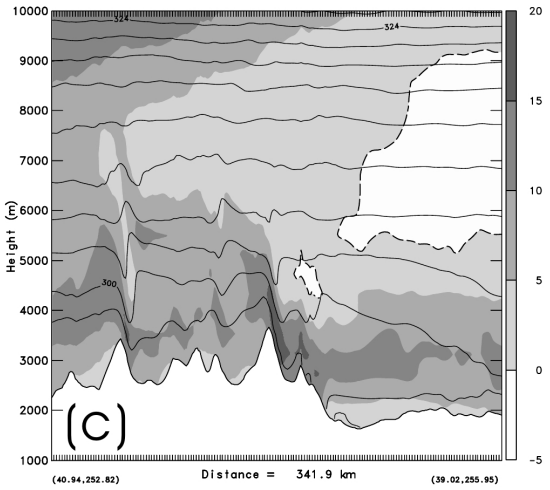

Figure 3.5: Figure 9c from Kim and Doyle (2005) show the result from an idealised modelling study over the Rockies. The wind blows from left to right in this plot. The grey shading shows zonal wind and the contour lines indicate potential temperature. Note the lack of vertical displacement upwind of the first and second ridge from the left, yet GWs are observed above them. Also, note the weak cross-barrier winds between these peaks — characteristic of blocking.

Blocking creates a broad barrier that can produce GWs via alternative methods. Trüb and Davies (1995) provide a good overview of GWs that forms over a broad ridge (classified as having a halfwidth of up to a few hundred kms) for wind flow of differing Rossby numbers (third instance how blocking can help excite GWs). Geldenhuys et al. (2021) introduces a new mechanism where a broad ridge (halfwidth $\approx$1 500 km) pushes the tropospheric jet out of geostrophic balance as an indirect source for GWs (fourth instance how blocking can help excite GWs). Depending on the model resolution some of these GWs may be resolved, but that would require the blocking layer and the ridge to be adequately resolved.

3.5 Summary

This chapter summarises the results from Geldenhuys (2022). The chapter clearly illustrates a shortcoming in the current application of the GW physics in vicinity of low-level blocking. Current implementations reduce GW drag exponentially if blocking is present. Counting the air uplifted above the dynamic blocking barrier and exciting GWs, it is shown that blocking can induce GWs in five different ways. Not one of these mechanisms are currently implemented in models, meaning that drag due to these mechanisms is only represented in general circulation models, if their resolution is sufficiently fine to explicitly resolve the GW excitation. One possible solution will be to calculate the width of the blocking layer and see if any upwind topography exist. Another

option is to remove the dependency between the GW drag and the blocking layer depth in the model physics. This will still not be an accurate representation, but will be a step in the right direction. In order to observe this mechanism, 3-D low-level measurements of the blocking and the corresponding MTWs would be required.

Chapter 4

Data and Tools

This chapter provides an overview of observational data, model data and software tools used in this dissertation. A description of the extraction of the GW signals is included for each respective dataset. The chapter discusses how the observational data were retrieved and analysed to be discussed in the following chapters. The model experiment used in Chapter 6 is also briefly introduced here.

4.1 Campaigns

Both PGGS (POLSTRACC[1], GWEX[2], GW-LCYCLE and SALSA[3] (DLR, 2022a)) and SouthTRAC campaigns discussed in this dissertation were aircraft campaigns utilising HALO (the German High Altitude Long Range research aircraft). HALO is an initiative from the whole German atmospheric science community (DLR, 2022b). The aircraft is a G550 Gulfstream and is capable of more than 10 h flight time with a range over 10 000 km. The aircraft has a certified ceiling altitude of 15 km. The business jet was converted into a configurable scientific instrument carrier. The instrumentation can be adapted to the objectives of specific campaigns. Observations from two campaigns are used in this dissertation, namely PGGS and SouthTRAC — refer to Chapter 6 and Chapter 5 respectively for a description of these. Observations from two instruments onboard HALO are discussed in this dissertation, namely GLORIA and ALIMA.

[1] POLar STRAtosphere in a Changing Climate Oelhaf et al., 2019
[2] Gravity Wave EXperiment
[3] Seasonality of Air mass transport and origin in the Lowermost Stratosphere and the tropically controlled transition region using the HALO Aircraft

4.2 Instruments and observational data analysis

Observational data for this dissertation include data from the GLORIA and ALIMA instruments both situated onboard the HALO research aircraft. GLORIA was flown in both campaigns, while ALIMA was only flown in the SouthTRAC campaign. From GLORIA observations 3-D volumes of atmospheric temperature can be retrieved below flight altitude, while ALIMA observations provide temperature curtains above the aircraft.

4.2.1 GLORIA description — Gimballed Limb Observer for Radiance Imaging of the Atmosphere

GLORIA (Friedl-Vallon et al., 2014; Riese et al., 2014) is a limb imager mounted in the belly pod of HALO. The GLORIA spectrometer uses a Fourier transform spectrometer and measures infrared radiance (Fig. 4.1). The spectral range of GLORIA is from 780 to 1 400 cm^{-1}. The instrument comprises a Michelson interferometer with a 2-D infrared detector array. The 2-D infrared detector array consists of 256 $\times$ 256 elements. However, only 48 $\times$ 128 pixels of the detector are used to provide about 6000 simultaneous limb views. The use of the lower number of pixels in the detector is sufficient to allow a higher temporal sampling, allows a good data quality and greatly reduces the storage of data. The 2-D array allows for a vertical field of view of 4.1°. With this, GLORIA images altitudes from $\approx$5 km to slightly above flight altitude. Below $\approx$5 km the atmosphere becomes optically thick for infrared limb viewing measurements as the signal becomes saturated by the water vapour continuum. GLORIA looks to the right side of HALO with regards to flight direction and its field of view can be panned from 135° to 45° w.r.t. carrier heading in the horizontal. During the PGGS (SouthTRAC) case study, GLORIA was panned from 129° to 45° (49°) in steps of 4° (8°) resulting in 21 (11) azimuth angles.

GLORIA measures the integrated radiance emitted by molecules along the line-of-sight (Friedl-Vallon et al., 2014; Riese et al., 2014). Radiance emitted by molecules is based on the type of molecule, the amount of molecules and their temperature. The amount of molecules for a respective region along the line of sight depends on atmospheric density and the mixing ratio of the considered specie. Usually the densest part will have the most molecules, radiating the most energy. The tangent point is the region closest to the Earth's surface and generally corresponds to the region from which the most radiance is being emitted. The measured radiance signal is averaged over each row of the 2-D detector array and is the integral of the emitted light along the

line of sight. This means the signal is smeared along the line of sight. Without tomography (see next section), GLORIA can not adequately measure features of enhanced and reduced emission along the line of sight. If the line of sight spans across a higher emission and a lower emission region, an averaged value is measured where the signal from the emissions cancelled.

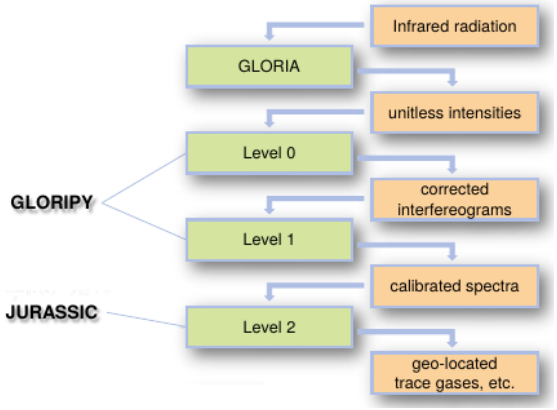

Figure 4.1: GLORIA processing chain and the software packages (GLORIPY and JURASSIC) used during analysis. Adapted from Krisch (2018)

GLORIA can measure with a spectral sampling of up to 0.0625 cm^{-1} (Friedl-Vallon et al., 2014; Riese et al., 2014; Ungermann et al., 2021). However, the finer the spectral sampling, the longer is the acquisition time needed to achieve this. A longer integration time implies a worse spatial sampling, as the aircraft is constantly moving. A lower integration time allows a finer spatial sampling but impacts the number of trace species that can be retrieved (as the spectral sampling is worse). Three main observation modes exist based on the integration time, namely low, medium and high spectral resolution modes (also known as Dynamics, Premier and Chemistry mode respectively — Tab. 4.1 (Ungermann et al., 2021)). Dynamics mode is a low spectral resolution mode originally designed for tomography. However, experiences learnt in the PGGS campaign resulted in an optimisation which resulted in the intermediate Premier mode.

Chemistry mode uses a spectral sampling of 0.0625 cm^{-1} for an increased number of detectable chemical species. Dynamics mode uses 0.625 cm^{-1} for an increased spatial sampling and to focus more on the retrieval of atmospheric temperature. Intermediate Premier mode employs a value of 0.2 cm^{-1} as a compromise. As HALO flies between 800 and 1 000 km h^{-1}, this translates to an along-track horizontal sampling (2-D curtain resolution) of 0.6 km for Dynamics mode, 1.1 km for Premier mode and 2.9 km for Chemistry mode. The resolution along the line of sight is 200–300 km (von Clarmann et al., 2009), but is increased for tomographic retrievals (Sect. 4.2.2).

Table 4.1: GLORIA measurement modes (Ungermann et al., 2021).

Mode	Panning angles/ stepsize (°)	Spectral resolution	Acquisition time (± 0.5 sec)
Chemistry	one fixed angle/0°	0.0625 cm^{-1}	13 sec
Dynamics	45-129°/4°	0.625 cm^{-1}	2.5 sec
Premier	49-129°/8°	0.2 cm^{-1}	5 sec

In this dissertation Dynamics mode and Premier mode are used. Premier mode was used in the first case study (SouthTRAC campaign — Chapter 5) and Dynamics mode in the second case study (PGGS campaign — Chapter 6). In both cases, the aim of the flight and the chosen GLORIA mode was to allow for tomographic retrievals.

4.2.2 GLORIA retrieval

Remote sensing data processing is typically divided into level 0, level 1 and level 2 processing (Fig. 4.1). Converting the raw and unitless measurement data into interferograms forms level 0 processing. Changing the interferograms into calibrated spectra takes place during level 1 processing (Krisch, 2018). Level 0 and level 1 processing is performed with the GloriPy software package (Kleinert et al., 2014; Ungermann et al., 2021). Finally, level 2 processing changes the spectra into geophysical data (Krisch, 2018) — from here on forward referred to as the retrieved quantities (e.g. temperature, ozone distribution, etc.). Each measured row of the 2-D detector array can be analysed for emission lines of gasses (Friedl-Vallon et al., 2014). GLORIA allows measurement and retrieval of amongst others, temperature, O_3, H_2O, NH_3, PAN, $ClONO_2$ and HNO_3. Level 2 processing is primarily done with the JURASSIC2 (Juelich Rapid Spectral Simulation Code version 2; Ungermann et al., 2010) software package.

Level 2 processing entails the reconstruction of an atmospheric state from calibrated radiance spectra, which is an ill-posed inverse problem[4]. To solve this inverse problem, an atmospheric state is iteratively adjusted by a Gauss-Newton type trust-region method (Ungermann, 2011). This continues until the synthetic measurements generated by a forward model agree within expectation to the actual measurements. The final state of this iterative process is then used as the 'retrieval' result (Krisch et al., 2017; Krasauskas et al., 2019). The first atmospheric state input into the forward model is called the a priori.

The a priori (first initial condition) consist of a smoothed reanalysis dataset of trace species

[4]If the problem does not have a solution, or it does not have a unique solution or the solution is not a continuous function of the input data, the problem is said to be ill-posed.

from ECMWF or WACCM (Whole Atmosphere Community Climate Model). All trace species have a known and unique emission spectrum. In this dissertation, the emission line parameters are obtained from the high-resolution transmission molecular absorption database (HITRAN) described in Rothman et al. (2013), which was updated in 2014. The emission spectrum (e.g. Fig. 4.2) provides an indication of which trace species (and what amounts) exist in the atmosphere. Figure 4.2 shows the trace gasses with an emission spectrum between 880 cm^{-1} to 1 000 cm^{-1}. It is this absorption spectrum that is modelled and compared to the observed spectrum.

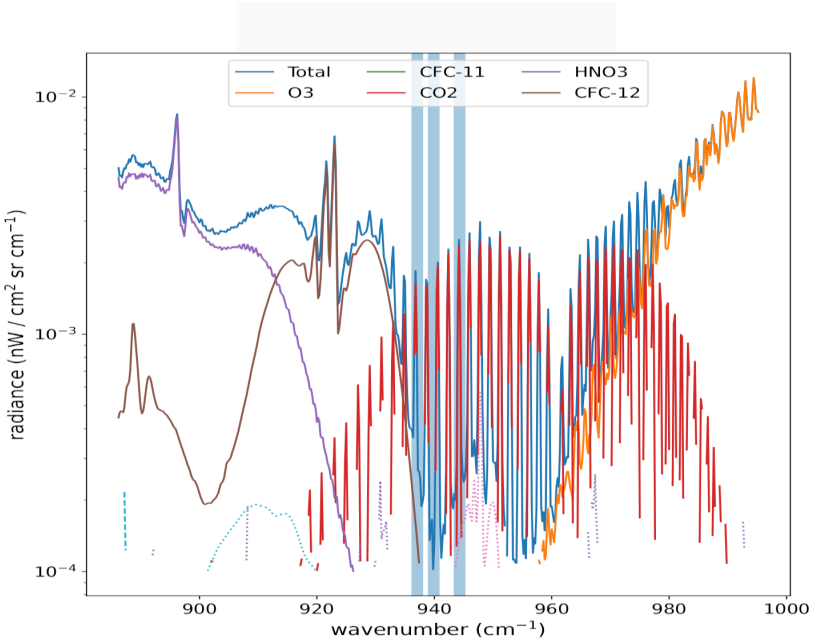

Figure 4.2: The ranges where the spectral samples are located which was employed to obtain the retrieval result for SouthTRAC flight 8 (Chapter 5). In the laser lines, CO_2 (red line) is virtually the sole contributor to the total radiance (blue line). The blue columns indicate the spectral windows used in the respective retrieval. The contribution of CFC-12 (brown) in the left most blue column is too small and can be neglected.

Comparing the modelled output to the observation emission spectrum occurs via a cost function (Krasauskas et al., 2019):

$$J(n) = (F(n) - o)^T \, {S_\varepsilon}^{-1} \, (F(n) - o) + (n - n_z)^T \, {S_a}^{-1} \, (n - n_a) \tag{4.1}$$

The first term of the cost function compares the actual measurements (e) to the simulated one ($F(d)$ provided for atmospheric state d). The expected instrument errors are represented by S_ε

(documented in Tab. 3.5 of Krisch et al. (2018)). The second term represents the regularisation term: within this term, information on the initial conditions (a priori) is introduced and assumptions about the inherent smoothness of the derived fields. The regularisation is calculated by the second-order derivative (Laplacian regularisation). The Laplacian regularisation replaced the traditional first spatial derivative regularisation approach. For an in-depth review of the Laplacian regularisation and the cost-function refer to Krasauskas et al. (2019). The cost-function is calculated after every forward model run to determine how the solution is converging to the observational spectrum.

To model the whole observed spectrum (780–1 400 cm^{-1}) might very well produce the best results, but would be computationally too expensive. To optimise the computation time the least number of spectral samples should be used to adequately retrieve the desired entities. Technically a robust retrieval only needs one emission line, but, GLORIA calibrations are imperfect and many unknown emitters exist in the atmosphere. For these reasons you want to model a peak and a nearby dip in the absorption spectrum of the retrieved trace species. Taking the difference between the two spectral samples is then assumed to belong solely to the emission of the targeted species. Another method of reducing computation time is to average several spectral samples and group into an integrated spectral window (this approach was followed to obtain the retrieval result discussed in Chapter 6).

The retrieval result generated for the PGGS case study (Chapter 6) was an evolution of Krisch et al. (2017), which was optimised to determine temperature, CCl_4, HNO_3, O_3 and aerosols. To optimise computation time, spectral regions were grouped into 16 integrated spectral windows (Tab. 4.2). Each channel can be associated with a different target quantity, namely 3 channels for temperature, 5 channels for CCl_4, 4 channels for HNO_3 and 4 channels for temperature and O_3 combined.

The ozone lines are known to be optically thick with interactions not fully understood. This results in a less accurate forward model. The result is that the retrieved signal can be placed at the wrong location along the line of sight, which complicates tomographic retrievals. Luckily, the SouthTRAC campaign allowed for a new set of spectral samples. The campaign was flown in an intermediate spectral resolution mode (i.e., Premier mode as opposed to Dynamics mode — Tab. 4.1), which allowed the use of the CO_2 laser lines. The lower spectral resolution of the PGGS campaign did not allow the use of the laser lines. The laser lines are optically thin and much more easily captured by the forward model. The retrieval for the SouthTRAC case study (Chapter 5)

Table 4.2: Spectral Windows used during retrieval of the PGGS case study in Chapter 6.

	Spectral Windows (cm^{-1})	Used to retrieve
1	790.6250 - 791.8750	Temperature
2	791.8750 - 792.5000	Temperature
3	793.1250 - 793.7500	CCl_4
4	794.3750 - 795.0000	CCl_4
5	795.6250 - 796.2500	CCl_4
6	796.8750 - 797.5000	CCl_4
7	798.1250 - 799.3750	CCl_4
8	883.7500 - 888.1250	HNO_3
9	892.5000 - 896.2500	HNO_3
10	900.0000 - 903.1250	HNO_3
11	918.7500 - 923.1250	HNO_3
12	956.8750 - 962.5000	Temperature
13	980.0000 - 984.3750	Temperature, O_3
14	992.5000 - 997.5000	Temperature, O_3
15	1000.6250 - 1006.2500	Temperature, O_3
16	1010.0000 - 1014.3750	Temperature, O_3

was set to retrieve temperature and a radiance background only. Spectral samples were used in the ranges between 936.8–938.6 cm^{-1}, 939.2–941.0 cm^{-1} and 942.4–944.2 cm^{-1} (Fig. 4.2). In the laser lines, the peaks and dips in the absorption spectrum are close to one another, meaning grouping similar spectral samples into a spectral window is not worth it. Hence, the forward model for the SouthTRAC case study retrieval used the spectral resolution of 0.2 cm^{-1}. This case was the very first tomography case study that used the laser lines for the retrieval.

A 1-D GLORIA retrieval consists of a temperature signal that was averaged over each row of the detector array for each respective line-of-sight. A 1-D retrieval converts single radiance profiles into temperature profiles by assuming a horizontal homogeneous atmosphere. The 1-D dataset is combined with the aircraft direction of travel to create a 2-D curtain. The first dimension represents time and the second altitude. The retrieved result of each row average is represented by its tangent point along the line of sight. The SouthTRAC case (the only case that used 2-D data in the discussion — Chapter 5) produced 11 different 2-D datasets from each of the azimuth angles. The GW perturbation was extracted from the 2-D dataset by subtracting a smoothed ECMWF temperature (also the a priori of the retrieval). To obtain a 3-D retrieval, tomography is required.

Tomography employs multiple views from different angles to examine a given target area. Tomographic measurements utilise the panning ability of GLORIA. The different azimuth angles provide multiple measurements of the same air mass from different angles. Data from different angles allow for a tomographic retrieval with the help of JURASSIC2 (Ungermann et al., 2010)

software packages. Both tomographic retrievals were conducted using a Delaunay triangulation-based, irregular grid-capable discretisation (Krasauskas et al., 2019). The Delaunay technique allows an adaption of grid density to atmospheric features and measurement density. A reduced number of grid points means a lower computational cost of tomographic retrievals.

Two types of tomographic measurement are acquired by GLORIA, namely full-angle tomography (FAT) and limited-angle tomography (LAT) (Krisch et al., 2018). During FAT, the aircraft follows a closed (e.g. circular or hexagonal) flight path around the area of interest. An aircraft that flies in a straight line only allows LAT (used to obtain the retrieval data for this dissertation). Linear flight patterns allow fewer angles to observe the area of interest (Krisch et al., 2018, 2020). This decreases the amount of measurements that can be used as input to determine the atmospheric state. It is to be expected that fewer measurements available to constrain the mathematical model will result in a product with a lower accuracy. For this reason LAT retrievals are more difficult and frequently show more artefacts. The resolution of LAT is also slightly worse compared to FAT. Krisch et al. (2017) observed a maximum horizontal resolution of 20 km for FAT. The vertical resolution of our LAT is 200 m. The horizontal resolution of LAT is $\approx$30 km in the along flight direction and $\approx$70 km perpendicular to the flight direction (Krisch et al., 2018). It is known that in cases the wave orientation can be turned to be more perpendicular to the flight path during LAT. Naturally, FAT is preferred with better resolution and fewer artefacts. However, experimental design during flight planning do not always allow for this as FAT flight patterns take substantially longer. To examine the robustness of our results, we tested different retrieval configurations. We found the derived temperature product to be robust within the region of high tangent point density, whereas other parts of the volume were subject to large differences depending on the chosen a priori or regularisation (Geldenhuys et al., 2021; Krasauskas et al., 2019).

4.2.3 ALIMA - Airborne Lidar for the Middle Atmosphere

ALIMA measures the atmospheric density profile from which temperature is calculated (Rapp et al., 2021). ALIMA is an iron resonance and Rayleigh lidar, however, during the SouthTRAC campaign, only the Rayleigh lidar was installed. Within the HALO body there is an optical window, which allows ALIMA to look upwards. Under ideal conditions ALIMA measures from 2 km above flight altitude up to 80 km by Rayleigh scattered light.

To measure up to 80 km requires a strong initial pulse and multiple fine-tuned detectors. ALIMA provides an initial pulse of light at 532 nm wavelength and receives backscatter by a telescope

48 cm in diameter (Rapp et al., 2021). The detected backscattered light has a large dynamic range. Thus, ALIMA uses three detectors with different sensitivities that are optimised for the near, mid and far region. A mechanical chopper blocks the intense backscattered light originating within 4 km above the aircraft in order to prevent overloading of the the detectors. The mid and far detectors are gated relative to the opening of the chopper to avoid saturation.

Following Hauchecorne and Chanin (1980) the lidar profile from each detector is converted to a temperature profile by hydrostatic downward integration in steps of 100 m. This requires a top of profile temperature for the highest profile of a measurement sequence, which is taken from SABER satellite data. The top of profile temperature of the lower profiles is taken from the above profile. The three profiles are then merged into a single profile covering the whole altitude range (Kaifler and Kaifler, 2021). At the top of the profile, the error can be large, but since pressure increases exponentially downward, the error similarly decreases exponentially downwards. The error decreases from 6.5 K above 70 km to 2.9 K between 60–70 km to 0.9 K below 60 km (Rapp et al., 2021). Temperature data used in Chapter 5 are taken at 1 min resolution, which roughly equates to $\approx$15 km horizontal resolution.

To obtain a curtain of GW perturbation, a 30 min running mean temperature is subtracted. Removing the background temperature reveals a complex GW structure exhibiting GWs of different scales and different propagation directions. Wavelet analysis was used to further analyse this complex interference pattern. Wavelet analysis has been applied to lidar data before to separate GWs of different orientations (Kaifler et al., 2017). Assuming non-stationarity on the straight flight legs a 2-D Morlet continuous wavelet transform (e.g. Torrence and Compo (1998)) was computed according to Chen and Chu (2017), using a Morlet oscillation parameter (k factor) of $2/\pi$. We found a discretisation starting at a spatial scale of 40 km while using 20 spatial and 30 angular scales sufficient in order to separate different slants of GW phase fronts. By making the assumption that the GWs propagate against the model wind we determine upward and downward propagating GWs.

The 2-D Morlet continuous wavelet transform is much better equipped than the fast Fourier transform to deal with non-harmonic waves, but there are still some inherent problems visible in the derived amplitudes. An amplitude signal of an upward propagating non-harmonic GW will leak to the downward propagating GW, lowering the 'real' temperature amplitude of the upward propagating GW. For this reason, all temperature amplitudes were determined using temperature perturbation components before application of the continuous wavelet transform.

4.3 Reanalysis data and model integrations

This dissertation uses multiple model and reanalysis datasets. Unless otherwise stated, ERA5 (ECMWF Reanalysis 5th Generation Description) data are utilised. Multiple model datasets were used. Weather Research and Forecasting model (WRF) data are used in Chapter 5 and high-resolution ECMWF data are used in Chapter 6.

4.3.1 ERA5 reanalysis

ERA5 (Copernicus Climate Change Service (C3S), 2017; Hersbach et al., 2020) data originates from a frozen version of the ECMWF IFS, which consists of a general circulation model and assimilation system. The frozen version creates a dataset using an identical physics package and constant spatial resolution making it consistent through time. The generic model consists of 137 levels on a high-resolution hybrid grid. For ease of use the above mentioned format was interpolated to a $0.3^\circ \times 0.3^\circ \times 200\,\text{m}$ grid. All ERA5 data used in this dissertation is on a geopotential height grid, with exception of the synoptic discussions and the calculation of the cross-stream ageostrophic wind (Figs. 6.5 and 6.6), which was calculated on a pressure grid.

The ERA5 data were separated into GWs and the large-scale background state. To remove the GW component from the background flow a zonal Fast Fourier Transform was used with a cut-off at zonal wavenumber[5] 12 (Strube et al., 2020). This was followed by a Savitzky-Golay (Savitzky and Golay, 1964) filter in the y- and z-direction. In the meridional (y) direction a third-order polynomial with a 50 point (15°) smoothing was applied. In the remaining direction (z) a fourth-order polynomial was applied with a 15 point (3 km) smoothing. The result after smoothing produces the background conditions. Subtracting the smooth background conditions from the original field produces the GW perturbation component. In all instances, the smooth background fields were visually studied to ensure no GWs signals were left in the field.

4.3.2 High-resolution ECMWF analysis data

To investigate the influence of orography on the GWs in Chapter 6 two global model forecasts with ECMWF IFS are discussed: i) CTL-run and ii) T21-run from Sect. 6.4. The model is constrained by data assimilation, which provides a more realistic analysis dataset. The forecasts are performed at TCo1279 horizontal resolution (corresponding to 9km grid-spacing on a cubic octahedral grid)

[5] At first a zonal wavenumber of 18 was used, but this proved inefficient and left some GW signals in the background data

with 137 vertical levels and use the operational ECMWF IFS configuration of cycle 45r1 (ECMWF, 2022). The only difference in the two runs is the resolved orography field, which in CTL-run is at TCo1279 resolution and in T21-run at T21 resolution. This means that the orography in the T21-run is much smoother, does not resolve, for instance, Fjords at the Greenland coast and represents only 60% of the TCo1279 orography field elevation. The two forecasts were initialised on 9 March 2016 at 12:00 UTC and run freely for 72h (the GW observation takes place 30h after initialisation). The GW perturbation was removed from the background flow similar to the method described for ERA5 data (Sect. 4.3.1).

4.3.3 WRF (Weather Research and Forecasting) model data

A high-resolution WRF model (version 4.2) is used to fill the data gaps when validating the raytracing and ALIMA results in Chapter 5. Boundary input conditions were supplied every 6 h at a 0.25° × 0.25° resolution from the Global Data Assimilation System (GDAS) from the National Centres for Environmental Prediction (NCEP). The WRF model was nested twice to produce a 9 km and ultimately a 3 km grid point distance. Vertical resolution was 0.5 km. The data extends from the surface to 42 km with a 10 km sponge. Only data below the sponge layer (32 km) were used in Chapter 5. The model spin-up time[6] was one day — only data after spin-up time was used.

The nested model implies that the data does not cover the whole globe and GW extraction is more complex. This means that the standard background removal employed for ECMWF and ERA5 data will not work. To separate GWs from the background fields a 2-D Fast Fourier Transform was used. The spectrum was cut at a horizontal wavelength of 400 km, retaining all shorter wavelengths in the perturbation part. Experiments with a 600 km cut-off produced similar GW perturbations revealing that the 400 km cut-off is sufficient.

4.4 GROGRAT — Gravity-wave Regional Or Global Ray Tracer

GROGRAT (Marks and Eckermann, 1995; Eckermann and Marks, 1997) is a raytracing tool that traces the propagation path of a GW and can be used for both forward and backward tracing. GROGRAT is based on the GW dispersion relation described by Eq. 2.6. A GW packet is fully characterised by its state vector, which consist of its position in space (x, y, z), time (t) and its 3-D wave vector (ω_{gb}, k, l, where subscript gb indicates ground-based). The raytracer projects this

[6] Time it takes for a forcing like the wind to induce velocities to the value of 63.2% of long time values.

state vector forward or backwards according to the raytracing equations (Lighthill, 1978):

$$\frac{\partial x_i}{\partial t} = \frac{\partial \omega}{\partial k_i}, \tag{4.2}$$

$$\frac{\partial k_i}{\partial t} = -\frac{\partial \omega}{\partial x_i}, \tag{4.3}$$

where the index i denotes the spatial direction (x, y, or z) or its corresponding wavenumber (k, l, or m), and $\frac{\partial}{\partial t}$ is differentiation in time.

In this study, the 4-D version of GROGRAT is used. This means that the background temperature, wind and pressure change with time (see Sect. 4.3.1 to see how the background state was determined). For each time step of the ray integration the group velocity and state vector change. Along the ray path, wave action density[7] ($A \equiv \frac{\bar{E}}{\omega}$) is conserved, but GW saturation as well as GW dissipation are taken into account. GROGRAT compensate for GW saturation and dissipation based on Marks and Eckermann (1995) (partly discussed in Sect. 2.4), while employing radiative and turbulent damping based on the scheme developed by Zhu (1993). Gravity wave amplitudes are converted from wave action.

For backtracing, it is important to keep in mind that the GW can be emitted at any point along the ray, and is not necessarily emitted at the endpoint of the ray (Preusse et al., 2014). One indication of a GW source along the ray is a violation of the Wentzel-Kramers-Brillouin (WKB) approximation (Hertzog et al., 2001). The GROGRAT implementation of the WKB approximation requests that the scale of change of the wavenumber is large compared to the wavelength of the GW. This is tested via the parameter (Eq. 5 of Marks and Eckermann (1995))

$$\delta = \frac{1}{m^2}\left|\frac{dm}{dz}\right|. \tag{4.4}$$

The GROGRAT propagation physics is complete (as far as WKB allows) and comprehends in particular horizontal propagation and refraction. However, some non-linear effects along the path are not captured by GROGRAT.

GROGRAT contains different physics packages. In this dissertation the 'normal' raytracing

[7] where $\bar{E} = \frac{1}{2}\rho(\frac{\hat{T}}{T})^2(\frac{g}{N})^2\frac{\omega^2}{\omega^2-f^2}$, here $\hat{T}$ is temperature amplitude and T is temperature

settings refer to 4-D propagation (similar to the setup used in Krisch et al. (2017, 2020); Strube et al. (2021)). In Chapter 5 alternative 3-D and 1-D propagation setups are used to compare to the 4-D propagation results. The 3-D propagation setup assumes the background constant in time and uses a single snapshot to propagate the GWs. The 1-D setup represent conditions when horizontal propagation and refraction are both disabled by setting the horizontal phase speed as well as $\frac{dk}{dt}$ and $\frac{dl}{dt}$ (Eqs. 2.15 and 2.16) to 0. This is analogous to a 1-D parameterisation scheme employed in a general circulation model.

Chapter 5

SouthTRAC campaign: The physics of GW refraction

Refraction acts during GW propagation (Fig. 2.1) and takes place as the orientation of the GW changes. Literature reveals a few articles showing the importance of refraction (e.g. Durran, 2009; Sato et al., 2009) and a few articles provide indirect proof of refraction (e.g Preusse et al., 2009; Ehard et al., 2017), however, no articles could be found to exhibit direct observations of refraction. This chapter uses high-resolution observations from GLORIA and ALIMA obtained during SouthTRAC to study GW refraction. Firstly, this chapter intends to use the high-resolution observations and to test the raytracing equations put forth by the theoreticians. Secondly, this chapter investigates the effect of refraction on the location and amount of GWMF deposition. This is in an attempt to shed more light on the missing GW drag at 60° S.

5.0.1 SouthTRAC

The SouthTRAC campaign was based in Patagonia, with its base in Rio Grande, Argentina. Measurements were taken around South America and Antarctica during two phases. The first phase in September/October 2019 and the second phase in November 2019. In total 26 flights (Fig. 5.1) took place; ≈68 000 km in the first phase and ≈20 000 km in the second phase.

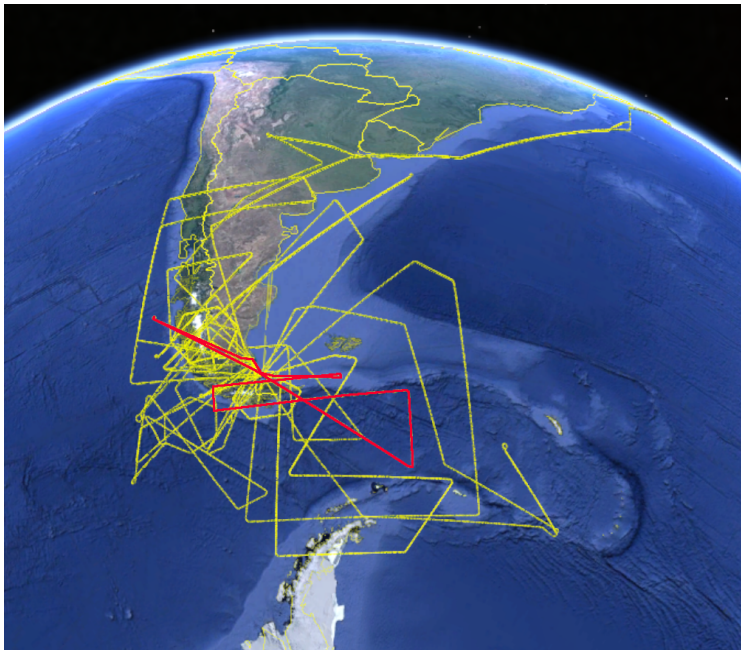

Figure 5.1: Compilation of flights during SouthTRAC surrounding southern parts of South America and the Antarctic Peninsula. The flight indicated in red is discussed in this chapter.

The GW phase of SouthTRAC aimed at studying GWs propagating into the polar vortex at the world's GW hotspot, the Southern Andes (Rapp et al., 2021). During phase one, eight flights were conducted with GW related objectives and one flight during phase two. Most flights were conducted at night to allow the lidar maximum observational altitude. This chapter mainly discuss a flight from phase one.

The detailed GW objectives of the SouthTRAC campaign included:

1. perform coordinated observations throughout the atmosphere,
2. gain improved understanding of horizontal and vertical propagation of mountain waves,
3. do high-resolution measurements and compare with high-resolution models on a case study basis,
4. explore GW breaking and dissipation, and
5. compare GWs over different measurement techniques.

The flight discussed in this chapter was the first GW science flight of the campaign and provided some of the last high propagating GWs for the season (see Sect. 5.1). This flight focused on GWs originating from the Antarctic Peninsula and drifting into the Drake Passage. Flight eight was ≈8 h and over ≈6 500 km long (Fig. 5.1).

Experiment design forms a very important aspect of campaigns. One of the instruments on-board HALO (the ALIMA instrument — see Sect. 4.2.3 for description) can only provide a 2-D dataset. On the one hand, a curtain observation does have a slight disadvantage as opposed to a 3-D dataset. But on the other hand, with creative experiment design (flight planning) this is easily overcome. To create a 3-D picture of the GWs, the flight planning team planned for a racetrack with two parallel flight tracks (Fig. 5.2) spaced less than one expected wavelength of the major GW structure. This would provide a 3-D picture of the GW field.

5.1 Synoptic Situation

The research flight took off on 11 September 2019 at 23:00 UTC and landed on 12 September 2019 shortly before 07:00 UTC — all times in this chapter are in UTC. The plan was to fly north west of Rio Grande and upstream of the Andes, the next leg was directed along the 1 hPa jet stream to the middle of the Drake Passage. This leg was primarily for ALIMA to measure the GWs that propagate above the flight path along the jet maxima and is not discussed in this chapter. The observations discussed in this chapter were performed between 03:30 and 06:30 when the racetrack[1] was flown. Observations used in this chapter are from the long parallel legs of the racetracks (red lines in Fig. 5.2). The southern leg was flown first from east-to-west followed by the northern leg from west-to-east. We choose 03:00 on 12 September 2019 to be representative for the synoptic situation of the racetrack.

The cold front (Fig. 5.2) passed over Rio Grande $\approx$5 h before flight take-off. The cold front is situated in a well developed Rossby wave at 500 hPa. Behind the cold front, cold stable air is advected onshore by a ridging high pressure system. This creates south-south-westerly flow over the southern most tip of Patagonia, veering to south-west (at 50° S), west-south-west (at 45° S) and west (at 40° S) in a northwards direction along the Andes mountain range. The stable conditions with wind flow nearly perpendicular (within 30°) across the mountains (ICAO, 2005; Geldenhuys et al., 2019) creates prime conditions for a whole spectrum of differently orientated GWs entering the observation regime. Smaller mountains on the tip of Patagonia are expected to form shorter horizontal wavelengths. The broad Andes ridge to the north is expected to excite long horizontal wavelengths with possible shorter waves coming from the side ridges leading up to the main ridge (Van der Mescht and Geldenhuys, 2019). All of these GWs are expected to

[1] A flight pattern consisting of two legs parallel to one another.

superimpose and to create a rather complex interference pattern.

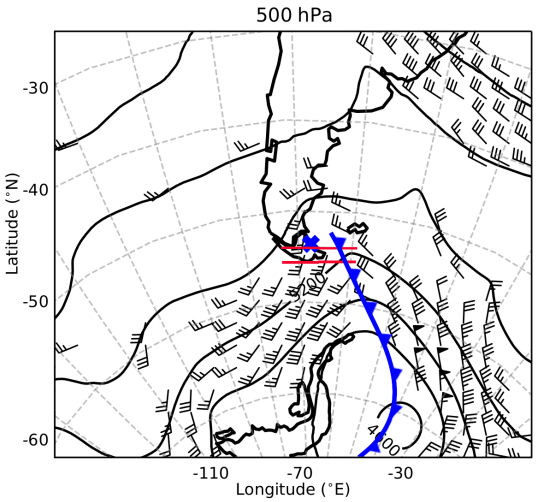

Figure 5.2: Synoptic situation in the mid-troposphere at 500 hPa on 12 September 2019 at 03:00 as indicated by ERA5. Black lines show geopotential height lines. Wind barbs only show wind where the total wind speed exceed 20 m s^{-1}. A short barb indicate 5 m s^{-1}, a long barb 10 m s^{-1} and a triangle 50 m s^{-1}. Note the Rossby wave with the cold front (blue line) directly downstream of Patagonia. The blue cross indicates the take-off location (Rio Grande) and the red lines over the southern tip of South America show the parallel racetrack legs used in the GLORIA and ALIMA retrievals.

Polar stratospheric clouds formed presumably in the GWs coming from the broad main ridge. The clouds were observed in the racetrack at 23 km altitude by ALIMA (Dörnbrack et al., 2020). Enhanced backscatter from the clouds means that ALIMA temperature measurements can only be used above this altitude. The polar stratospheric clouds extended unusually far north. This was attributed to a displaced stratospheric polar vortex.

In the stratosphere a significant event occurred, namely a sudden stratospheric warming (Shen et al., 2020). This minor sudden stratospheric warming was a displacement event (Fig. 5.3) forced by a bottom-up mechanism: an anomalously strong wavenumber 1 activity propagating upwards from the troposphere. The strong wavenumber 1 activity was in turn forced by anomalously strong convection over the Pacific Ocean. The sudden stratospheric warming caused a rapidly weakening polar vortex with temperatures increasing rapidly from above to below. Both the weakening in the wind and the strong change in temperature is unfavourable for GW propagation and cause GW dissipation or the trapping of GWs. Both of these act as a lid to restrict the GW activity moving upwards.

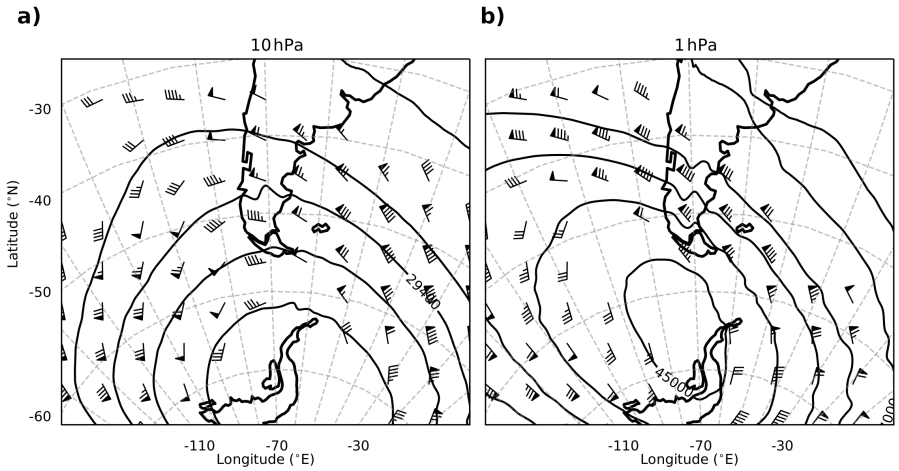

Figure 5.3: Stratospheric synoptic situation at 10 hPa (a) and 1 hPa (b) on 12 September 2019 at 03:00 as indicated by ERA5. Black lines and wind barbs are similar to Fig. 5.2. Note that the polar vortex is displaced from the pole with its centre located at 70° S 60° W at 10 hPa and 65° S 75° W at 1 hPa.

The slow down in the 10 hPa zonal average winds appeared in the first few days of September 2019[2]. By 11 September 2019, the slow down had merely started and still allowed GW propagation to vortex altitudes. This is confirmed by the strong westerly winds shown in ERA5 data on Fig. 5.3. The location of the polar vortex creates a large amount of wind speed and directional shear. The shear is expected to form prime conditions for refraction, however the reader is to keep in mind that winds during this event are not representative of the normal this time of year.

5.2 GW Observations: Tropospheric and Lower Stratospheric

The viewing geometry of GLORIA on its carrier HALO allows tropospheric and lower stratospheric observations. The southern leg of the racetrack (Fig. 5.2) was used in the GLORIA retrieval and was flown from east to west at 13.5 km. Using both the northern and southern leg in a combined tomographic retrieval created artefacts due to the non-symmetrical tangent point distribution. A retrieval using only the northern leg produced a GW field similar to the southern leg.

[2]Using data from MERRA-2 (Modern-Era Retrospective analysis for Research and Applications — Gelaro et al. (2017)). MERRA-2 data are used as it assimilates MLS (Microwave Limb Sounder) satellite data, which makes it a more trustworthy dataset in the upper stratosphere and lower mesosphere (Ern et al., 2021).

5.2.1 GLORIA Observations: 3-D

The 3-D GLORIA temperature field is obtained from a 3-D tomographic retrieval. The retrieval reveals short horizontal wavelength GWs in the lee of the south western most tip of Patagonia. The horizontal cut in Fig. 5.4 shows two distinct GW orientations. The first is aligned west-east and the second from north-west-to-south-east. Taking the GLORIA viewing geometry into consideration we theoretically have less trust in the west-east orientated feature. The viewing angles of GLORIA are aligned across the phase fronts — for example the 49° and 73° viewing angles on Fig. 5.4.

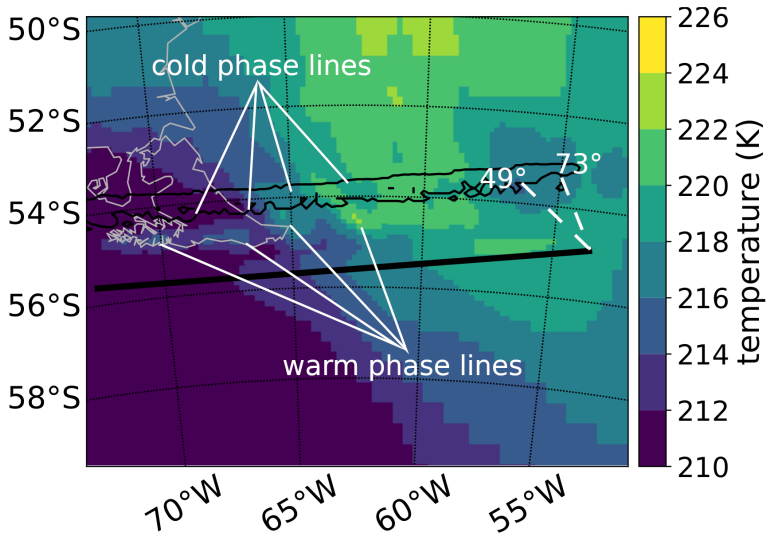

Figure 5.4: Horizontal cut at 10 km altitude of the GLORIA tomographic field. Outside the retrieval volume the temperatures fall back to the a priori. The retrieval was computed using data only from the southern leg — thick black line. Thin white solid lines indicate the Patagonia coastline and the straight white solid lines point to different phase fronts. The thin black line indicates our tangent point region for this altitude, which is our region of trust (Sect. 4.2.1). The dashed white lines indicate the maximum and minimum angle of the GLORIA field of view discussed in Fig. 5.5.

If the line of sight spans across a positive and a negative temperature anomaly, the signal will be an averaged value of emissions from both regions. The amount that each feature contributes depends on the density. The densest part will have the most molecules, radiating the most energy. For example, the 49° azimuth angle on Fig. 5.4 is aligned along the eastern most indicated warm phase front. In this instance we expect a maximum temperature amplitude. Viewing the westernmost indicated phase front means we look at both a warm and a cold phase front. This means the warm and the cold phase fronts average out to have a weak signal, i.e. no retrievable GW. Considering this with the fact that this is a limited angle tomography case, we are surprised

how well we can see these structures parallel to the flight path (the westernmost indicated warm front on Fig. 5.4). The high-resolution WRF model (Sect. 4.3.3 and 5.2.3) confirms this structure also exists. This adds trust to the retrieval process (and the complex physics and mathematics behind it), when the result is better than what simplified physics dictate it should be.

The second GW orientation is aligned north-west-to-south-east. Horizontal cuts at different altitudes similar to Fig. 5.4 and a vertical cut perpendicular through the GW phase fronts reveal a horizontal wavelength of 116 km, vertical wavelength of 4.4 km, amplitude of $\approx$3 K and an orientation of 230°. Krisch et al. (2018) found that limited-angle tomography (method used to produce the 3-D retrieval while flying on straight legs) enhances the uncertainty/error of the phase front orientation. Considering that orientation is important in a refraction study, we complement the orientation results with the 1-D retrieval.

5.2.2 GLORIA Observations: 1-D

Each GLORIA viewing angle produce a different 2-D curtain (Sect. 4.2.2). Each viewing angle observes the GW phase front differently (Fig. 5.5). Where the viewing angle aligns along the GW phase front a greater signal is obtained, as opposed to looking across the phase fronts at an angle. Looking across a succession of GW phase fronts dampens the wave amplitude in the observed radiance (Preusse et al., 2002). For a specific altitude the maximum temperature amplitude is reached when the line of sight and phase fronts are aligned. The viewing angle of the most pronounced signal is then used for the wave orientation with an error of half a scanning step (4°) as error estimate.

At 8 km altitude the maximum amplitude in Fig. 5.5 is observed for an angle of 65°. The maximum at 10 km occurs at 57° and at 12 km at 49°. Taking into account the aircraft heading of 268° and subtracting 90° to convert from phase-front orientation to wavevector, we obtain a ground-based orientation of 243° for the 65° viewing angle. Satellite data from GOES (Geostationary Operational Environmental Satellite — not shown) channel 8 to 10 indicate a GW orientation of $\approx$240° between $\approx$615 hPa ($\approx$4 km) and 340 hPa ($\approx$8 km), consistent with the lowest GLORIA altitude. Accounting for the fact that amplitudes are maximum at different altitudes for different GLORIA viewing angles, we can conclude that at higher altitudes (Fig. 5.5) the orientation turns anticlockwise to 235° at 10 km and $<$227° at 12 km (GLORIA has no viewing angles lower than 49°, which means the orientation can be lower than 227°). Assuming one wave packet with a fixed orientation at launch, the refraction between 8–12 km is at least 16°.

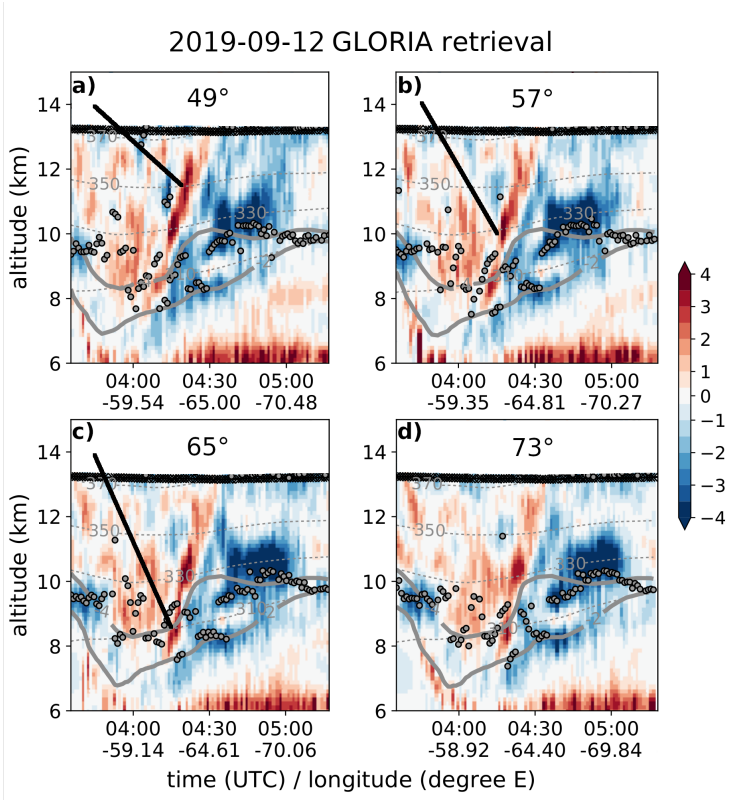

Figure 5.5: Temperature perturbations (in K) from GLORIA 1-D observations for 4 of the 11 azimuth angles: 49°, 57°, 65°, and 73°. Angles are respective to HALO flight path from forward to backward and 49° as well as 73° angles are shown on Fig. 5.4. Note how the maxima of the warm phase front at fixed altitudes depend on the viewing angle (marked by thick black line). The thick grey lines indicate dynamic tropopause at -2 and -4 potential vorticity units and the thin dashed grey lines show potential temperature — both extracted from ECMWF analysis data. The dots indicate the suggested thermal tropopause as determined from the retrieval, however, the gravity wave signature will influence this. Data is valid for the southern leg of the racetrack and longitude values represent tangent point longitude.

5.2.3 Raytracing and WRF comparison

In this section GROGRAT is checked for consistency to ALIMA and WRF before subsequent experiments are conducted (Sect. 5.4.2). The GROGRAT input was obtained from the GLORIA observations (Sect. 5.2.1) and the dispersion relation (Eq. 2.6). To account for the measurement error the input values are perturbed by 10% to form an ensemble raytrace. Tracing the ensemble backwards in time produces a spread of rays surrounding the south coast of Patagonia (Fig. 5.6 — the yellow region includes all but one ensemble member (the perturbation associated with a shorter vertical wavelength propagated to 58.5° S 75.5° W and was neglected in the spread)). All ensemble members end within close vicinity in the horizontal and vertical to the coastal mountains (Fig. 5.6). This is a key indicator that the complex mountains on the south coast of Patagonia

are the source of the GWs. GLORIA observed the GWs ≈5 h after formation. The GROGRAT suggested horizontal wavelength, vertical wavelength and phase orientation agrees well with the ERA5 data. The consistency generates trust in the features seen in observations, GROGRAT and ERA5.

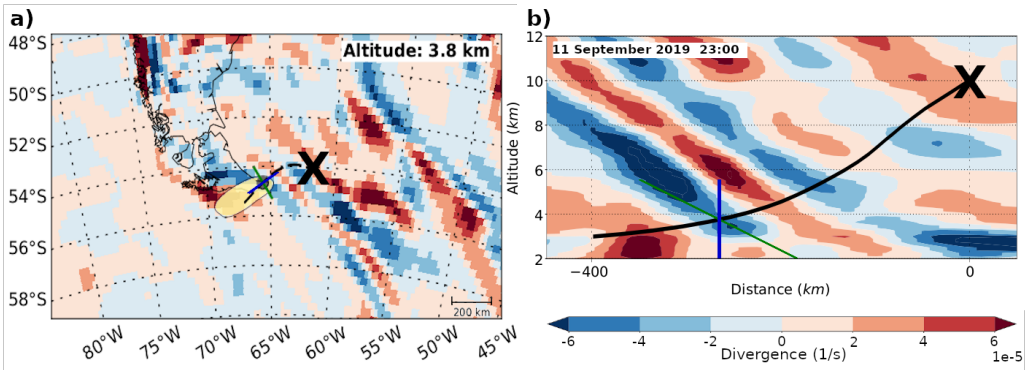

Figure 5.6: GROGRAT backtrace using GLORIA observations as input overlaid on horizontal wind divergence from ERA5. The raytracing starts at 03:00 on 12 September 2019 at 10 km and traces back ≈5 h. Both panels (a) and (b) are valid for 23:00 — 4 h before observation. Panel (a) shows a horizontal cross-section with the ray as a dashed line and ERA5 divergence at 3.8 km. The yellow transparent region surrounding the end of the ray shows the spread of the ensemble members. The thin black line represents the coastline and the X the start of the ray. Panel (b) shows the vertical cross-section as interpolated along the ray (black line). The location of the GW packet for this respective time is indicated by the cross of the blue and green line. The blue line on the left (right) plot shows the GROGRAT suggested horizontal (vertical) wavelength. The green line shows the phase orientation.

The forward raytrace of the GW observed by GLORIA is compared to ALIMA for further verification. The ray remains below the ALIMA observational range and reaches ALIMA observational altitudes south of the racetrack (Fig. 5.7). The ray takes ≈3 h to propagate from the observation altitude to 27 km. Time wise this makes the raytrace directly comparable to the WRF data at 06:00 on 12 September 2019. The ALIMA southern leg was flown east to west between 03:30 and 05:20 and hence 40 min to 2.5 h before the time the WRF model is evaluated. The comparison relies on the assumptions that the GW structure (phase and amplitude) does not alter in this time frame.

The reconstructed GROGRAT GW in Fig. 5.7 compares well to the WRF and ALIMA data. It is noted that the eastern most part of the leg has the biggest time difference between the ALIMA observation and the GROGRAT GW, hence we could expect differences. Between 62° and 68° W the WRF model and ALIMA compares remarkably well. The WRF data fills the gaps between ALIMA measurements and the reconstructed GROGRAT GW making it a useful dataset. Using the ALIMA data by itself becomes complicated as there are many short horizontal wavelength GWs (e.g. between 62° and 68° W), which is difficult to interpret using only the two ALIMA curtains.

The WRF model simulates the shorter horizontal wavelength GWs well, which makes it easier to interpret the ALIMA data.

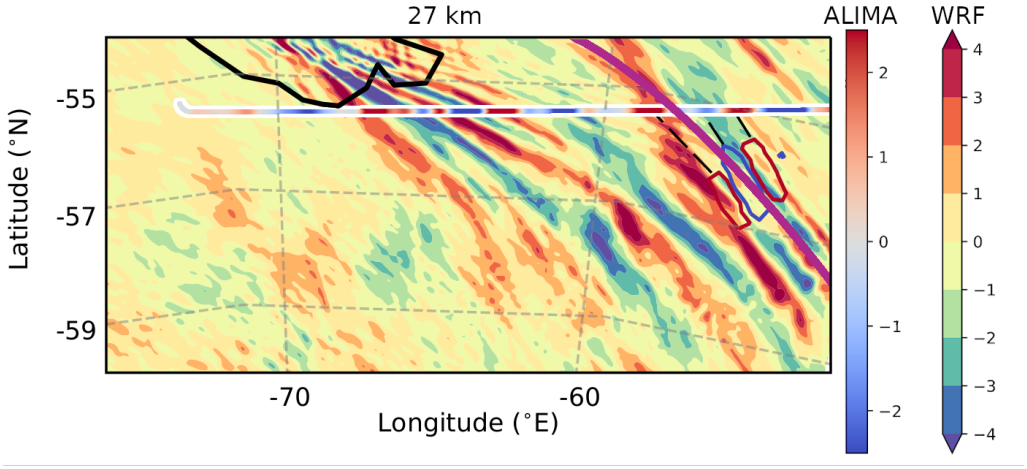

Figure 5.7: The forward raytrace (magenta line) of the GLORIA observed GW overlaid with WRF and ALIMA data. All data are valid for 27 km. The background data is WRF data while the red and blue line with the white border represents ALIMA data on the southern flight track after the upward propagating waves were selected with a wavelet transform (Sect. 4.2.3). The red and blue contour lines show warm and cold phases of the reconstructed GROGRAT GW based on GLORIA observations respectively. The reconstructed GWs and WRF data are both valid for 12 September 2019 06:00. To guide the eye, the black-dashed lines create a link between GROGRAT reconstruction and the ALIMA track, which shows that the phase fronts of the GW match well. The plot is exclusively used to match the GW structure and validate GROGRAT versus ALIMA. Note that the temperature (in K) scale are different for WRF and ALIMA — the wavelet transform would cause the ALIMA temperature amplitude to be lower than the actual amplitude (Sect. 4.2.3).

5.3 GW Observations: Mid- and Upper Stratosphere

In the following discussion we use data from 04:15 to 06:05, this implies assuming a stationary environment for ≈2 h in the combined analysis. We initially assume the GW structure is stationary and test this with every GW packet we observe. The temperature perturbation field shown in Fig. 5.8 were determined by subtracting a 30 min running mean and applying a wavelet transform as specified in Section 4.2.3. Three GW families are identified in the ALIMA curtains on Fig. 5.8. The southern leg (Fig. 5.8a) shows two long horizontal wavelength GWs. A first wavepacket (family 1) has a top at ≈40 km and starts 32 km — with a weak signature extending down to 27 km (the GWs on Fig. 5.7). Compared to family 1, the phase fronts of the higher wavepacket (family 3) have a steeper slant, show a shorter horizontal wavelength and a smaller GW amplitude. The 'dead zone' (weak amplitudes and an incoherent structure) between these packets and the differences in the GW properties indicate that these are two distinct GWs. Horizontal cuts through

the ALIMA data (similar to Fig. 5.9) show a well defined GW pattern that disappears around 40 km. This is further evidence of two GWs rather than structures of the same GW packet.

The northern leg (Fig. 5.8b) exhibits three dominant GW packets. The first GW packet exhibits strong similarities to family 1 (in the southern leg) in the left plot and is categorised as the same GW packet. Above family 1 (in the 'dead zone' of the southern leg in Fig. 5.8a) another GW packet is identified (family 2). This GW packet has no similarities to family 1 or 3 and is hardly discernible in the southern leg (mainly at flight distances $< 700km$). This suggests that the GW packet does only weakly extend to the southern leg. With only one leg we cannot determine a 3-D wavevector for family 2 and source determination is not possible. A separation between family 2 and the upper GW packet is around 50 km. The upper GW packet is clearly defined between 51 km to 60 km. This GW packet closely resembles family 3 in the southern leg (left) and is categorised accordingly. The presence of three different families hints towards three different origins.

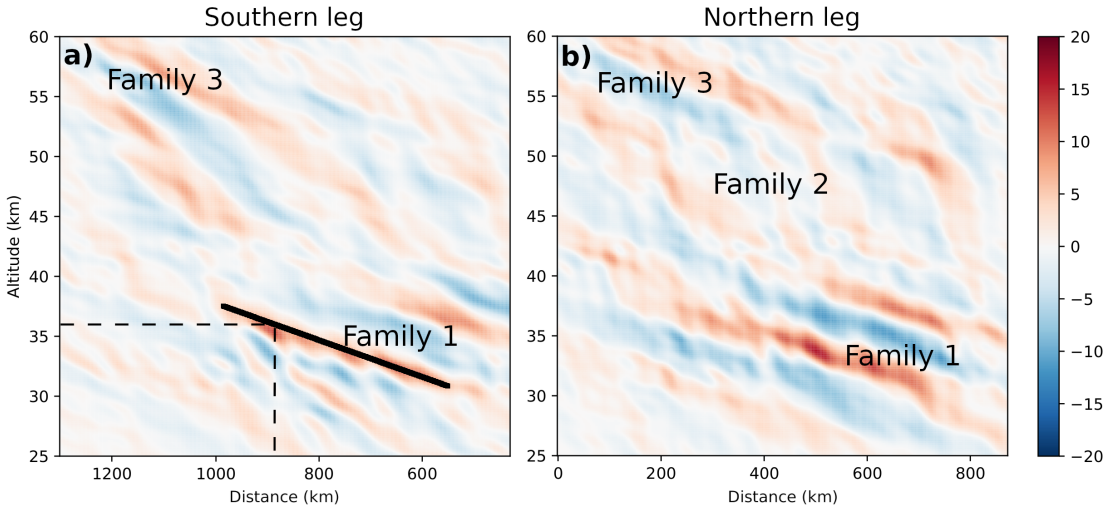

Figure 5.8: ALIMA temperature perturbations (in K) of the southern (a) and northern (b) leg. The x-axis is distance from the start of the respective flight leg. The eastern part of the southern leg is not shown here in order to have the same distance scale as the northern leg. Panels (a) and (b) show westward tilted GW phase fronts only (i.e. upward and westward propagating GWs, see Sect. 4.2.3). Note the three distinctly different wave packets, here named family 1, 2, and 3. The solid and dashed lines indicate the method of determining phase orientation on horizontal plots, see text for details.

5.3.1 ALIMA: GW Family 1

Family 1 is clearly distinguished between 32 km to 40 km on both legs (Fig. 5.8). From a single curtain we can obtain a vertical wavelength, but not an accurate horizontal wavelength and no

orientation. ALIMA provides high resolution 2-D observations above HALO, but by designing the experiment with the racetrack a 3-D picture is obtained. Combining the vertical curtain with the horizontal cuts (e.g. Fig. 5.9) 3-D information can be obtained. Phase fronts were approximated linearly in the vertical cut by drawing lines along the phase fronts (e.g. between 32 km and 38 km to identify the GWs — solid black line in Fig. 5.8a). Where the fitted line crossed a respective altitude the longitude was noted (dashed line Fig. 5.8a) and marked on the corresponding leg in the horizontal plot (Fig. 5.9). The phase orientation was obtained by connecting these longitudes, forming the phase fronts in Figs 5.9 and 5.10. By using this method we have a more complete picture. The racetrack flight pattern hence allows the determination of an accurate horizontal wavelength and orientation from ALIMA data exclusively.

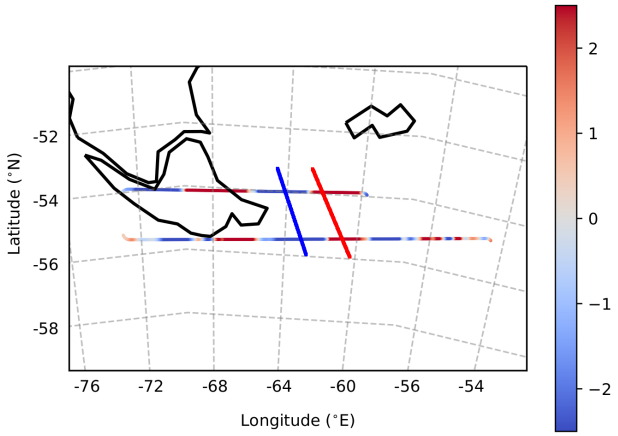

Figure 5.9: Temperature perturbation (in K) component showing the upward propagating GW as observed by ALIMA at 36 km. In an attempt to mask out short wavelength GWs, a colour scale is chosen where the temperature amplitude saturates at 2.5 K. Combining the northern and the southern legs and focusing on the long horizontal wavelength GWs, we can now form a 3-D picture. The drawn in phase fronts were determined with the help of vertical cuts. For the first time ALIMA data are used exclusively to determine GW phase orientation. From west to east we see two full wavelengths starting with a cold phase front.

Figure 5.9 is dominated by a long horizontal wavelength GW. For illustration one cold and warm phase front of the GW packet is drawn in. The blue and red phase fronts of both legs show a wavevector that points to the south-west (250° — measured on the drawn phase fronts). The horizontal wavelength is determined at about 473 km. Using ALIMA data that did not undergo the wavelet transform the amplitude is determined as 15 K. Horizontal cuts at multiple altitudes (seconded by the vertical cuts) show a vertical wavelength of 7.7 km. The ground-based phase speed

is calculated using the dispersion relation (Eq. 2.6) and reveal a nearly stationary GW, which is common for mountain waves. This means that we can safely assume horizontal stationarity over the two legs for family 1. The 3-D wavevector of family 1 was backtraced with GROGRAT to the Andes. The ray traced from 36 km to directly above the Andes main ridge at ≈52° S.

5.3.2 ALIMA: GW Family 3

Family 3 exists between 51 km and 60 km on Fig. 5.8. Figure 5.10 shows a clear westward slant of phase fronts with altitude between 53 km and 55.5 km. Figures 5.8 and 5.10 indicate a GW with a vertical wavelength of 7.5 km. Raw temperature residual data (before applying the 2-D Morlet continuous wavelet transform) show an amplitude of 7 K. The dashed phase fronts suggest an initial orientation of 282° and a horizontal wavelength of 291 km.

The dashed phase fronts on Fig. 5.10 form a curious Y-shape pattern with phase lines from the three fronts meeting around 58° S. The most likely explanation is that the GW is not stationary and the phase propagation is to the east. This would stretch the wavelength on the northern leg and shorten it on the southern leg similar to a Doppler shift effect between phase velocity and aircraft movement. The GW has a non-zero ground-based phase speed. This is corrected exemplary by using 53 km on Fig. 5.10. Combining the fact that this is an upward propagating GW (see Sect. 4.2.3) and the westward phase slant with height (Figs. 5.8 and 5.10) as well as the wind direction we know the GW wave vector points westwards. To calculate the ground-based phase speed in the x-direction we need wavenumber k (–1.87 × 10^{-5} m^{-1} is the average between the two legs), wavenumber m (8.3 × 10^{-4} m^{-1}), stability (N^2 =2.276e-4), scale height (7 683 m), and zonal wind (v =30 m s^{-1}). The calculated intrinsic phase speed in the x-direction is –16.96 m s^{-1}. The zonal wind speed is stronger than the intrinsic phase speed and the GW packet drifts eastwards at 13 m s^{-1} (and 13.1 m s^{-1} at 55.5 km). This means that when observing the warm phase front in the southern leg, the same phase front was located further westward than what it was observed in the northern leg in Fig. 5.10. The phase correction is calculated by:

$$\text{correction} = (t_{ref} - t_{obs}) \cdot C_{gb}, \tag{5.1}$$

where t_{ref} is the reference time of 05:30 and t_{obs} is the observation time. The solid lines between the flight tracks show the corrected phase lines. This correction reduces the Y-shape of the phase

fronts and provides a more natural looking GW packet.

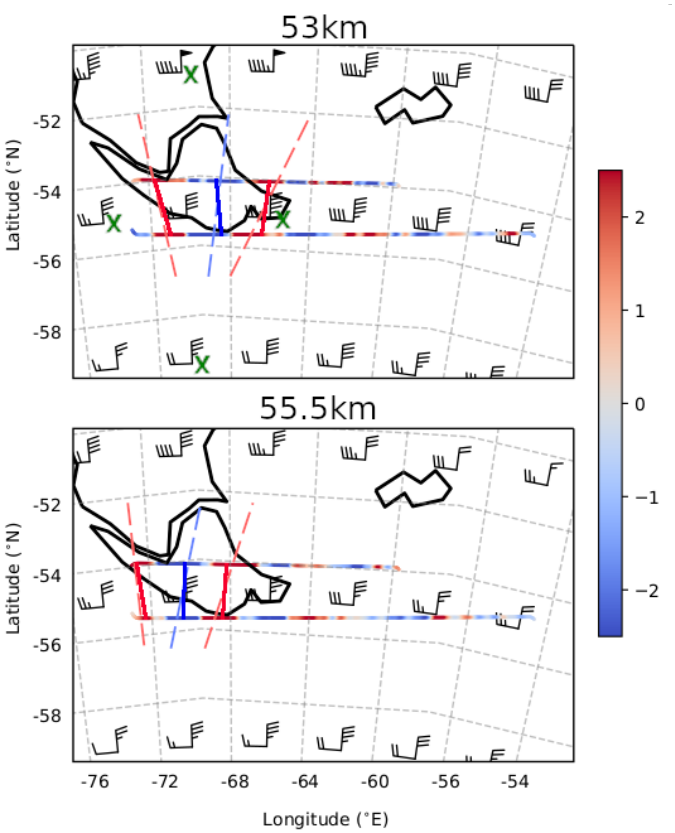

Figure 5.10: ALIMA temperature residuals (in K) showing upward propagating GWs at 53 km and 55.5 km. The background ERA5 zonal and meridional winds are shown in wind barbs. The barbs are similar to Fig. 5.2. Note the winds have a decreasing trend from northwest to southeast and with increasing altitude. The zonal wind speed is also generally weaker than the meridional wind speed. The dashed lines represent the phase fronts as determined from the vertical cut (Sect 5.3.1). The dashed phase fronts are then corrected to compensate for GW propagation (solid lines connecting the two racetracks — see Eq. 5.1 and corresponding text). The green X's on the top plot are used to predict the refraction in Sect. 5.4.

The new cold phase fronts (solid blue lines) suggest orientations of 262.8° at 53 km and 270.4° at 55.5 km. Raytracing this new and more accurate 3-D wavevector in GROGRAT shows the origin of this GW lies upwind of the Andes (Fig. 5.11) — another indication of a non-orographic GW source (the non-stationary GW phase speed being the first). Some weak evidence of a jet generated GW exists, however, conclusive evidence is missing. A peak in WKB values from 0.1 to 0.45 exists at 24 km — a value of 0.45 is not considered a WKB violation but its worth noting the peak. No increased values of the cross-stream Lagrangian Rossby number was found in the region. However, an increase in the cross-stream ageostrophic wind was detected at 24.4 km (refer to (Zülicke and Peters, 2006; Geldenhuys et al., 2021) for the calculation of these parameters). On

Fig. 5.11b the ERA5 data confirms the upwind GW. The GW signal is weak near the WKB peak. Also, between −2 000 to −2 200 km and directly above the ray path a weak fishbone (or V-shaped) structure is identified. That makes three weak signals that indicates a jet generated GW. This provides a curious case where a GW propagated for ≈1 500 km just to be observed over a mountain. This highlights the fact that a source can not simply be determined by pure co-location as already mentioned in Krisch et al. (2020); Geldenhuys et al. (2021); Strube et al. (2021).

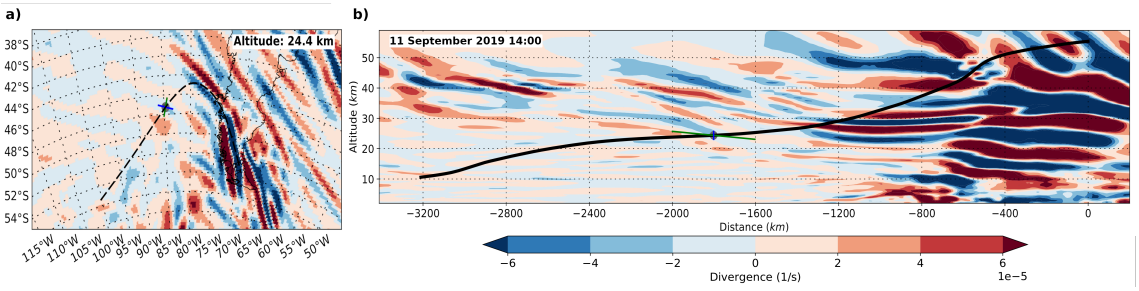

Figure 5.11: Divergence of ERA5 horizontal winds along the GROGRAT raytrace started at 55.5 km. Both plots are valid for 11 September 2019 at 14:00. Panel a shows the horizontal cut at 24.4 km. Panel b shows a vertical cut along the raypath. The black, blue and green line is similar to Fig. 5.6.

5.4 Refraction: Causality and Consequence

5.4.1 How do GWs refract?

This section will briefly explain how the GWs refract using the case of family 3. This section does not intend to provide an accurate or exact solution of refraction, but rather to describe its general behaviour. Horizontal wavelength and wave direction (which depends on the wavelength in the x- and y-direction) of a GW change in the presence of a horizontal wind gradient (Ehard et al., 2017). This is described by Eqs 2.15 and 2.16 from Lighthill (1978) (also in Marks and Eckermann (1995)). In the presence of strong horizontal wind gradients the first two terms in Eqs 2.15 and 2.16 are the dominant ones. We therefore neglect the smaller terms to obtain:

$$\frac{dk}{dt} = -k\frac{\partial u}{\partial x} - l\frac{\partial v}{\partial x} \tag{5.2}$$

and

$$\frac{dl}{dt} = -k\frac{\partial u}{\partial y} - l\frac{\partial v}{\partial y}. \tag{5.3}$$

Table 5.1: Parameters for input into Eqs 5.2 and 5.3 determined from Fig. 5.10. The distances in ∂x and ∂y are 535.1 km and 889.6 km respectively.

Altitude	∂u in x	∂v in x	∂u in y	∂v in y
53 km	$-10\,\mathrm{m\,s^{-1}}$	$-10\,\mathrm{m\,s^{-1}}$	$25\,\mathrm{m\,s^{-1}}$	$15\,\mathrm{m\,s^{-1}}$
55.5 km	$-5\,\mathrm{m\,s^{-1}}$	$-5\,\mathrm{m\,s^{-1}}$	$25\,\mathrm{m\,s^{-1}}$	$5\,\mathrm{m\,s^{-1}}$

Table 5.2: Calculated values to predict the new orientation using Eqs 5.2 and 5.3 with values stated in Table 5.1. Wavenumbers k and l are $-1.93 \times 10^{-5}\,\mathrm{m^{-1}}$ and $-2.44 \times 10^{-6}\,\mathrm{m^{-1}}$ at 53 km.

Altitude (km)	$^{dk}/_{dt}$ ($\mathrm{m^{-1}\,s^{-1}}$)	$^{dl}/_{dt}$ ($\mathrm{m^{-1}\,s^{-1}}$)	dk ($\mathrm{m^{-1}}$)	dl ($\mathrm{m^{-1}}$)	Predicted Orientation (°)
53	-4.06×10^{-7}	5.84×10^{-7}	-1.46×10^{-6}	2.1×10^{-6}	269.1
55.5	-2.03×10^{-7}	5.56×10^{-7}	-7.31×10^{-7}	2.0×10^{-6}	274.4

Family 3 experiences a significant amount of shear on the edge of the polar vortex and serves as a good example to understand refraction from both theory and observation. Refraction is evident in the solid phase lines between 53 km and 55.5 km on Fig. 5.10. The wind barbs on the plot represent ERA5 background zonal and meridional winds without the GW perturbation. The centre of the displaced and elongated vortex is located to the south (Fig. 5.3) and results in a decreasing wind speed from north-west to south-east (Fig. 5.10). This horizontal shear creates favourable conditions for refraction. Using the winds as input into Eqs 5.2 and 5.3 we can predict the refraction in time.

The wind gradient is determined in the x- and y-direction between the green X's on Fig. 5.10. The gradients in the x-direction are negative (Table 5.1) while being positive in the y-direction. Under normal non-displaced vortex conditions one would expect no gradient in the x-direction and a positive gradient in the y-direction. By placing these gradients together with the wavenumber k (calculated from new solid phase lines $-1.93 \times 10^{-5}\,\mathrm{m^{-1}}$) and l ($-2.44 \times 10^{-6}\,\mathrm{m^{-1}}$) into Eqs 5.2 and 5.3 we obtain $^{dk}/_{dt}$ and $^{dl}/_{dt}$ (documented in Tab. 5.2). Under the assumption that we see the same GW packet, dt can be estimated from the time it takes the GW to propagate from 53 km to 55.5 km, which is 1 hr[3]. According to the resultant dk and dl, the total horizontal GW wavelength from 53 km to 55.5 km will reduce from 323 km to 303 km. The predicted change in angle of orientation is from 262.8° at 53 km to 269.1° at 55.5 km. This compares remarkably well with the 270.4° we observe on Fig. 5.10 and the related discussion in Sect. 5.3.2. The GW is expected to refract by another 5° from 55.5 km to 60 km. After the phase correction applied in the previous section (see Fig. 5.10), the ALIMA observations can serve as an example for refraction.

From this section it is evident that refraction greatly depends on the wavelength and the wind

[3]The vertical phase speed varies between $0.5\,\mathrm{m\,s^{-1}}$ ($1.8\,\mathrm{km\,h^{-1}}$) to $0.75\,\mathrm{m\,s^{-1}}$ ($2.7\,\mathrm{km\,h^{-1}}$) for this GW. For convenience we assume it at $2.5\,\mathrm{km\,h^{-1}}$.

gradient. The wind shear experienced during this flight was anomalously strong for this time of the year. This was caused by the displaced vortex and sudden stratospheric warming (Sect. 5.1), which created a situation better than most to study refraction.

5.4.2 What is the impact of the refracting GWs?

In this section we show refraction impacts the atmosphere through taking up additional GWMF and by modifying the propagation path of the GW. Five GROGRAT experiments are conducted to illustrate this. All five experiments use the GW characteristics at the source of the GLORIA observed GW (obtained by backtracing — Sect. 5.2.3). The forward raytracing experiment starts directly above the source at 4 km. From Fig. 5.12 it is clear that mountain waves propagate a significant distance from the mountains. This figure place emphasis on the fact that source attribution due to co-location is not a good approach. The GW propagating into the Drake Passage is also a possible explanation for the missing GW drag at 60° S.

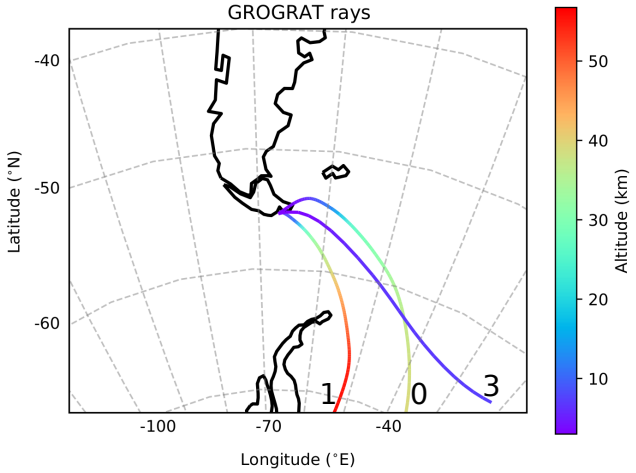

Figure 5.12: GROGRAT experiments during forward tracing of the GLORIA observed GW. Ray #0 shows raytracing using the 'normal' setup with 4-D propagation in a high-resolution background. Ray #1 uses the same 4-D propagation setup but uses a background u and v wind, which was multiplied by a factor of 1.5. Ray #2 is not depicted here as it will only show as a dot above the starting location. Ray #3 attempts to reproduce the results of (Hasha et al., 2008) and uses a coarse resolution background and only 3-D propagation setup.

The first experiment (ray #0) is the control experiment and is used to compare to different scenarios. Ray #0 represents the most up to date physics and should be the closest to reality. This entails the use of 4-D propagation setup and a high-resolution background as described in

Section 4.4. The GW represented by ray #0 in Fig. 5.12 rapidly propagates into the stratosphere in a south-eastward direction. Ray #1 uses the same setup but with an enhanced wind gradient in a stronger background flow. The enhanced gradient was obtained by multiplying the background wind with a factor of 1.5. Ray #2 represent the 1-D column parameterisation scheme employed by models. This ray can only propagate in the vertical and can not undergo refraction. Ray #3 is used to reproduce the experiment of Hasha et al. (2008). Hasha et al. (2008) used 3-D raytracing with low-resolution model background data. Input of GW characteristics were determined by a model parameterisation scheme. They concluded that there is no noteworthy reason to include refraction and horizontal propagation of mid-frequency GWs into models.

Richard Feynman said that proper experiment design requires you to first reproduce the results from previous work before you can build on that (Leighton and Feynman, 1985). With this in mind the experiment of Hasha et al. (2008) was reproduced as closely as possible, but keeping it comparable to the results in this study. To keep the results comparable the same (as ray #0 to #2) background conditions and ray initial conditions were used (which is a mid-frequency GW). Only the GROGRAT setup was changed to represent the 2008 experiment. Ray #3 on Fig. 5.12 was raytraced with the 3-D propagation setup (Sect. 4.4) in a coarse resolution background. Analogous to the Hasha et al. (2008) experiment the background consisted of a vertical (horizontal) resolution of 1.3 km (2.5°). The resulting forward raytrace of ray #3 follows the same horizontal trajectory as ray #0 at first but diverges towards the end of the ray. Ray #3 remains in the troposphere and at a much lower latitude than ray #0 (which ends at 75° S). Compared to the control ray (ray #0), the relative error in ray #3 is 10° of latitude and 35 km in altitude. The incorrect location of GWMF deposit by ray #3 will result in a noteworthy difference compared to ray #0. More importantly, the results from Hasha et al. (2008) are not reproduced as the GWMF deposit takes place at a significantly lower latitude. With the anomalously different wind regime of 2019, we can not come to the same conclusion as Hasha et al. (2008).

In another attempt (not shown here) to reproduce the results of Hasha et al. (2008) we used background conditions of a 'normal' year. In a new experiment we use the exact same propagation setup and resolution but using the non-stratospheric-warming year of 2018 as background input into GROGRAT. On 4 September 2018 at 06:00 a similar (to 11 September 2019) tropospheric synoptic system existed where a cold front brushed over the southern Andes with a ridging high pressure system behind that. We assume that this synoptic system will result in similar GWs to the GLORIA observed GWs. Raytracing the GW in the 2018 conditions we find after 25 h of

propagation the ray (again) remains in the troposphere, but only deviates by 2° of latitude from its source latitude. The small difference in latitude reflects a similar result to the conclusion of Hasha et al. (2008). Ignoring the incorrect altitude of the ray, we can say that the GW will produce drag at roughly the correct latitude. This experiment correctly reproduces the result of Hasha et al. (2008) — horizontal propagation and refraction can be ignored without serious repercussions. However, in different circumstances (like this case of 2019 with a weak and displaced vortex) this does not apply. The two experiments used to reproduce Hasha et al. (2008) confirms the finding of Durran (2009) who stated that the impact of refraction on GWMF is case dependent. Chen et al. (2005) and Durran (2009) found in their idealised numerical study that the GWMF is enhanced in regions of divergence and reduced in regions of convergence.

Ray #2 was restricted to vertical propagation and is not identifiable on Fig. 5.12 (as it is only a dot at the starting location below ray #3). Ray #2 attained a maximum altitude of 42 km (similar to our normal conditions represented by ray #0). The drag deposited from ray #2 will be at the correct altitude, but similar to ray #3 at the incorrect latitude — a major shortcoming.

Ray #1 uses background conditions with a stronger wind and an increased wind gradient. By multiplying the background wind with a factor of 1.5 we obtain a total wind speed more representative to normal (compared to the year 2020) stratospheric polar vortex wind speeds. The multiplication also results in a larger wind gradient. It is known that GWs prefer stronger winds to propagate in (if the wind is not too strong to create a propagation lid). Thus, it is no surprise to see ray #1 reach the highest altitude at 57 km. Ray #1 propagates further south and reaches polar vortex altitudes sooner compared to ray #0. The stronger wind with increased gradient creates an even more perfect setting (compared to ray #0) for GW propagation and refraction.

The GWMF of the 4 rays are compared in Fig. 5.13. Ray #1 dominates the graph and clearly the stronger wind / stronger wind gradient results in a higher GWMF. GROGRAT takes k, l and ground-based frequency as input and calculates the vertical wavelength from intrinsic phase speed. The intrinsic phase speed is affected by the higher background wind speed, which results in a larger vertical wavelength. This results in a higher GWMF value at the start of the ray. Ray #0, #1 and #2 agree somewhat with regards to the altitude where most of the drag is deposited. Ray #3 compares the worst as the ray never reaches the stratosphere. The comparison of the GWMF makes it clear that not only the deposition location differs (as described in the first part of this section), but also the amount of GWMF. Most of the community (and in fact all GW parameterisations) only consider GWMF decreasing with altitude. Ray #2 and #3 follow this as-

sumption, but ray #0 and #1 do not. To investigate this increase in GWMF we consider only ray #0 in Fig. 5.14.

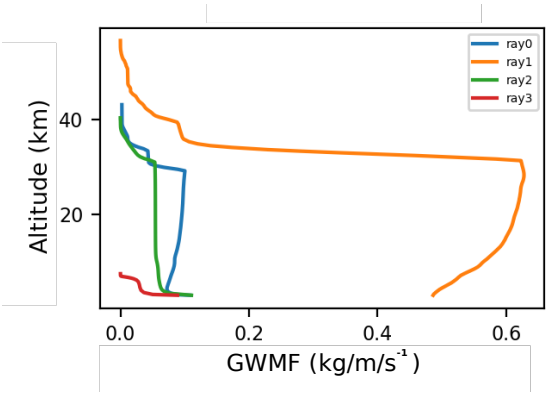

Figure 5.13: The GWMF along rays #0 to #3. Note the increase in the GWMF along ray #0 and #1, as opposed to ray #2 and #3, which only decrease with altitude.

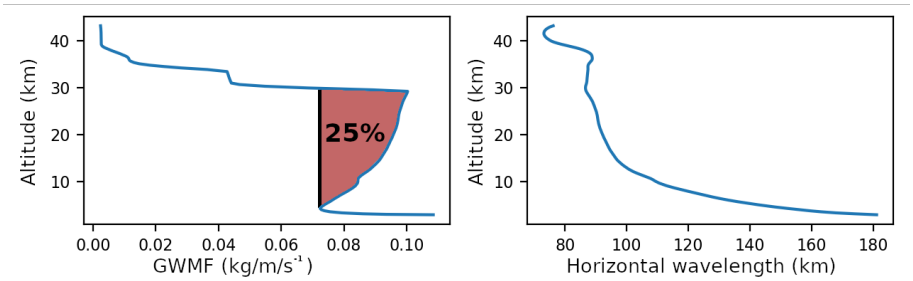

Figure 5.14: The GWMF and horizontal wavelength along ray #0. Note the maximum change in horizontal wavelength corresponds to the GWMF increase between 4 km and 30 km. An increase of 25.7% is observed.

The GWMF of ray #0 in Fig. 5.14 shows a clear increase between 4 km and 30 km. A strong decrease of horizontal wavelength corresponds with these altitudes. The changes in the wavelength during refraction can be interpreted as GW growth or GW dissipation (Fig. 2.1). The changing wavelength during refraction shows again that a GW is never fully stationary or unchanging, but constantly reacts and changes during its lifetime. In Section 5.4.1 we established that refraction is directly linked to the wavelength of the GW (and in turn the wavelength is linked to the wind gradient). Figure 5.14 confirms the link between GWMF and horizontal wavelength and therefore suggest a link to refraction. The GWMF equation for a single wave confirms this link (absolute momentum flux Eq. 1 from Ern et al. (2015)):

$$\mathrm{GWMF} = \frac{1}{2}\rho_0 \frac{\lambda_z}{\lambda_h}\left(\frac{g}{N}\right)^2\left(\frac{\hat{T}}{T}\right)^2, \tag{5.4}$$

where λ_z is vertical wavelength and λ_h is horizontal wavelength. The GWMF equation depends on the horizontal wavelength in the denominator. This means that if the horizontal wavelength decreases (Fig. 5.14 right) the GWMF increases (Fig. 5.14 left). Similarly, in an idealised numerical study Chen et al. (2005) found that the GW wavelength decreases if it propagates through wind divergent regions, increasing the GWMF of the GW. A GW packet consists of multiple single GWs superimposed on one-another. This means that the GWMF of the GW packet consists of a combination of the GWMF from all the single GWs. Thus, the GWMF of a GW packet have a similar dependence on the horizontal wavelength.

The change in wavelength (hence refraction) makes a significant contribution to the total GWMF of the GW packet. The GWMF along ray #0 increases by as much as 25.7% (scaled by the amount at forcing altitude). The additional GWMF is absorbed from the background flow. Accordingly, ray #0 can deposit a 1/4 more momentum and have a stronger effect on the background flow. The GWMF of ray #1 increases by 30% along the ray. This shows that a stronger wind with a larger wind gradient will increase the amount of missing drag in the model. In a numerical study for SouthTRAC flight 8, Alexander et al. (2022) found a general increase in the average GWMF with altitude calculated zonally in the rectangle defined by 45° S 63° W and 60° S 77° W. Similar to Fig. 5.14, they found a general increase with a peak in the GWMF at ≈30 km. This can be an indication that all the GWs in this region refract similarly with an increase in GWMF.

It is possible that the increase in GWMF averages out in time with all the other cases where GWMF decreases as a result of refraction (Durran, 2009). This can mean that this process does not have a meaningful impact over a longer time scale, however, this still needs to be confirmed. Even if the GWMF does average out over a time period, it can still have an important impact on global dynamics. Literature states that short but sustained bursts of GW activity can have marked impact on dynamics — for example Samtleben et al. (2020) found it can help to generate a sudden stratospheric warming. This would mean a few days with an increased amount of GWMF can have an important impact.

The five experiments (four rays plus the repeated Hasha-experiment) discussed in this section bring the importance of refraction (and horizontal propagation) forward. Not only do these processes affect where the GWMF is deposited, they also affect the amount of GWMF deposition.

5.5 Frequency of occurrence

The 2018 raytracing experiment (Sect. 5.4.2) indicated no increase in GWMF along the ray, whereas the 2019 experiment did. An important question is whether this increase in GWMF occurs regularly? Durran (2009) stated that if you sample waves at a regular time interval over a month, a few cases would be observed with an increase in GWMF with altitude. Three new experiments were designed to test this theory (Fig. 5.15). All rays used an ad hoc starting condition at 4 km with a horizontal wavelength, vertical wavelength and amplitude of 400 km, 4 km and 3 K respectively. The rays are traced forward in time and launched every day of the year at 00:00 from 1 June 2006 to 31 December 2006[4]. It is assumed that GROGRAT will filter out all the GWs that would not have formed due to unfavourable propagation conditions. It is noted that the change in GWMF in this experiment can also be a result of amplitude or other factors.

Panel (a) on Fig. 5.15 shows the first experiment, which was launched at the location of the backtraced GLORIA observed GW (Fig. 5.6). An orientation of 235° was used. It reflects the orientation of the tail of the Andes in the south of Patagonia. Figure 5.15 show only a few days throughout the time period with an increase in the GWMF with altitude. This means that for this single location an increase in GWMF occurs only a few times per year — in agreement with Durran (2009). The increase in GWMF will average out in time with all the other cases where GWMF decrease, as suggested by Durran (2009). However, Fig. 5.15 shows numerous short sustained bursts even for a single location (e.g. first week of November 2006). Literature states that such short but sustained bursts of GW activity can have marked impact on dynamics.

In a new raytrace experiment, two additional rays are used to represent more mountainous areas. Panel (b) of Fig. 5.15 represents three rays, each launched at a different position. The first ray was launched above the main Andes ridge, the second ray is the exact same location as for the first experiment (panel a) and the final ray was launched above the Antarctic Peninsula ridge. The orientation of the rays was chosen to reflect their underlying topography: 270° for the main Andes ridge and 325° for the Antarctic Peninsula. This experiment is very broadly used to represent the effect of mountain waves surrounding the Drake passage. One day on panel (b) is represented by only one of the three rays chosen by the maximum GWMF increase along the ray. Comparing panel (a) and (b) reveal a large increase in the number of cases with an increase in GWMF with altitude. Between September 2006 to December 2006 almost every second day shows an increase in GWMF.

[4] 2006 was used as this was the year with most satellite data available for inclusion into the reanalysis data.

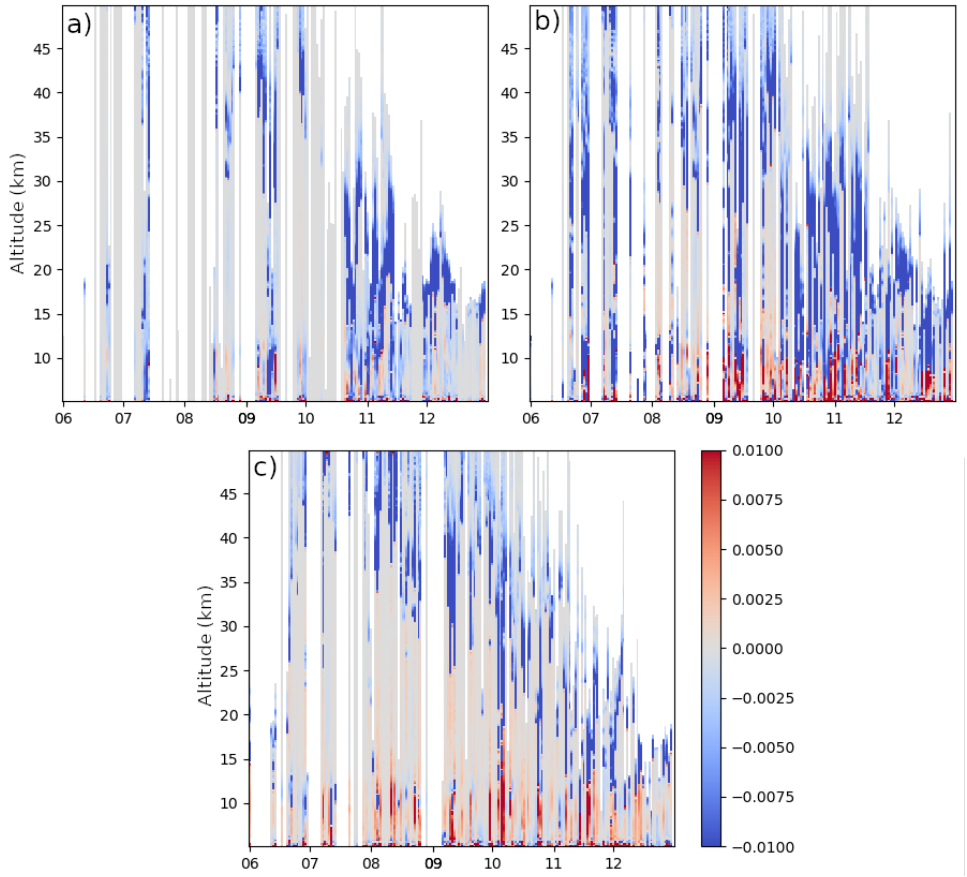

Figure 5.15: Three raytrace experiments showing GWMF (in $kgm^{-1}s^{-2}$) along rays for June to December 2006. Panel (a) represents a single location at the south tip of Patagonia — 54.52° S 65.31° W. Panel (b) show the maximum GWMF increase for three starting locations — 54.52° S 65.31° W, 52.15° S 74.86° W and 63.83° S 65.83° W. Panel (c) represent the maximum GWMF increase for 36 rays launched every 10° of longitude (starting at 5°) and at 54.52° S. Days without any profile (white space) represent days when GROGRAT determined the GWs can not propagate. Red demarcate and increase in GWMF and blue a decrease.

The final raytrace experiment tested the effect of GWs at different longitude positions. This experiment assumes non-orographic GWs are launched every day along the line of 54.52° S for every 10° of longitude. The experiment tests whether favourable synoptic conditions exist (to allow an increase in GWMF) elsewhere if not over the mountains of the Drake Passage. Similar to panel (b), panel (c) only shows the single ray (out of all 36 rays) with the maximum increase in GWMF. Figure 5.15c indicates that an increase in the GWMF takes place virtually every day of the year. This experiment likely assumes too many non-orographic GWs. However, it clearly indicates that throughout time some place on the globe has synoptic conditions that is favourable for an increase in GWMF. These three experiments confirm that the GWMF increase is not only a localised event,

but occurs globally and that models should account for this. Curiously the increase in GWMF seems to be restricted to below 15 km. Durran (2009) states that convergence/divergence is the result for the changes in wavelength and ultimately the changes in the GWMF, however, no literature dictates a fixed relationship. In a follow-up study it is intended to obtain a relationship between the GWMF increase and convergence/divergence[5].

5.6 Summary

This chapter provides the first observational evidence of GW refraction using high-resolution measurements from the troposphere to mesosphere. Refraction is observed from mountain waves and non-orographic GWs. GLORIA 1-D data shows refraction of 16° between 8 km and 12 km. Refraction of 9° is identified in the ALIMA data. The curtain retrievals of ALIMA form a 2-D dataset, but through creative flight planning a 3-D dataset is obtained. For the first time this allowed an accurate horizontal wavelength and orientation observation from lidar measurements — allowing a high-resolution refraction study.

Horizontal refraction, simply put, is the change in wavelength in x- and y-direction. Eqs 5.2 and 5.3 reveal that refraction depends on a wind gradient. Refraction affects the GW packet by increasing (in this case but can also result in a decreasing) the GWMF. A 25% increase in GWMF is found in this single GW case which was observed. In an artificial experiment,over a longer period of seven months, an increase in GWMF is seen only on a few cases. For a region like the Drake Passage an increase in GWMF is seen almost every second day at times. At a single latitude circle a GWMF increase is seen virtually every day. The effect of this increase in GWMF is not captured by a large part of the model physics and warrants further attention. This can make a sizeable contribution to the missing drag identified by McLandress et al. (2012) and Garcia et al. (2017). McLandress et al. (2012) state that “modelers should give serious thought” to account for meridional propagation of GWs in parameterisation schemes. This chapter shows that model parameterisation schemes should not only include horizontal propagation, but also refraction to improve representation of atmospheric dynamics.

[5]In the event that such a relationship can be determined a term can be added to the single column parameterisation scheme physics. However, it is expected that there will be a strong dependence on horizontal wavelength and this information does not exist in the parameterisation scheme.

Chapter 6

PGGS Campaign: Physics of a new GW source combination

Literature tells us that more GW observations are required (Plougonven et al., 2020) from more sources. Undiscovered GW sources can make an important contribution to the missing GW drag in the models. This chapter uses observations of GWs from which the source is unknown and aims to find the source — this is to add to the shortage of observations of GW sources.

This Chapter focuses om a HALO flight that took place on 10 March during the PGGS campaign. Two days before the flight was performed, high-resolution ECWMF medium-range weather forecasts predicted a large-scale GW event covering most of Greenland. Accordingly, a PGGS research flight was planned to measure these GWs, presumably generated by the breaking Rossby wave. However, at the time there were multiple suspected non-orographic GW source mechanisms. This chapter addresses Objective 3 (Chapter 1) and uses observations to identify the source of these GW. The chapter identifies a new non-orographic source mechanism which is linked to orography Geldenhuys (2018). Here I'd like to demonstrate how remarkably complex it is to identify the source of a modelled or observed GW by providing an in depth-analysis of a previously unobserved kind of gravity wave. It is believed to be the first documented observational evidence of a so far unconsidered mechanism.

6.0.1 PGGS — POLSTRACC, GWEX, GW-LCYCLE and SALSA

The PGGS campaign consisted of a single operation, which combined funding of multiple proposals, namely POLSTRACC[1], GWEX[2], GW-LCycle and SALSA[3] (DLR, 2022a). One of the major aims of the campaign was the investigation of the generation and lifecycle of GWs. The POLSTRACC campaign was aimed at investigating polar air during the polar vortex breakdown in spring. The PGGS campaign took place from December 2015 to March 2016.

Twenty-one research flights were conducted during all phases (DLR, 2022a). The campaign base was both in Oberpfaffenhofen, Germany and Kiruna, Sweden. The PGGS campaign consisted of 17 mission flights over 3 continents. Over 152 flight hours were dedicated in a region stretching from Tenerife (28.3° N) to the North Pole. One flight from this campaign is discussed in this chapter. HALO flew from Kiruna, Sweden to Greenland where it crossed the mainland from south-east to north-west at 10.5 km, and, on the way back at 13.5 km (blue line on Fig. 6.1). The flight took off on 10 March 2016 and measurements started at 15:18 UTC up to 22:26 UTC. Throughout this chapter, 18:00 UTC represents the time of the Greenland GW observation and the synoptic conditions of the flight.

6.1 Synoptic situation

The synoptic situation for the PGGS case study is shown by Fig. 6.1. The meandering 300 hPa geopotential height and horizontal wind fields show a cyclonically breaking Rossby wave. At flight time (10 March 2016 18:00 UTC, panel b), the potential vorticity lines steepen and turn back at the point of inflection, signalling Rossby wave breaking. An associated mid-tropospheric low-pressure system drifts from west to east (not shown). Accordingly, the sub-tropical jet drifts with time. However, the divergence of the winds within the jet remains above or in close vicinity of Greenland throughout the 30 h before observation. The above mentioned synoptic conditions are favourable for the formation of jet generated GWs (e.g. Uccellini and Koch, 1987; Plougonven and Zhang, 2014).

A trapping layer inhibits GW propagation beyond the respective layer. A trapping/reflection layer is formed by an increase in wind speed and stability and is identified with the help of the Scorer parameter (Eq. 2.9) (e.g. Durran, 2003; Geldenhuys et al., 2019). Knowing potential GW

[1] POLar STRAtosphere in a Changing Climate Oelhaf et al., 2019
[2] Gravity Wave EXperiment
[3] Seasonality of Air mass transport and origin in the Lowermost Stratosphere and the tropically controlled transition region using the HALO Aircraft

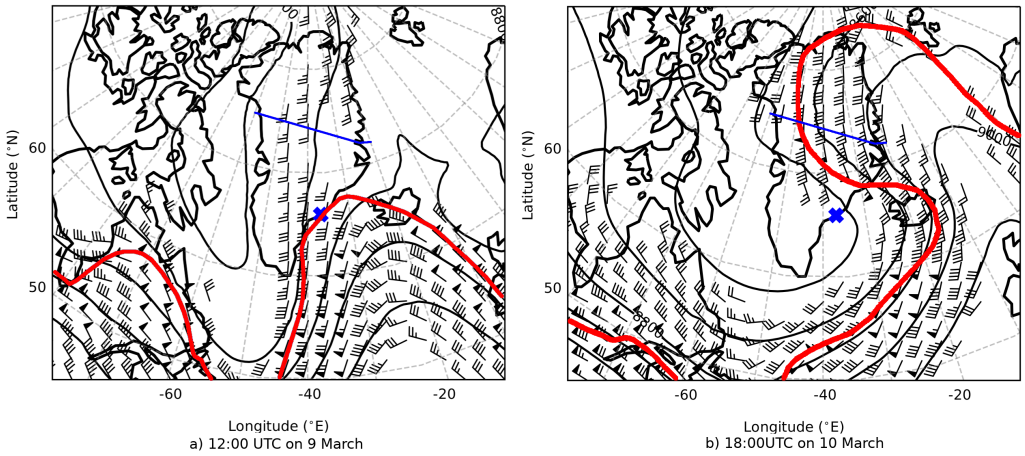

Figure 6.1: ERA5 geopotential heights and winds at 300 hPa valid for 9 March 2016 12:00 UTC (a) and 10 March 2016 18:00 UTC (b). Only wind speeds greater than 20 m s^{-1} are plotted. A triangle represents 50 m s^{-1}, one full line represents 10 m s^{-1} and half a line 5 m s^{-1}. The red line represents the approximate (excluding eddies and local fluctuations) 4 PVU line. The blue cross will be referred to in Sect. 6.3. The blue solid line represents the flight section used for GLORIA retrieval.

reflection layers can therefore be important to find the sources of GWs. The Scorer parameter reveals that up to 30 h before observation all horizontal wavelengths $>$ 4 km will propagate through the reflecting layers. With no reflecting layers present for the wavelengths considered in this study, it is clear the GW source can be located at the surface, or in the free troposphere. Furthermore, this justifies the use of ray-tracing tools for freely propagating GWs (Sect. 6.3).

A jet is known to release upward (above the jet) and downward (below the jet) propagating GWs (Thomas et al., 1999; Guest et al., 2000). Hodographs can be used to distinguish between upward and downward propagating GWs. In the Northern Hemisphere clockwise (anti-clockwise) rotating hodographs indicate upward (downward) propagating GWs (Andrews et al., 1987; Hertzog et al., 2001). Multiple hodographs from ERA5 reanalysis were drawn within the 500 and 300 hPa jet region. The hodographs (e.g. Fig. 6.2) depicted no rotation to weak clockwise rotation with altitude below 7 km, with strong clockwise rotation above 10 km. The rotation above 10 km is nearly circular, which implies that $f/\omega \approx 1$. This points to an upward propagating inertia-gravity wave with a low intrinsic frequency close to the Coriolis parameter (Hertzog et al., 2001; Fritts and Alexander, 2003). Less pronounced is nearly a full anticlockwise rotation between 7 and 10 km, even though this altitude range should be treated with care as the jet region (7.5to 10 km at flight time) can influence the hodograph.

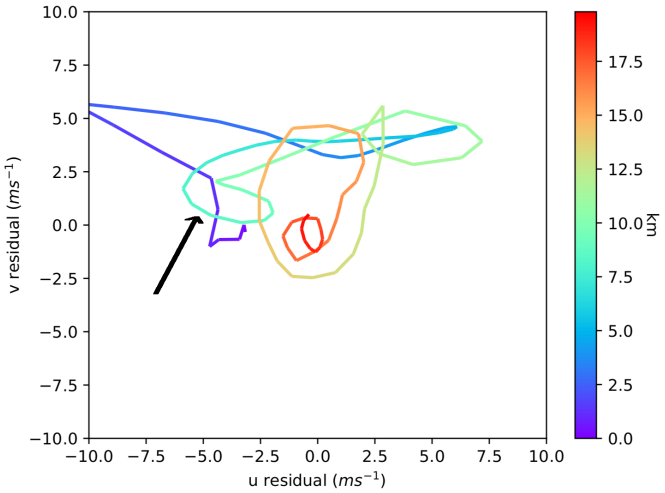

Figure 6.2: Hodograph in the centre of the jet upwind of Greenland at 60° N and -30° E. The arrow points to the anti-clockwise rotation between 7 and 10 km, with the rest being clockwise or no rotation. The hodograph is valid for 9 March 2016 at 07:00 UTC, calculated from ERA5, and a good representative for all hodographs upwind, within the jet and through time.

6.1.1 Calculation of geostrophic balance

In this section, the cross-stream ageostrophic wind (Eq. 2.13) is used to diagnose unbalanced flow within the jet as suggested by Mirzaei et al. (2014). To calculate this, firstly, horizontal wind (u and v components) and geopotential height fields were smoothed to remove GW signatures with a boxcar[4] over 500 km in x and y direction (similar to Mirzaei et al. (2014)). Secondly, ageostrophic winds (u_a and v_a) were calculated on pressure level data, using MetPy (May et al., 2008 - 2020). Thirdly, the cross-stream ageostrophic wind was calculated using the approach of Zülicke and Peters (2006) and Eq. 2.13. In a final step it was tested whether this quantity exceeds the threshold of 7.5 m s^{-1}, which corresponds to a critical Rossby number of 0.15 and a length scale of 500 km. A conservative value of 7.5 m s^{-1} is used to indicate that the jet exit region is out of balance and can spontaneously emit GWs. Mirzaei et al. (2014) used 1 m s^{-1} to indicate out of balance areas in the jet, and argued theoretically 4 m s^{-1} is a good value. Hence, a value of 7.5 m s^{-1} is a conservative value.

[4]Zülicke and Peters (2006) smoothed over 1 000 km, but for this case smoothing over 500 km better conserved the synoptic wind structure and was sufficient to remove all GWs.

6.2 GLORIA observations

The GLORIA temperature field is retrieved from the higher flight leg over Greenland (black line in Fig. 6.3). The results acquired from measurements taken from this leg represent the situation from 19:00 UTC to 21:00 UTC. Gravity waves are seen within the tangent point area in Fig. 6.3. Outside this volume the retrieval does not have measurement information and falls back to the a priori. The GWs within the tangent point area compare well to ERA5 data (more on this in Sect. 6.3). In the horizontal (panel a), the GW phase fronts are oriented at about a 90° angle to the flight path. With height (panel b), the phase fronts slant eastwards. Slanting GW phase fronts are an indication of vertically propagating, internal GWs. The observed slant together with the hodograph analysis indicate upward propagation, with intrinsic propagation to the east.

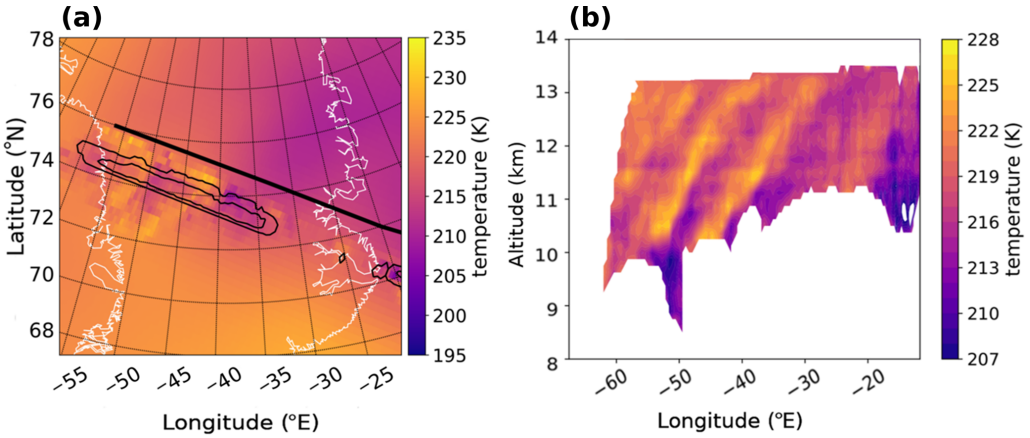

Figure 6.3: Horizontal (a) and vertical (b) cross-section of the GLORIA temperature retrieval, showing the retrieved GW packet. Outside the retrieval volume the field is determined by the a priori. The horizontal cross-section is shown for 11 km. The white line represents the Greenland coastline. The thick black line represents the section of the flight path that was used for the retrieval, the thin black contours represent the tangent point area. The vertical cross-section is averaged at 90° to the flight path using only data within the tangent point area. Note the decrease in vertical wavelength and amplitude above 12 km.

The GW characteristics are determined within the tangent point volume indicated in Fig. 6.3 and similar retrieved images. The characteristics of these GWs are listed in Table 6.1 and were used as input to GROGRAT simulations (see next section). A horizontal wavelength between 320 km and 390 km is observed in different parts of the GW packet. The vertical wavelength is between 1.6 and 2.1 km, and the GW orientation between 130° and 140° from North. The amplitude and vertical wavelength decrease with altitude (as can be seen in Fig. 6.3b). This is indicative that a change in propagation conditions is taking place and point to GW dissipation (more on this in Sect. 6.3).

Table 6.1: Gravity wave characteristics determined by eye from the retrieval (Fig. 6.3). The wavelengths are represented by λ_h and λ_z for the horizontal and vertical direction respectively. Ray #0 to #3 were used as input for the GROGRAT raytracer.

GW number	Lat (° N)/ Lon (° E)	Alt (km)	λ_h (km)	λ_z (km)	Ground-based frequency (s^{-1})	Temp amplitude (K)
0	74.3/-38.8	12.3	386.2	1.6	9.6e-5	3
1	73.9/-41.5	12.0	320	2.0	1.2e-4	4.5
2	74.5/-43.3	11.4	335.8	2.0	1.3e-4	4.5
3	74.0/-45.0	11.0	330.1	2.1	1.6e-4	4.5

6.3 GROGRAT raytracing

Tracing the backward trajectory of a GW is an established method to find its source (e.g. Marks and Eckermann, 1995; Krisch et al., 2017, 2020). According to Hertzog et al. (2001), the excitation of GWs by geostrophic adjustment from the jet is usually associated with enhanced values of the WKB parameter (δ) near the height of the wind maximum. This is attributed to the sharp upper and lower edges of the jet. Sharp changes in the jet wind speed will induce sharp changes in the vertical wavenumber. If the scales of change in the wavenumber becomes large compared to the wavelength, the WKB parameter is violated (see Eq. 4.4 and corresponding Sect. 4.4).

Four main rays were backtraced, starting between 11 and 12.3 km based on the GW parameters given in Tab. 6.1. The GW ground-based frequency or input to GROGRAT was calculated via the dispersion relation (Eq. 2.6) using the horizontal- and vertical wavelength in Table 6.1 as well as ERA5 reanalysis data.

All rays trace backward into the jet and end over the ocean, with exception of ray #3 (Fig. 6.4 — rays named as in Tab. 6.1). As the vertical cross-section of the GLORIA observation indicates the GW is propagating intrinsically opposite to the wind. The horizontal group velocity, however, is slower than the wind velocity which leads to a downstream drift of the GW packet. To provide further confidence in the raytracing study, sensitivity tests were performed. An ensemble raytrace (20 members) was conducted by perturbing the initial conditions (listed in Tab. 6.1) by $\approx$10%. This means $\pm$0.2 km for the vertical wavelength and $\pm$30 km for the horizontal wavelength. This is the approximate error associated with the wavelength determination from Fig. 6.3. All ensemble members behaved similarly to the main rays (Fig. 6.4). The ray paths proved to be more sensitive to the launch orientation. A 10° change in orientation frequently ended with the backtraced GW being evanescent or vertically stalling. In another experiment, the 4 main rays were backtraced,

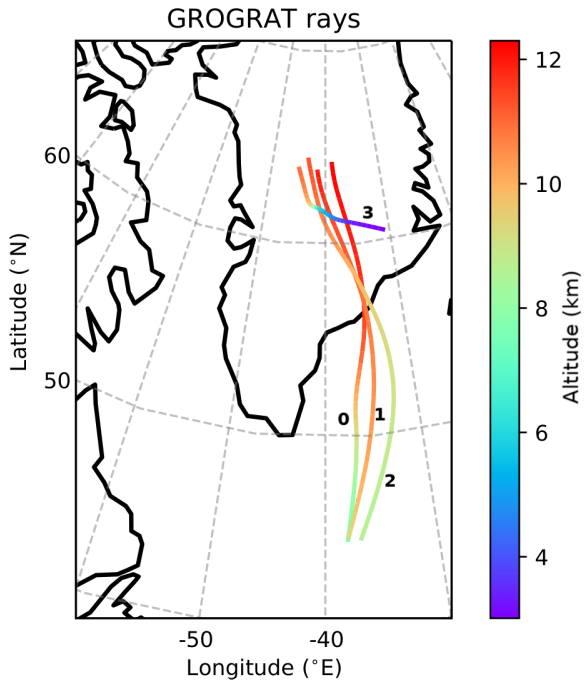

Figure 6.4: GROGRAT backtracing rays, using a 4-D setup. The rays have a starting time of 10 March 2016 at 18:00 UTC. The initial conditions to the rays are listed in Table 6.1. The backtracing starts between 11 and 12.3 km and is depicted respective to their altitude, latitude and longitude.

whereby the ray orientation at the end of the ray was perturbed (again by 10°) and forward traced. In the forward tracing, a change in orientation was much less sensitive. This shows that the excited GW spectrum expands from the source and organises itself by the propagation conditions to GW packets of similar characteristics and spread over a large area. A similar behaviour (known as frequency-dispersion) is known for ocean waves (Holthuijsen, 2007).

Ray #0 to #2 (named as in Tab. 6.1) all experienced large horizontal propagation and very little vertical propagation. This is normally characteristic of trapped GWs, however, the slanted phase fronts in Fig. 6.3 indicates the GWs were not trapped. Figure 6.4 highlights the importance of including meridional propagation in model GW physics. Only ray #2 is discussed here in detail (Fig. 6.5). The GROGRAT-calculated vertical group velocity peaks at 10 km with 0.2 m s^{-1} and has a minimum of 0.05 m s^{-1} at 9 and 11 km (Fig. 6.7). This translates to a vertical propagation speed of 180 to 720 m h^{-1}. Intrinsic horizontal group velocity peaks at 72 m s^{-1} and has a minimum of 26 m s^{-1}. This translates to a ground-based group velocity ranging from 6 m s^{-1} to 17 m s^{-1}. The wavelengths and phase orientation predicted by GROGRAT correlates well with the ERA5 reanalysis and produces further trust in the experiment (same as for ray #3 - Fig. 6.6).

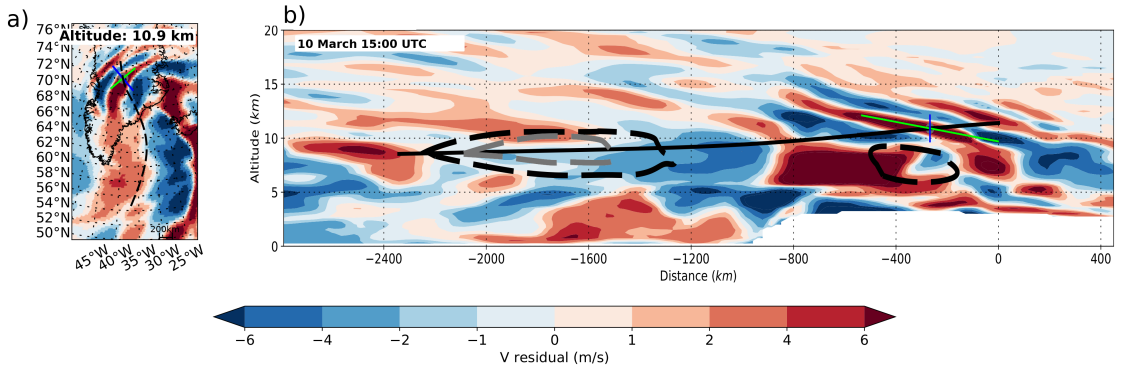

Figure 6.5: GROGRAT backtracing of ray #2 and meridional wind (v) residuals from ERA5. The backtracing starts at 11.4 km (on 10 March 2016 at 18:00 UTC) and ends at 8.5 km (on 9 March 2016 at 18:00 UTC). Panel a shows the horizontal cross-section of the ray path (dashed black line) and the corresponding v residual wind speeds at 10.9 km. Panel b shows the vertical cross-section of v residual wind speeds along the ray path (solid black line). Raytracing started at ray reference time 42 h (flight time), both a and b are valid for 13:00 UTC (5 h prior to ray initialisation). The cross of the blue and green line represent the position of the GW at the respective time, the blue line indicates one horizontal (vertical) wavelength in the horizontal (vertical) cross-section and the green line indicates the orientation of the phase fronts, all calculated in GROGRAT. The thick dashed black (grey) line indicates cross-stream ageostrophic wind values in excess of 7.5 m s^{-1} (10 m s^{-1}). The encircled dashed area at −1 500 km occurred between 24–19 h before ray initialisation (the backtrace passed through this area at the same time). The encircled dashed area at −400 km represents an out of balance jet at 2–7 h before ray initialisation.

The cross-stream ageostrophic wind indicates out of geostrophic balance flow within the jet exit region at multiple locations along the ray path (Fig. 6.5). On Fig. 6.5 at x=−1 500 km the ray passes through a 10 m s^{-1} cross-stream ageostrophic wind region 22 h before observation. Multiple other out of balance regions exist within the jet throughout the ray lifetime. From this, it is concluded that the jet is constantly emitting GWs. It is noted that ray #0 to #2 did not have major WKB violations. Although WKB values reached a maximum within the out of geostrophic balanced jet regions, the peak values reached mere values of 0.5.

Ray #3 is the only GW which traces to the orography (Fig. 6.6) and hence was investigated for a possible mountain wave. The ray traces to the plateau of Greenland, and not the precipitous coastline orography. In addition, the ray passes through a cross-stream ageostrophic wind region at the steepest part of the ray. Clear violations are observed in the WKB values at 6.5 and 8 km (consistent with the findings of Hertzog et al. (2001)), supporting the idea that the GW is released by the jet. It should be noted that cross-sections through ERA5 reanalysis residual data did indicate mountain wave activity localised in time and space along the coast. However, as far as the GROGRAT experiment is concerned, these mountain waves were not observed by GLORIA. Ray #3 was emitted by the jet initially with a longer vertical wavelength (hence the steep propagation path at x= −250 km), which was immediately reduced as it propagated out of the

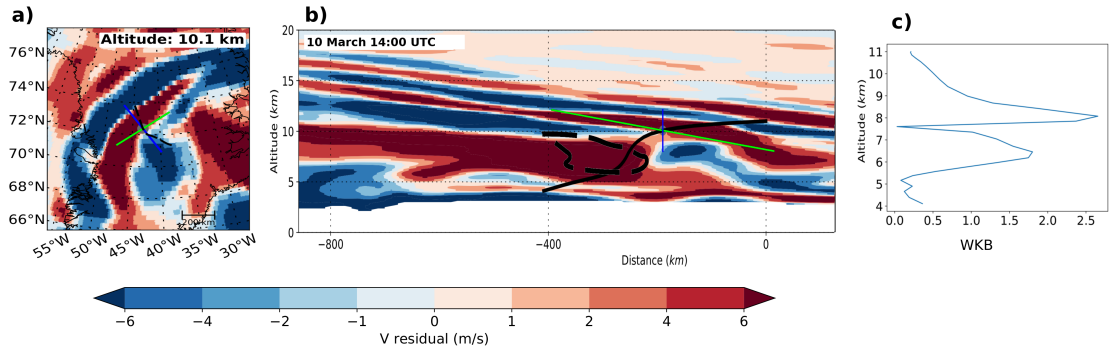

Figure 6.6: Similar (a and b) as in Fig. 6.5, but valid for ray #3 on 10 March 2016 at 14:00 UTC (4 h prior to ray initialisation). The horizontal cross-section (panel a) is valid for 10.1 km. Panel b shows the raytracing starts at 11 km and ends above the Greenland plateau. The thick dashed black line indicates cross-stream ageostrophic wind values in excess of 7.5 m s^{-1}. Panel c indicates the WKB parameter with height. The relation of the WKB parameter can be related to the jet in Fig. 6.8.

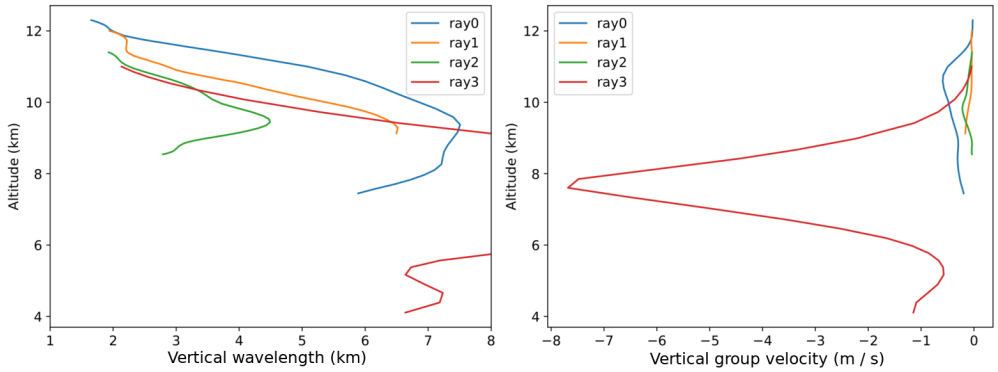

Figure 6.7: Vertical wavelength (left) and vertical group velocity (right) along the backtrace for ray #0 to #3 as calculated by GROGRAT. The leftmost plot is cut at 8 km in order to achieve readability for ray #0 to #2.

strong wind regime. The vertical group velocity peaked around 8 m s^{-1} (Fig. 6.7), receding rapidly to 0.04 m s^{-1} at 11 km.

The vertical wavelength of rays 0 to 2 similarly decreased above the jet region (Fig. 6.7 left). The effect of the changing vertical wavelength is also observed on the vertical group velocity (Fig. 6.7 right). Similarly the observed GW amplitude and the observed vertical wavelength decrease with height (Fig. 6.3 and Tab. 6.1), this can imply that the GWs are dissipating. A large drop in background wind speeds (17 m s^{-1} for ray #3 and 40 m s^{-1} for ray #0 to #2) occur from 8 to 9 km to the ray starting altitude (Fig. 6.8). Within the same region the stability ($\frac{\partial T}{\partial z}$) of the atmosphere changes dramatically within the jet exit region (location indicated by the blue cross on Fig. 6.1).

The maximum stable temperature amplitude determined by Eq. 2.20 is 0.9 K. Thus it can be said that the temperature amplitude (Tab. 6.1) is unstable and GW breaking will occur. Similarly, the Richardson number along the rays occasionally peaked to critical values. The strong decrease in wind speed created the critical layer and is responsible for the decrease in the vertical wavelength, and hence responsible for the GW dissipation. As the wind speed approaches the horizontal phase velocity (Fig. 6.8), the intrinsic frequency decreases to zero, which means the vertical wavenumber will approach infinity — representing a critical layer for the GW.

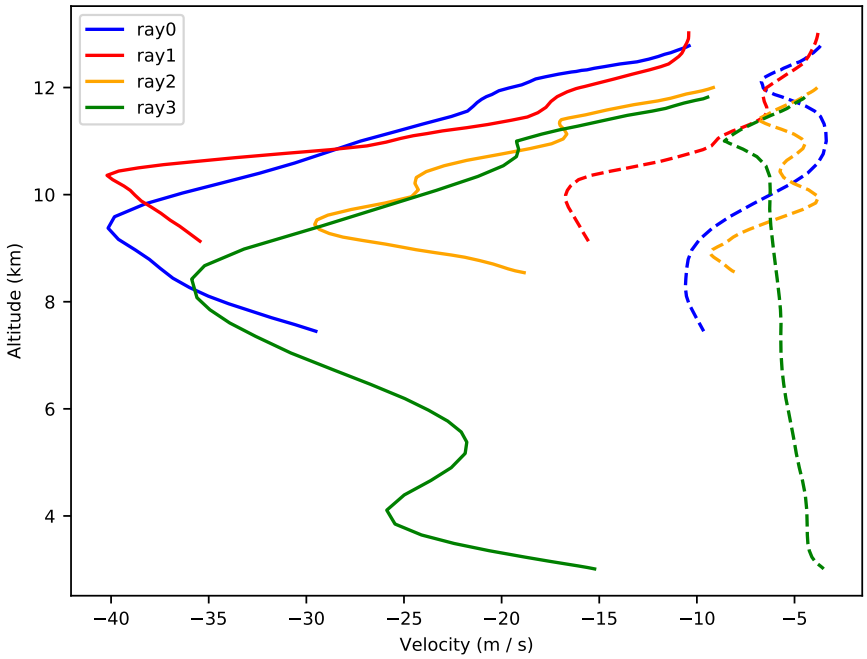

Figure 6.8: The horizontal phase velocity (dashed) and the background wind (solid) along rays #0 to #3. Where the phase velocity and the wind speed approach one another a critical layer exists. Altitudes above the ray starting point (Tab. 6.1) represents the same starting conditions raytraced forward.

6.4 Numerical Weather Prediction Experiment and GW source identification

Originally designed as an attempt to entirely rule out topography as a source, a numerical experiment with strongly reduced topography was designed. This yielded unexpected results implicating topography as a major contributor.

6.4.1 Numerical experiment overview and results

The unmodified ECMWF operational model was used as the control run (CTL-run Sect. 4.3.2) (Fig. 6.9a-h). The CTL-run produced GWs (Fig. 6.9e) similar to observations (Fig. 6.3) and ERA5 data (Figs. 6.5 and 6.6).

The second experiment (T21-run) uses a T21 topographic field (the lowest resolution topographical field available), to achieve a smoothed orography. Comparing the CTL-run with the T21-run on 10 March 2016 at 18:00 UTC (Fig. 6.9e and m), in the area of interest GWs are observed in the CTL-run, but hardly any are seen in the T21-run — also in the following time steps. The very weak GWs observed in the T21-run exist from the very first model time step, and no new GWs are excited in the following time steps. Clearly, the topography plays a significant role in GW generation. Are the two experiments hence an indication of direct orographic GW generation? Keeping in mind that Sect. 6.3 implicated the jet as the likely source, this hint to orography is a puzzling result. Therefore the hypothesis that the orography is responsible for the GW excitation in an indirect way is investigated.

6.4.2 CTL-run vs. T21-run: What is the difference?

Which synoptic scale differences can arise from the reduced orography that could induce GW excitation? As argued in Sect. 6.3 the GWs are likely excited by out of geostrophic balanced flow. Therefore, the cross-stream ageostrophic wind (calculated as in Sect. 6.1.1) for the two model runs are compared. In Fig. 6.9, the cross-stream ageostrophic wind is shown where all three of the following conditions are met: the values of the cross-stream wind are greater than $7.5\,\mathrm{m\,s^{-1}}$, the total wind speed is greater than $20\,\mathrm{m\,s^{-1}}$, and latitudes are lower than 80° N. As mentioned in Sect. 6.1.1, a critical value of $7.5\,\mathrm{m\,s^{-1}}$ is used to indicate when the jet can spontaneously radiate GWs.

The CTL-run, in Fig. 6.9, has large cross-stream ageostrophic wind regions. These cross-stream ageostrophic wind regions are an indication of an imbalance between the Coriolis and the pressure gradient force in the jet. Early after model initialisation (12 and 18 h — Fig. 6.9a and b, the CTL-run indicates large out of balance jet regions over the ocean. Figure 6.9b depicts the CTL-run jet reaching cross-stream ageostrophic winds of $10\,\mathrm{m\,s^{-1}}$). Six hours later the CTL-run jet is unbalanced over the Greenland mainland (Fig. 6.9c). The greater the cross-stream ageostrophic wind is, the more unbalanced is the jet, and the more likely it spontaneously emits GWs (Zülicke and Peters, 2006; Mirzaei et al., 2014).

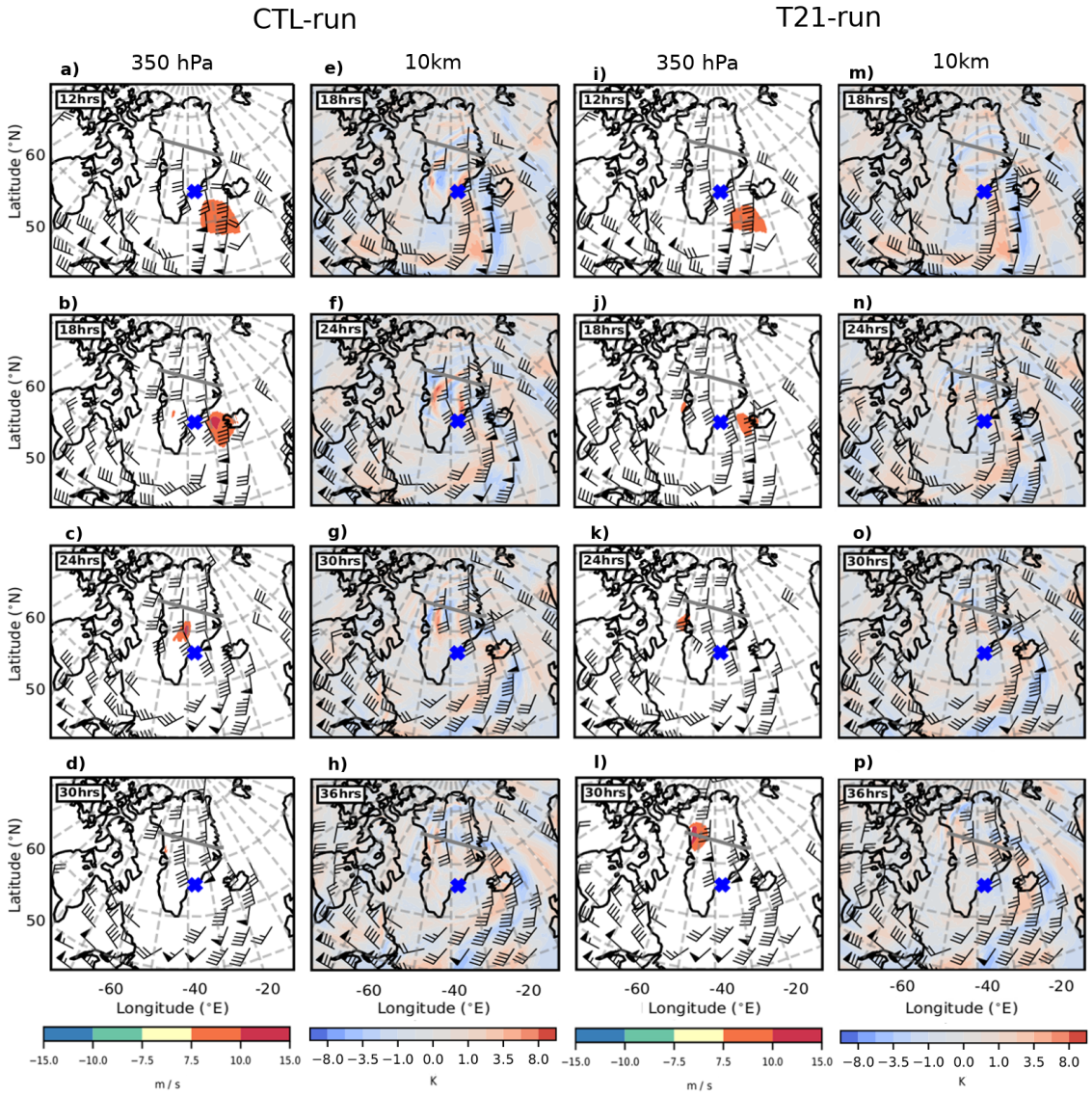

Figure 6.9: CTL-run (a–h) and T21-run (i–p) cross-stream ageostrophic wind and temperature residuals at different times. The cross-stream ageostrophic wind (a–d and i–l) was calculated on pressure levels, hence here it is depicted at 350 hPa (≈8.1 km). The temperature residuals (e–h and m–p) were determined on geopotential heights, hence this is valid for 10 km. The temperature residuals are depicted ≈2 km higher than the cross-stream ageostrophic wind, as the GW structure forms a complex interference pattern with upward and downward propagating GWs within the jet. The temperature residual plots are offset by 6 h from the cross-stream ageostrophic wind to allow time for the GWs to propagate to 10 km (a vertical group velocity of 200–700 m h^{-1} indicates vertical propagation of 2 km between 3 to 10 h). The overlaid wind barbs are as in Fig. 6.1. The flight path is indicated in grey and thick black lines are the coastline. The blue cross acts as a centre point of reference in the jet and indicates the location of the stability discussion in Sect. 6.3. Times (in h) are since model initialisation (on 9 March 2016 at 12:00 UTC) + xx h ("xx" as specified in top left corner of each plot).

After each imbalance in the jet a GW response is seen 6 h later 2 km higher and downwind of the imbalance region (comparing Fig. 6.9a to c with e to g). This height and area offset is understandable as the GWs take time to propagate from 8 to 10 km meanwhile drifting horizontally. Taking the mid-range ($\frac{\text{min}+\text{max}}{2}$) vertical group velocity of ray #0 (Sect. 6.3), the GW packet will propagate 2.7 km vertically in 6 h. Throughout all shown time steps the unbalanced region is associated with a GW field downwind.

The T21-run (Fig. 6.9i to p) shows a totally different picture. Firstly, the cross-stream ageostrophic wind indicates a smaller region and a more balanced jet. Small regions of 7.5 m s^{-1} (no 10 m s^{-1} region) is seen over the ocean in Fig. 6.9i and j. No cross-stream ageostrophic wind is observed upstream or over the Greenland mainland at 24 h after model initialisation (Fig. 6.9k). Matching the more balanced jet, GWs are almost nonexistent in the T21-run.

Only during one time step was the T21-run jet more unbalanced than the CTL-run (Fig. 6.9d and l). At forecast hour 30 (at flight time) a large area of imbalance occurs below the north-westernmost part of the flight track (Fig. 6.9l). This imbalance area (at 350 hPa) is larger in the T21-run and indicated cross-stream ageostrophic wind values exceeding 10 m s^{-1}. Six hours later, the T21-run indicated more GWs than the previous time step (north of the flight track — Fig. 6.9p), and for the first time, a comparable (if not a greater) GW field to the CTL-run (Fig. 6.9h) was observed.

The CTL-run, in Fig. 6.9, has larger and more intense cross-stream ageostrophic wind regions when compared to the T21-run. Throughout all shown time steps the greater unbalanced region is rewarded with a greater GW field. Therefore, it is asserted that the GWs are directly caused by the increased out of balance within the jet.

In order to find direct evidence for the presence of GWs upstream of Greenland, divergence is considered. Divergence fields are a frequently used method to discern between GWs and balanced motions (Zülicke and Peters, 2006). Beside the emphasises of the shorter scales by differentiation, this method removes the geostrophic modes and leaves the ageostrophic flow including GWs. This is applied to the potential source region of the GWs upstream of Greenland for Fig. 6.10. Six hours after model initialisation (left) a superposition of wave phase fronts parallel to the isobars and perpendicular to the flow between the blue cross and Iceland is seen. The latter is likely to become the waves observed later with GLORIA. At 18 hours (right) the two directions of phase fronts have separated, forming long streaks parallel to -30° E south west of Iceland and an arc of phase fronts perpendicular to the flow between Iceland and Greenland. These GWs

upstream of the Greenland coast are consistent with our hypothesis that flow instability upstream of the terrain is the source of the GW patterns. Furthermore, the source moves with the jet and drifts over Greenland in later time steps.

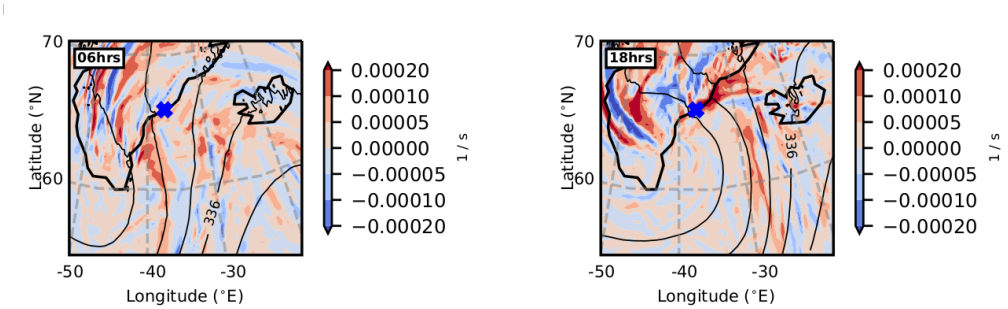

Figure 6.10: Divergence for CTL-run at 6 and 18 hours after model initialisation. The divergence is indicated at 8.2 km to correspond to the cross-stream ageostrophic wind at 350 hPa in Fig. 6.9. The overlaid pressure isolines (thin black lines) give an indication to the geostrophic wind direction. The blue cross is used as a point of reference, while the thick black lines and times in the top left corner are as in Fig. 6.9.

6.4.3 CTL-run vs. T21-run: What causes the difference?

If the CTL-run has GWs, and the T21-run does not, then the difference between the two model runs must be the source of the GWs. By now it has been established that the jet and its related imbalance is the cause of the GWs. It is clear that the orography played a role in the balance of the jet, but there is a missing puzzle piece connecting these two.

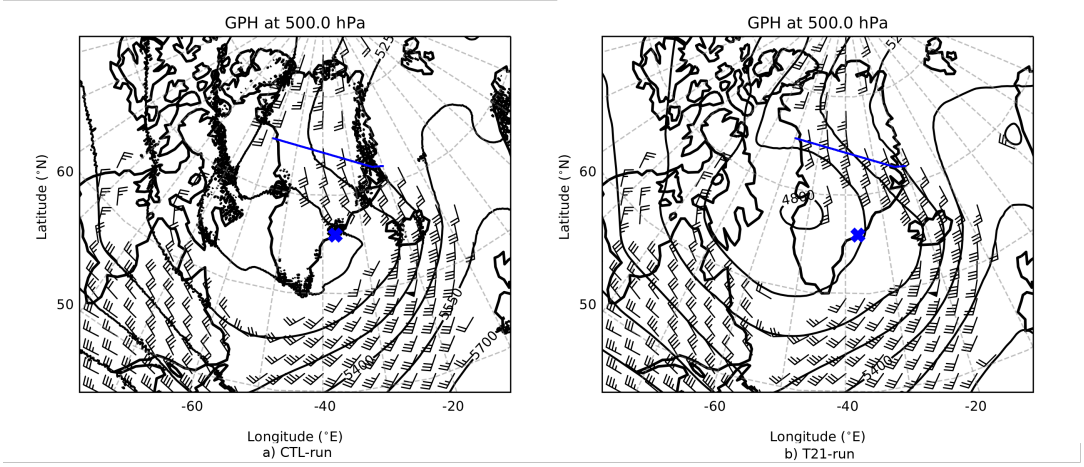

Figure 6.11: Geopotential heights and winds at 500 hPa valid for 9 March 2016 18:00 UTC for the CTL-run (a) and the T21-run (b). Note the spotted (especially along the coast lines) CTL-run is a result of the orographic GW drag parameterization scheme. The rest of the display is the same as in Fig. 6.1, but with no PV line.

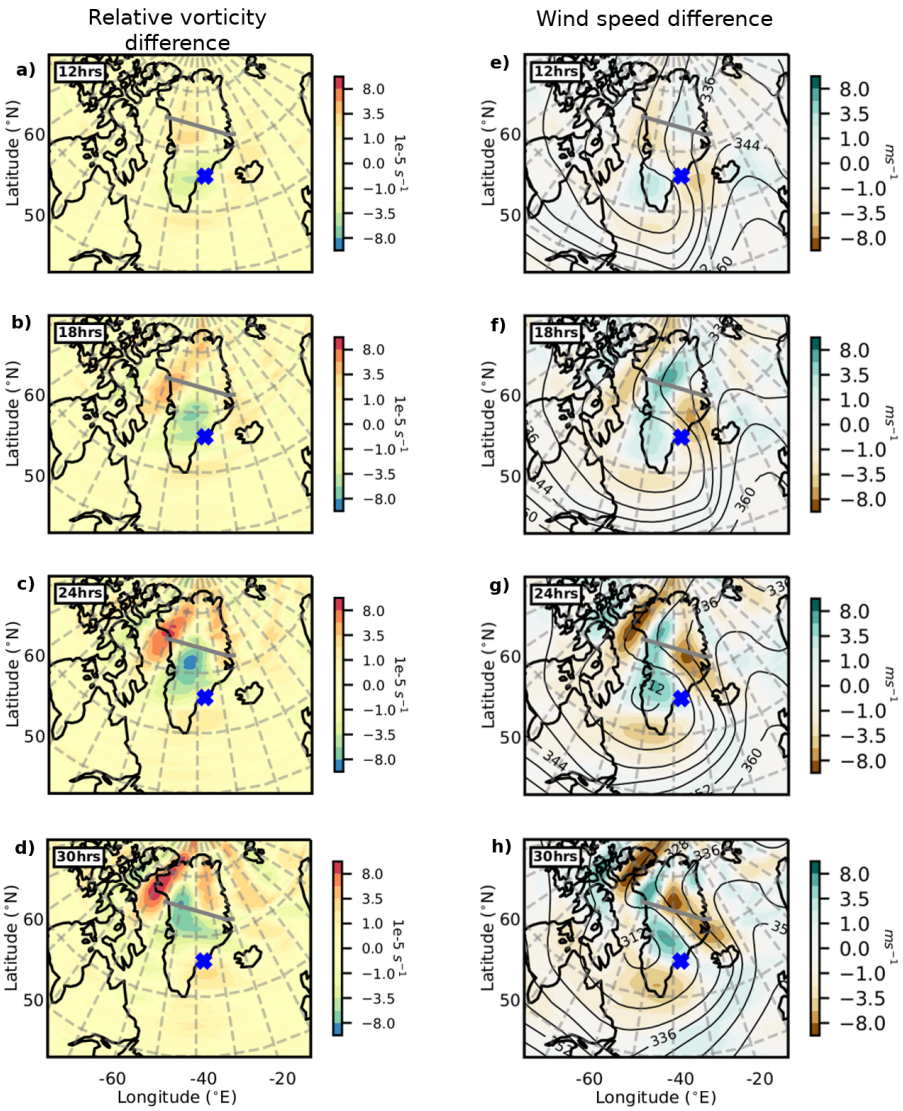

Figure 6.12: Difference between the CTL-run and T21-run for relative vorticity (left) and background total wind velocity (right) at 8 km. The revealed dipole structure is closely related to the GW excitation. The dipole structure in the wind speed difference (e–h) and the relative vorticity difference (a–d) field is offset by half a phase (90°). Isobars (thin black line — in hPa) at the respective level is overlaid to indicate the shape of the jet. Coastline, flight path and the times indicated in top left is similar to Fig. 6.9.

Comparing the two model runs, the jet location and shape remained similar. The centre of the low pressure (being stronger in the T21-run) was displaced ≈5° westwards (Fig. 6.11). To find the missing link the difference in the model basic variables (U, V, temperature, pressure and relative vorticity) was calculated. Subtracting the wind speed and relative vorticity of the T21-run from the CTL-run produced an interesting dipole structure (Fig. 6.12). In Fig. 6.12e to h green (brown) demarcates an area where the CTL-run wind speed was faster (slower) than the T21-run. In order

to investigate the origin of this difference, it is convenient to calculate relative vorticity:

$$\zeta = \frac{\partial v}{\partial x} - \frac{\partial u}{\partial y}. \tag{6.1}$$

It is well known that an uplift process induces relative vorticity (Holton, 2004). It then should be remembered that relative vorticity is only a different expression for the same wind field and that any process which causes changes of vorticity is altering the wind velocity field[5]. The same dipole structure is observed in the relative vorticity but offset by 90°. The dipole structure in the wind speed and vorticity represents the changes that occurred in the wind speed, and consequently the changes that occurred in the jet.

The role of vorticity is known from the classical formation model of a Rossby wave (Holton, 2004). The flow above the ridge is compressed by the elevated orography, changing the potential temperature gradient, which in turn changes the vorticity, deflecting the wind and the synoptic flow. For the early time steps of 12hrs and 18hrs (Fig. 6.12a, b) there is a vorticity difference between the T21-run and the CTL-run over Greenland close to the coast. This is the same area where a change in uplift process would be expected due to the changes in the T21-run and CTL-run topography. This illustrates the effect that the uplift by orography has on the vorticity (and the jet). Later time steps (Fig. 6.12c–d and g–h) are more complex. Here it is expected that the jet adjusted itself due to the lack of orography, for example an adjustment to the orientation of the jet would additionally influence the relative vorticity field.

Vorticity can also be introduced by dissipation processes. This includes blocking (Smith, 1982), flow splitting (Siedersleben and Gohm, 2016), mountain wakes (Grubisic, 2004; Siedersleben and Gohm, 2016; Smith, 2019), breaking GWs (Siedersleben and Gohm, 2016) and wakes at the edges of mountain ranges (Grubisic, 2004). Given the location and synoptic conditions, all of the above processes most probably played a role in producing vorticity, but the dominant process (due to the altitude of the jet) is expected to be due to the compression of flow above Greenland. Eq. 9 in Uccellini and Koch (1987) shows that when the vorticity (term 2 on the right-hand side) changes, divergence will also change. Uccellini and Koch (1987) and references there-in found that an increase in divergence is directly linked to a more out of balance jet.

The difference in orography from the CTL-run to the T21-run induced different vorticity areas

[5]This is because vorticity and wind velocity distribution are different views of the same wind field linked by a mathematical transformation and not because of a physical cause and effect.

(Fig. 6.12). These changes in the wind field will change the components in the jet, bringing the Coriolis and pressure gradient forces out of balance. This will trigger the jet to spontaneously emit GWs in order to bring the forces back into balance. Trüb and Davies (1995) showed in an idealised model simulation that evanescent GWs form over broad terrain in flow with a Rossby number (Eq. 6.2) < 0.25 (see Fig. 6.13). Also, upwind and downwind of the mountain a change in the wind components was observed. For our case, using a wind of 30 m s^{-1}, Coriolis parameter of 0.00014 1/s and a mountain half-width measured from the blue X (Fig. 6.1) to the Greenland north coast of 1 650 km a Rossby number of 0.13 is achieved from

$$R_o = U/fL, \tag{6.2}$$

where U - total wind speed and L is mountain half-width (the width of the mountain at $0.5 \cdot$ mountain height).

The large evanescent GW (this should not be confused with the observations in Fig. 6.3, which clearly are propagating GWs), which is expected to form following Trüb and Davies (1995) over the Greenland terrain, can be one explanation of the rotation (Fig. 6.13) and the upstream slow down of the wind. Wind being uplifted by orography will decrease due to kinetic energy changing into potential energy. In the geostrophic balance, the Coriolis parameter is multiplied by the wind to obtain the Coriolis force, thus a slow down in the wind will change the Coriolis force. The Coriolis force deflects winds to the right in the Northern Hemisphere, acting on the zonal wind (u) component. This explains the changes in the zonal component in Fig. 6.13. Figure 6.13 is a clear indication of the horizontal and vertical extent that orography has on the background wind.

Based on the chain of arguments presented above it is clear that the observed GWs were excited by the jet. The dynamics of the jet was heavily influenced by orography through large-scale vorticity, forced by flow over broad terrain. According to Plougonven and Zhang (2014), our understanding of GWs from jets are still too inadequate to understand all the dynamics. With that in mind, it is acknowledged that the hypothesis presented here might not be the only feasible hypothesis. Only the study of Trüb and Davies (1995) has so far linked orography with the release of GWs which is not mountain waves. Trüb and Davies (1995) goes further in saying that observational evidence of GWs linked to orography induced ageostrophic imbalanced flow “will be difficult” to obtain.

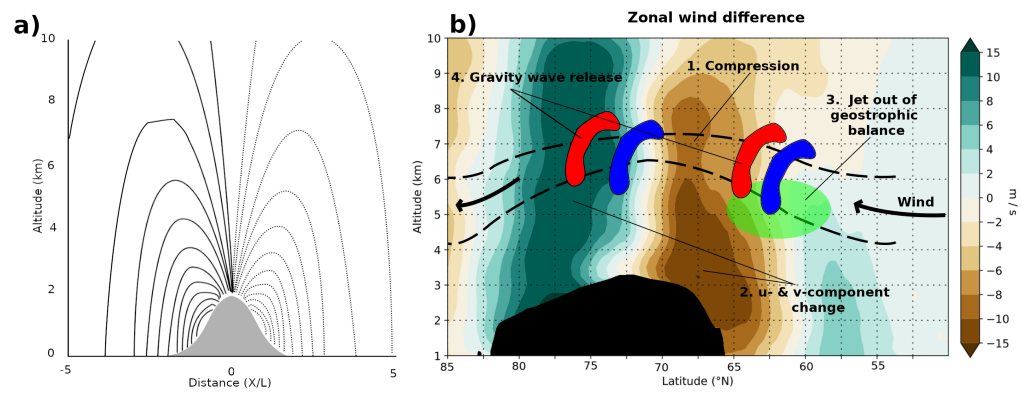

Figure 6.13: Panel a is reproduced from Trüb and Davies (1995) Fig. 11d and shows the along ridge velocity component. Their idealised numerical model revealed this dipole structure that forms above broad ridges for flow with a Rossby number $<$0.25 and a Froude number of 0.01. Panel b shows the difference between CTL-run and T21-run zonal wind (u) component at flight time. The zonal wind component represents an along-ridge wind (similar to panel a). The cross-section with altitude is aligned roughly along the jet axis (see Fig. 6.1 for the jet) at 40° W longitude from 85° N to 50° N. Black indicates the Greenland topography. The annotations, red, blue and green sections on the plot explains the new excitation mechanism — this is discussed in the summary.

6.5 Summary

This chapter illustrates how challenging it is to disentangle the sources of GWs. The GLORIA observed GW as input into GROGRAT show GWs drifting horizontally for more than 1000 kms over $\approx$15° of latitude. This reflects on the nonphysical nature of single column parameterization schemes currently in use for GWs (Kim et al., 2003; Preusse et al., 2009; Sato et al., 2012; Kalisch et al., 2014; Ribstein and Achatz, 2016; Amemiya and Sato, 2016; Krisch et al., 2017; Plougonven et al., 2020, e.g.) and confirms the hypothesis of (McLandress et al., 2012) that models require meridional propagation (key point 2 in Chapter 1). With the help of observations, GROGRAT and a numerical experiment a new GW source mechanism is identified. Wind approaching topography is uplifted and compressed above the ridge (dashed lines on Fig. 6.13). The compressed air deflects the wind (induce vorticity). The change in the wind components results in the forces in the jet to be out of geostrophic balance (green on Fig. 6.13 — this occurred upwind in this case study). The out of balance jet will release energy in order to bring the forces in the jet back into balance. The release of energy is realised by the excitation of GWs. The new source mechanism is the jet that was heavily influenced by orography through large-scale vorticity, forced by flow over broad terrain. It is likely that this jet-orography interaction causes the jet to come out of balance on a frequent basis in many regions for example Greenland, Scandinavia, Antarctica, South Amer-

ica, New Zealand and others. This means that this new source (key point 3 in Chapter 1) can induce substantially more NOGWD than what we currently assume (key point 1.2 in Chapter 1). A literature study revealed no other studies linking topography with upwind GWs or any mention of this orography-jet combination.

Chapter 7

Conclusion

Gravity waves form an indirect but integral part of general circulation models. These models oversimplify GWs to a high degree in their parameterisation schemes, which results in a high degree of uncertainty. This uncertainty can affect the weather predictions over the medium term and the climate projections over the long term. This thesis mainly relies on observations to better understand GW excitation and propagation. The results and new understanding presented here lead to suggestions for improvements in general circulation models.

Suggested improvements are in the form of abstracted conceptual models. Conceptual models are a powerful tool of physics as they allow quantitative understanding. These conceptual models can be implemented/integrated in a computationally efficient way in physics parameterisation schemes. Furthermore, conceptual models make predictions about physical behaviour and need to be based on sound physics. This requires the theoretical predictions to be checked and confirmed by observations — first, as a general principle of natural science and second, to avoid, for example, an oversimplification. Three regions for improvement were identified:

One: An analysis of the GW physics in connection with low-level blocking reveals an oversimplification in the implementation of the orographic gravity wave parameterisations and simplified mountain wave models. **Objective 1 analysed the orographic GW physics employed in standard general circulation models (for example, ECMWF IFS) to assess any shortcomings.** This objective was addressed in Chapter 3 and part of Geldenhuys (2022). Current equations in the models reduce the GW drag exponentially in the vicinity of low-level blocking. Chapter 3 provides five arguments why the GW drag should be larger (than parameterisations expect) when low-level blocking is present. Firstly, the blocking jet blows perpendicularly to mountainside ridges,

which lead up to the main ridge. This creates prime conditions for mountain wave formation. Secondly, air passing over the blocking layer and spilling to the lee side of the mountain can accelerate down the lee slope, adjust with a hydraulic jump and trigger GW formation. Thirdly, blocking acts to widen the mountain barrier and can hence induce GWs above a seemingly broader barrier than the width of the ridge. Fourthly, the broad barrier can push the jet out of geostrophic balance and can trigger GWs similar to the discussion in Chapter 6. Fifthly, the blocking layer forms a dynamic barrier that acts as a mountain and can induce GWs. Not one of these mechanisms is implemented in parameterisations. Hence, unless so-generated GWs are explicitly resolved, the associated GWMF originating from these mechanisms is not captured.

Two: Observations presented here confirm the theoretical concept of horizontal refraction for which only indirect observational evidence was available. The effect of refraction has been absent in GW parameterisation schemes to date. **Objective 2 set out to investigate observations of a case study with refraction and with southwards propagation.** The observations of a SouthTRAC case study (Chapter 5 and Geldenhuys et al. (2022)) reveals that refraction can be an important mechanism concerning GWMF. Observations include two orographic and one non-orographic GW packet over the southern Andes. The fact that a non-orographic GW is found over orography shows the importance of detailed GW observations and source characterisation. Many studies only use spatial collocation to assign GW drag to orographic and non-orographic sources, respectively. The discussed case is clear evidence that this is not a good approach.

The raytracing experiments clearly indicate that meridional propagation is important (Figs. 5.7 and 5.12). This is further evidence showing that the location of the GW drag deposition is incorrect in GW drag schemes assuming only vertical propagation. More important in this case study was the contribution of refraction during meridional propagation. Refraction, in this case, resulted in a 25% increase in GWMF during the lifetime of the single GW. The additional GWMF was deposited in the Stratosphere where it can greatly influence dynamics. Literature suggests that a similar result is expected from a GW packet. Follow-up experiments show that this is not an everyday occurrence for a single location and occurs approximately once per month. A single region like the Drake Passage and surrounding area reveals an increase in GWMF a couple of times per week; on a latitude circle, it occurs virtually every day. The increase in GWMF is not captured by parameterisations and can have a significant impact on dynamics. Refraction was observed in the troposphere by GLORIA and in the Mesosphere by ALIMA. To our knowledge, this thesis presents the first direct observation of horizontal refraction acting on an individual wave packet.

Three: Observations provide evidence that orographic and non-orographic GWs have been oversimplified and are not as separated in nature as we treat them in the models. Here a new GW source was identified, which was previously unknown to the community. **Objective 3 investigated non-orographic gravity wave drag and meridional propagation and found observational evidence of a new GW source.** The study revealed that the observed GW propagated laterally $\approx$2 000 km from its source and across 15-20° of latitude (Fig. 6.5). The wave encountered a critical layer whereby it deposited its GWMF. This is clear evidence that GWs can propagate across many latitudes to deposit their GWMF at very different locations.

Observations and multiple tools were used to identify a new GW source combination of orography and spontaneous imbalance discussed in Chapter 6 and published in Geldenhuys et al. (2021). Raytracing of an observed GW traced back the origin of the wave to the open ocean rather than the topography of Greenland. However, a numerical model simulation with strongly reduced and smoothed topography but otherwise equal flow conditions generated no GWs, implying that topography is a necessary ingredient for the GWs to form. Analysis revealed that the topography lifts and compresses the jet, pushing it out of geostrophic balance. This takes place above the topography but also upwind. The out-of geostrophic-balance jet excites GWs to bring the Coriolis and the pressure gradient force back into balance. A literature study shows that this mechanism has not been identified before and represents a new so-far undiscovered source.

7.1 Summary

This dissertation used GLORIA tomographic observations in order to investigate GW excitation and propagation. In the introduction (Chapter 1) literature was summarised to reveal the key missing elements surrounding GWs are: (1) models require more GW drag (orographic and/or non-orographic GW drag), (2) models require meridional propagation and (3) observations of GWs and its sources are required to verify our physical understanding. With this in mind, three objectives were designed to address the oversimplifications in models and provide specific outcomes addressing the three above-mentioned key points. This dissertation analysed GW physics in the orographic GW drag model parameterisations and found it provided too little GW drag in the vicinity of low-level blocking. Blocking yields five additional scenarios where GWs can form; all previously not accounted for in the oversimplified parameterisation schemes. High-resolution observations from the SouthTRAC campaign were used to show refraction is important during

meridional propagation and can make a sizeable contribution to the GW momentum flux of a single GW. This was the very first direct observation of atmospheric GW refraction taking place. Lastly, a new GW source combination was uncovered in PGGS campaign data. This produced observational evidence of a GW phenomenon previously unknown to the community.

Appendix: Gravity wave sources

A.1 Inertial instability

Inertial instability is a form of dynamic instability which results in the transfer of kinetic energy from the background flow to the disturbance (or the GW) (AMS, 2018). Inertial instability forms in a rotating flow when the centrifugal force is larger on the displaced parcel than on the background flow. From an earth system view, earths angular speed is so large that the disturbance is stable. But when applied to low-latitudes the angular speed of earth with respect to a local vertical is small and the disturbance can grow at the expense of the background flow. The centrifugal force accelerates parcels of air polewards which can trigger a local signature of a tropopause fold when it overrides the stratospheric air (Rowe and Hitchman, 2015, and references therein). The variation of acceleration in the x- and y-directions creates convergent and divergent zones.

In the atmosphere, inertial instabilities resemble thin 'pancake' structures of a few hundred meters thick (Strube et al., 2020). Inertial instability is diagnosed where (Holton, 2004):

$$f(f+\zeta) < 0, \tag{1}$$

where ζ is vorticity ($\frac{\partial v}{\partial x} - \frac{\partial u}{\partial y}$). In the Northern (Southern) Hemisphere f is positive (negative) and inertial instability requires the absolute vorticity ($f+\zeta$) term to be negative (positive). Once a pancake layer is inertially unstable, unstable motions form to mix the air laterally. This turbulent mixing would continue to occur until the inertial instability coefficient (Eq. 1) becomes positive. This continuous mixing results in the pancake structures becoming turbulent layers (Rowe and Hitchman, 2015, and references therein). Rowe and Hitchman (2015) argue that inertial instability acts to enhance convergence and divergence of winds, thereby generating GWs. Holton (2004) describes inertial instabilities to be most pronounced on the anticyclonic shear side of upper level

jets (that is the equatorward side of a westerly jet). This means that inertial instabilities enhance the likelihood of an out-of-balance jet, thereby triggering a GW release. Rowe and Hitchman (2015) studied GWs from inertial instabilities between two jets with horizontal wavelengths of about 100 km. They found that the GWs modulates the two jets connecting them in a 'rib-like' fashion.

A.2 Wind shear and Kelvin-Helmholtz waves

Wind shear is another possible source of GWs (Lott, 1997). Wind shear can occur throughout the atmosphere, but frequently occurs along the flanks of jet streams. Wind shear is defined as the change in wind speed in the horizontal or in the vertical. Two fluids of a different speed existing next to one-another creates a shear instability (Fig. 1). Shear instability (also known as Kelvin-Helmholtz instability) is one of the many parts that make up dynamic instability[1].

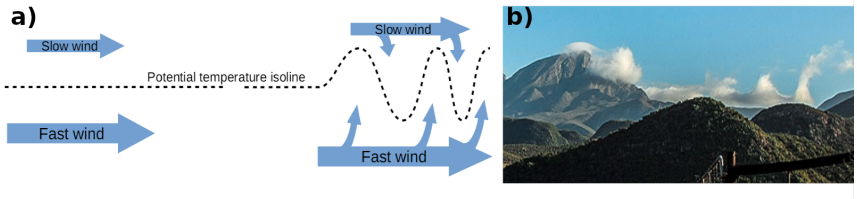

Figure 1: Panel (a): Shear instability in the form of Kelvin-Helmholtz waves created by two fluids with different velocities. Panel (b): Kelvin-Helmholtz waves takes shape in the lee of the mountain. The cap cloud (cloud on top of the mountain peak) suggests the wind was blowing from left to right in the photo with the mountain shading the lee side. A stratus cloud situated in the lee of the mountain was shaded from the stronger wind upstream of the mountain — forming the layer with the slower wind speed. The stronger flow passing over the barrier (and above cloud level) started dragging the slower flow in the cloud triggering a disturbance. Note how the disturbance grew with time from left to right. The right most wave is overturning and will soon dissipate into turbulence. Photo adapted from: www.meiringspoortchallenge.co.za/mountain-bike/gallery/gallery-2021/

In a two layer system with differing speeds the faster flow drags the slower flow along to generate a small disturbance (Fig. 1). The process is analogous to the wind creating ripples on water. The instability allows these disturbances to grow into waves with a structure similar to corrugated iron. The amplitude of the wave structure is dependent on the initial Richardson number, the horizontal wavelengths can extend up to 10 km (Fritts and Rastogi, 1985b) and the ground-based phase speed of the wave match that of the background wind speed (Fritts and Alexander, 2003). These Kelvin-Helmholtz waves grow exponentially with time until dissipation

[1] Also known as hydrodynamic instability — other dynamic instabilities include inertial instability, baroclinic instability, barotropic instability and rotational instability (AMS, 2018).

(Fritts and Rastogi, 1985b). After the Kelvin-Helmholtz waves become turbulent the region is characterised by homogenisation whereby strong stratification and shear is eroded. This can trigger secondary shear instabilities. The large-amplitude Kelvin-Helmholtz waves are believed to excite propagating GWs of a scale larger than the Kelvin-Helmholtz waves. The short horizontal wavelengths triggered by the wind shear mechanism will result in high-frequency GWs.

Literature suggests a second GW excitation mechanism linked with shear instabilities. Buehler et al. (1999) mathematically and numerically show that the Kelvin-Helmholtz waves break and induce mixing through clear air turbulence. This creates a 'pancake' layer of a few km's in the horizontal and a few hundred meters in the vertical (similar to an inertial instability layer). The mixing erodes the temperature, stability and wind gradients, causing the turbulent layer to collapse. This triggers a low-frequency GW with dimensions comparable to that of the turbulent layer emitted in all directions. The horizontal wavelengths from this mechanism is longer than the one described by Fritts and Rastogi (1985b) and has a higher likelihood to propagate longer distances without reflection (see Sect. 2.1.1 for details on reflection).

Shear instability exists in regions with a critical Richardson number (Fritts and Rastogi, 1985b; Holton, 2004):

$$\mathrm{Ri} = \frac{N^2}{(\frac{\partial \bar{u}}{\partial z})^2}, \tag{2}$$

where $\bar{u}$ is the mean background wind. A critical Richardson number of less than 0.25 frequently occurs as a result of large scale GWs or from low-frequency motions in a region of uniform stratification (Fritts and Rastogi, 1985b). Nath and Chen (2013) state that a wind shear greater than $10\,\mathrm{m\,s^{-1}\,km^{-1}}$ is sufficient to induce small Richardson numbers for the excitation of propagating GWs. Pramitha et al. (2015) observed propagating GWs and attributed them to a region of wind shear of $\approx 9\,\mathrm{m\,s^{-1}\,km^{-1}}$. Nath and Chen (2013) found no correlation between the wind shear intensity and the observed GW amplitudes. Both GWs observed in Nath and Chen (2013) and Pramitha et al. (2015) were high-frequency GWs (see Sect. 2.1.1 for a description on the types of GWs). Pramitha et al. (2015) observed shear generated GWs with horizontal wavelengths between 2 km to 134 km, however observation occurred far from their source meaning the wavelengths could have changed in time.

A.3 Katabatic winds

A katabatic wind is a wind that blows downslope from higher topography to the mountain foot (AMS, 2018). Colder (or denser) air on a plateau will sink down the slope forming a downslope wind. The sinking air gathers speed and momentum and will continue sinking past its equilibrium position where buoyancy will counteract its downward momentum, exciting a GW (as described under GW excitation at the beginning of this section). Alternatively the downslope wind can gather enough speed to obtain a supercritical Froude number ($Fr > 1$) whereby the flow can adjust via a hydraulic jump (Fig. 2 — this would be how a downslope windstorm forms) (Yu and Cai, 2006). This hydraulic jump can also excite a propagating GW.

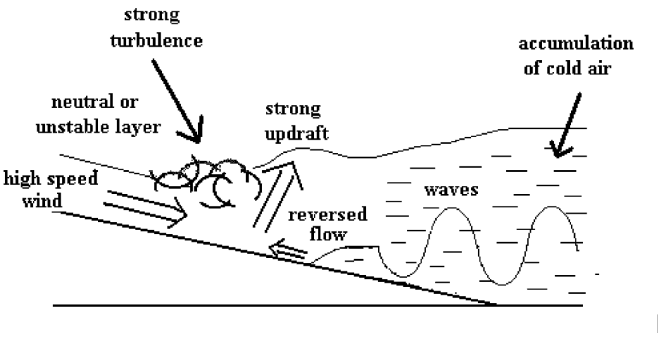

Figure 2: Conceptual model of a katabatic hydraulic jump from Yu and Cai (2006).

Propagating GWs from katabatic winds have been observed off the coast of Antarctica (e.g. Yu and Cai, 2006; Watanabe et al., 2006; Vignon et al., 2020), over Greenland (Tollinger et al., 2019) and in South Africa (Geldenhuys et al., 2019). Yu and Cai (2006) used a high-resolution model to simulate the katabatic hydraulic jump. The model showed the jump region to have a horizontal scale of ≈500 m with strong vertical motions up to 1.5 m s^{-1} (Fig. 2). The jump region was shown to excite propagating waves with a wavelength of ≈1 km. Tollinger et al. (2019) showed a cross-section through high-resolution model data (their Fig. 9d) revealing ≈20 km horizontal wavelength.

A.4 Convection

Convection is a well known GW source mechanism (e.g. Salby and Garcia, 1987; Pfister et al., 1993; Alexander and Pfister, 1995; Chun and Baik, 1998; Beres et al., 2004; Choi et al., 2012). Convection in itself is a dynamically complex and diverse process, hence it can generate GWs by multiple mechanisms (Fritts and Alexander, 2003). Literature describes three mechanisms:

thermal forcing, mechanical oscillator effect, and a moving mountain effect.

Thermals form when the surface supplies heat to the atmosphere (AMS, 2018). A thermal is created once a region of air has been sufficiently heated to become unstable and rise in a current. When these currents condensate, latent heating is produced which warms the atmosphere locally (Song et al., 2003). The local heating perturbs the air nearby the convection, which excites convective GWs by the thermal forcing mechanism. Work by Salby and Garcia (1987) showed that thermal forcing generate a wide variety of different frequency GWs by adiabatic heating. Propagating GWs from this mechanism have a vertical wavelength equal to twice the depth of the thermal forcing but quickly is refracted to the depth of the thermal forcing (Salby and Garcia, 1987; Garcia and Salby, 1987; McLandress et al., 2000; Fritts and Alexander, 2003).

The updrafts and downdrafts in the convective cell is the mechanical oscillator in the mechanical oscillator effect. All convective clouds in the developing (also called cumulus stage) and mature stages are characterised to have an updraft (Wallace and Hobbs, 2006). However, air can not always constantly be moving upwards, and hence a corresponding downdraft forms and the convective cell enters the mature stage. All mature and dissipating stage convective cells are characterised to have downdrafts. Throughout most of the lifetime of the convective cell a constant updraft and downdraft co-exist. These up-and-down movements on a stable atmosphere[2] simulates that of a mechanical oscillator (Fovell et al., 1992); similar to a stone being dropped in water. The mechanical oscillator produces high-frequency GWs (similar to the thermal mechanism) with short horizontal wavelengths. The GW frequencies were found to simulate the oscillation frequencies of the up- and downdrafts. Alexander and Pfister (1995) observed high-frequency GWs from the mechanical oscillator effect with horizontal wavelengths $\approx$10–100 km on either side of the convective updrafts.

The moving mountain effect functions similar to topographic sources (Fritts and Alexander, 2003). The convective cloud (or the latent heat released by the condensation) creates an obstacle for winds. The winds are forced to rise over this temporary barrier (Fig. 3). On the lee side the parcel of air is not at equilibrium and a GW is excited (via the process discussed under GW excitation at the start of this section). Observations of low-frequency GWs with wavelengths $\approx$200–2 000 km from this mechanism are described in Vincent and Alexander (2000). In a numerical study Clark et al. (1986) found that the moving mountain effect is a more efficient mechanism and create GWs with a higher amplitude compared to the thermal forcing mechanism.

[2]For example the tropopause region (Kim et al., 2003).

Convectively generated GWs are perhaps the most diverse type of GWs and can have virtually any vertical or horizontal scales (McLandress et al., 2000; Fritts and Alexander, 2003). The fact that convectively generated GWs can be anything from from high-frequency to low-frequency are attributed to the different mechanisms and the complex nature of convection. Lane and Knievel (2005) found that models tend to exaggerate the lowest part of the convective GW spectrum that it can resolve. This makes the models convective GWs less trustworthy and emphasise the need for observations.

Figure 3: A photo of a GW that was excited by a convective tower/cumulus cloud. The cauliflower cloud structure is the convective cloud and the lenticular clouds above that show the GWs. The fact that the length scale of the lenticular cloud matches the length scale of the convective tower hints toward the obstacle effect as the source mechanism. Note the lenticular clouds slants left with height, which indicates this is a propagating GW. Photo was taken coming in to land at Ushuaia, Argentina.

A.5 Fronts

A front is defined as the separation line between two airmasses with different temperature values (AMS, 2018). For example, a cold front is a line that separates the equatorward moving cold polar air and the cool environmental air. Cold and warm fronts are dynamically complex regions well known to be associated with other GW sources like the jet stream, convection and baroclinic instability (Fritts and Alexander, 2003). Both the jet and convection are well known GW sources and are discussed separately. Alternatively, fronts can excite GWs through two mechanisms: via an obstacle effect (Ralph et al., 1999) or via an imbalance in the flow (Fritts and Alexander, 2003) (similar to an out-of-balance jet stream — Sect. 2.1.2).

An unbalanced flow achieves a balanced state by redistributing energy, which frequently is by exciting GWs. This redistribution of energy and momentum implies that the GWs are more likely found in regions of wind deceleration. GWs from unbalanced flow in vicinity of the front and jet were observed and discussed by Koch et al. (2005). They observed a region of unbalanced frontogenesis on the cyclonic side of the jet, which was formed by increased ageostrophic

forces during frontogenesis. The unbalanced region excited GWs with horizontal wavelengths of 120–216 km. However, also smaller scale high-frequency GWs were observed with horizontal wavelengths of 1–20 km. Similar to an out-of-balance jet stream, the GW characteristics from the adjustment process are linked to the size and timescale of the source region (Fritts and Alexander, 2003). Vertical wavelengths of a few km's and horizontal wavelengths of ≈10–100 times larger are typical. If the source is elongated the orientation of the GWs are parallel to the source axis.

The obstacle effect is very similar to topography or the moving mountain mechanism from convection. The front is characterised as a line that runs perpendicular to the mean flow (AMS, 2018). The leading edge of the frontal line is characterised by updrafts and an airmass with different temperatures and pressures than the surrounding environment (Ralph et al., 1999). The frontal line is also frequently characterised by a large mass of clouds. This creates a temporary obstacle where airflow is directed around or over the temporary barrier instead of through this region. This results in GWs in the cross-frontal directions. Similar to mountain waves, the GWs from this mechanism are expected to propagate upwards and remain stationary with respect to the cold front. Ralph et al. (1999) documents observations of GWs from this mechanism with a horizontal wavelength of 60 km and vertical motions of 1 m s^{-1}.

A.6 GW Breaking

Secondary GWs are emitted during the breaking of other GWs. GW breaking is a non-linear process whereby the GW lose energy and deposit GWMF. During GW breaking the energy is passed down to smaller scales (Pierrehumbert, 1986) and turbulence acts to turn the energy into thermal energy. During this non-linear process, small-scale high-frequency GWs are created with scales smaller than the breaking GWs (Zhou et al., 2002; Vadas et al., 2018).

The small-scale GWs generated after breaking typically propagate only small distances before also breaking and depositing their momentum (Zhou et al., 2002; Vadas et al., 2018). Given that the GWs do not propagate far, it is frequently ignored and classified as part of the transition to heat through turbulence. The deposition of GWMF accelerates the background wind in the direction of the primary GW wavevector. The region of acceleration is larger than the breaking GW as a result of the short propagation of the small-scale GWs. The acceleration takes place in the ageostrophic wind (the meridional component) and will push the wind out of geostrophic balance. The out-of-balance wind will radiate energy (similar to the discussion in Sect. 2.1.2) and generate

a low-frequency GW (called a secondary GW). The scale of the large-scale secondary GWs are nicely illustrated by an example from Vadas et al. (2018) (and references there-in); A breaking GW with two cycles will produce a breaking region with a width of 2 wavelengths. After transition to turbulence the region is twice the size (making it 4 wavelengths wide). Such a region will then generate a GW with a wavelength 8 times the original wavelength. These large-scale secondary GWs are low-frequency GWs created from linear processes (even though the wave breaking is a non-linear process) (Zhou et al., 2002).

Similar to GWs excited by an out-of-balance jet, these secondary GWs are emitted both upwards and downwards and are identifiable by fishbone structures in the data (Vadas et al., 2018). During GW breaking the fishbone structure is visible in all directions, except perpendicular to the acceleration force direction. The study of Vadas et al. (2018) observed secondary GWs with vertical wavelengths of 6 to 14 km in lidar data over Antarctica. The process of GW breaking is discussed in more detail in Section 2.4

A.7 Rossby waves / Tropopause folds

Rossby waves are complex dynamical systems with multiple possible GW sources (similar to fronts and jet streams). Rossby waves are characterised by meandering jet streams (first possible source) frequented by cold fronts (second possible source) and is known to favour convection (third mechanism). These three mechanisms are discussed above and this subsection focuses on another mechanism, namely tropopause undulations. The compression of isotherms in the cold air advection region of a Rossby wave is well known to trigger undulations in the tropopause (Hirschberg and Fritsch, 1991). The tropopause undulations is frequently associated with tropopause folds (Wallace and Hobbs, 2006).

Some studies have observed GWs in the region of tropopause folds and tropopause undulations (e.g. Koch et al., 2005). However, until recently the mechanism remained unknown with most studies attributing the GWs to a different source (e.g. jet stream by Buss et al. (2004) or mountain waves by Woiwode et al. (2018)). Recently Dörnbrack et al. (2021) observed long horizontal wavelength GWs in the stratosphere from a lidar and attributed the GWs to the depression caused by the tropopause. The undulation in the tropopause is similar to a valley in the topography. The winds relative to the moving depression sinks into the depression and create a propagating GW. It remains unsure whether this is similar to the katabatic wind effect or whether it is similar to a

moving mountain effect (although Dörnbrack et al. (2021) compares this to drifting convection and hence to the moving mountain effect).

A.8 Volcanoes

Volcanoes have been observed to trigger GWs from multiple mechanisms, some of which we do not fully understand. It is known that the plume of the volcano can act as a dynamic obstacle and can trigger GWs similar to a mountain or a convective cloud (De Angelis et al., 2011). However, in the recent volcanic eruption of 14 January 2022 close to Tonga a new and not fully understood mechanism was observed (Adam, 2022). The volcanic eruption triggered multiple concentric rings of GWs (similar to a pebble dropped in a pond). The very large spectrum of GWs was observed to occur from the surface up to the Ionosphere. One possible explanation for these GWs can be the warm and rapidly rising plume displacing the air parcels outwards and upwards. The large scale GWs originating from the Tonga volcano was observed on satellite data to have horizontal wavelengths in the order of 500 km and vertical wavelengths of 20 km (Ern, 2022).

A.9 Others

Other GW sources at the surface include tsunamis (Artru et al., 2005), explosions (Harkrider, 1964) and the electrical field generated before earthquakes (Hegai et al., 2006). Other GW sources located in the free atmosphere include auroral heating (Fritts and Alexander, 2003), eclipse cooling (Fritts and Alexander, 2003) and a planetary wave induced critical layer in the polar vortex (Polichtchouk and Scott, 2020).

A.10 Summary

The GW review paper by Fritts and Alexander (2003) states that a full GW source survey is 'beyond our current state of knowledge'. The sources mentioned above are by no means complete, but include the ones that are believed to be important. From the discussion in this section it becomes clear that many of the sources rely on a small set of common mechanisms. The obstacle mechanism excites GWs by an obstacle in the path of the wind (examples of this includes topography, convection, fronts, Rossby waves, tsunamis and volcanic plumes). The flow imbalance

mechanism trigger GWs to reduce energy of the forces and bring the flow back into balance. The flow imbalance mechanism plays a role in the out-of-balance jet stream, inertial instability, fronts and GW breaking.

Acknowledgments

First and foremost I would like to thank the Creator for creating a vast universe with so many puzzles to solve and questions to answer. Similarly I give thanks for a sound mind and body to have been able to study these puzzles.

I am very grateful to Prof. Martin Riese who provided me with this wonderful opportunity to work on these projects and the datasets. I am extremely grateful for the patience and assistance my direct supervisors (Dr. Peter Preusse and Dr. Jörn Ungermann) provided me with. Without your guiding hand myself, and this dissertation, would have been much poorer. Thank you all for the exposure and the opportunities you provided me with, they definitely changed my outlook on life.

I am deeply indebted to my fellow PhD students (Isabell Krisch, Conny Strube, Sebastian Rhode, and especially, Lukas Krasauskas). Your support and help really meant a lot to me.

I would like to thank HITEC Graduate school for the scholarship and funding my research stay in Argentina.

Lastly, thank you for the unconditional support from my wife. Your sacrifices did not go unnoticed! A special kind of thanks to my baby daughter Klara, who kept me awake at strange hours in the night to devise, formulate and finish my second paper. Sonder julle twee aan my sy sou die tyd hier nie die moeite werd gewees het nie!!

List of Figures

List of Tables

List of Equations

List of symbols

- $x,\ y,\ z$ - traditional coordinate directions
- ρ - density
- p - pressure
- R - gas constant for a dry ($286.9\,\mathrm{J\,kg^{-1}\,K^{-1}}$) or moist ($461.4\,\mathrm{J\,kg^{-1}\,K^{-1}}$) air.
- Ω - angular velocity of earth ($7.292 \times 10^{-5}\,\mathrm{rad\,s^{-1}}$)
- ϕ - latitude
- H - density height scale
- $k,\ l,\ m$ - wavenumbers in the $x,\ y,\ z$ -directions
- N - Brünt-Väisälä frequency
- g - gravity constant at $9.8\,\mathrm{m\,s^{-1}}$
- $\bar{\theta}$ - layer averaged potential temperature
- $\bar{U}$ - wind perpendicular to the GW phase fronts
- $\bar{u}_{perp}$ - wind perpendicular to the mountain averaged from surface to mountain top
- h_m - observable mountain height (valley floor to peak)
- Fr - Froude number
- u - zonal wind component
- v - meridional wind component.
- $_a$ - ageostrophic wind component

- C - group phase speed
- $_{gb}$ - with respect to the ground
- λ_z - vertical wavelength
- λ_h - horizontal wavelength
- T - temperature
- $_0$ - value at reference level
- Ri - Richardson number
- d - length of the region that is considered.
- $u_h{}'$ - total wind speed amplitude
- C_{gb_H} - horizontal phase speed
- $\bar{U}$ - horizontal wind along the wavevector $((ku+lv)/k_h)$.
- τ_{GWD} - GW drag
- E - enhancement factor
- m_{no} - number of mountains
- λ_{eff} - grid length or acts as a tuning coefficient
- G - asymptotic function to facilitate a smooth transition between 2-D blocking and non-blocking cases
- U_{ref} - horizontal wind speed at reference level that is projected onto the low-level wind direction
- b - mountain height variation in the along-ridge direction
- G_s - function of mountain sharpness
- γ - represents mountain anisotropy
- B - function of γ which can vary from 1 for a 2-D ridge and $\pi/4$ for a circular mountain
- H_{eff} - effective mountain height

- Z_{blk} - depth of the blocking layer
- $J(n)$ - cost function
- o - actual measurements
- $F(n)$ - simulated measurements for atmospheric state n
- S_ε - expected instrument errors
- t - time
- U - total wind speed
- L - mountain half-width (the width of the mountain at $0.5 \cdot \text{mountain height}$)

List of abbreviations

- ALIMA - Airborne LIdar for the Middle Atmosphere
- ECMWF - European Centre for Medium-Range Weather Forecasts
- ERA5 - ECMWF Reanalysis 5th Generation Description
- FAT - full-angle tomography
- GDAS - Global Data Assimilation System
- GLORIA - Gimballed Limb Observer for Radiance Imaging of the Atmosphere
- GOES - Geostationary Operational Environmental Satellite
- GROGRAT - Gravity-wave Regional Or Global Ray Tracer
- GWMF - gravity wave momentum flux
- GW - gravity wave
- HALO - High Altitude LOng range
- IFS - Integrated Forecast System
- JURASSIC2 - Juelich Rapid Spectral Simulation Code version 2
- LAT - limited-angle tomography
- MERRA-2 - Modern-Era Retrospective analysis for Research and Applications
- MLS - Microwave Limb Sounder
- NCEP - National Centres for Environmental Prediction
- NOGWD - non-orographic GW drag

- OGWD - orographic GW drag
- ROMIC - Role if the Middle Atmosphere in Climate
- WACCM - Whole Atmosphere Community Climate Model
- WKB - Wentzel-Kramers-Brillouin
- WRF - Weather Research and Forecasting model

Bibliography

D. Adam. Nature news, 2022. URL https://www.nature.com/articles/d41586-022-00127-1. last access: 21 January 2022.

M. J. Alexander and C. D. Barnet. Using satellite observations to constrain gravity wave parameterizations for global models. *J. Atmos. Sci.*, 64(5):1652–1665, 2007.

M. J. Alexander and L. Pfister. Gravity wave momentum flux in the lower stratosphere over convection. *Geophys. Res. Lett.*, 22(15):2029–2032, 1995. doi: 10.1029/95GL01984.

M. J. Alexander and K. H. Rosenlof. Nonstationary gravity wave forcing of the stratospheric zonal mean wind. *J. Geophys. Res.*, 101(D18):23465–23474, 1996. doi: 10.1029/96JD02197.

P. Alexander, A. de la Torre, P. Llamedo, R. Hierro, T. Marcos, B. Kaifler, A. Giez, M. Rapp, and J. L. Hormaechea. The coexistence of gravity waves from diverse sources during a southtrac flight with optimal vertical propagation conditions. *J. Geophys. Res.*, 2022. to be submitted.

A. Amemiya and K. Sato. A new gravity wave parameterization including three-dimensional propagation. *Journal of the Meteorological Society of Japan. Ser. II*, 94(3):237–256, 2016. doi: 10.2151/jmsj.2016-013.

AMS. American meteorological society glossary website, 2018. URL http://glossary.ametsoc.org/wiki/Main_Page. last access: 9 March 2020.

D. G. Andrews, J. R. Holton, and C. B. Leovy. *Middle Atmosphere Dynamics*, volume 40 of *International Geophysics Series*. Academic Press, 1987.

J. Artru, V. Ducic, H. Kanamori, P. Lognonne, and M. Murakami. Ionospheric detection of gravity waves induced by tsunamis. *Geophys. J. Int.*, 160(3):840–848, MAR 2005. doi: 10.1111/j.1365-246X.2005.02552.x.

J. Bacmeister, P. Newman, B. Gary, and K. Chan. An algorithm for forecasting mountain wave-related turbulence in the stratosphere. *Wea. Forecast.*, 9(2):241–253, JUN 1994. doi: 10.1175/1520-0434(1994)009<0241:AAFFMW>2.0.CO;2.

R. Barry. *Mountian weather and climate*. Cambridge University Press, third edition edition, 2008. doi: 10.1017/CBO9780511754753.

G. Bell and L. Bossart. Appalachian Cold-Air Damming. *Mon. Weath. Rev.*, 116:137–161, 1988. doi: 10.1175/1520-0493(1988)116<0137:ACAD>2.0.CO;2.

J. H. Beres, M. J. Alexander, and J. R. Holton. A method of specifying the gravity wave spectrum above convection based on latent heating properties and background wind. *J. Atmos. Sci.*, 61 (3):324–337, 2004.

J. Berner, U. Achatz, L. Battè, L. Bengtsson, A. de la Camara, H. M. Christensen, M. Colangeli, D. R. B. Coleman, D. Crommelin, S. I. Dolaptchiev, P. F. C. L. E. Franzke, P. Imkeller, H. Järvinen, S. Juricke, V. Kitsios, F. Lott, V. Lucarini, S. Mahajan, T. N. Palmer, C. Penland, M. Sakradzija, J. von Storch, A. Weisheimer, M. Weniger, P. D. Williams, and J. Yano. STOCHASTIC PARAMETERIZATION Toward a New View of Weather and Climate Models. *Bull. Amer. Meteor. Soc.*, 98:565–588, 2007. doi: 10.1175/BAMS-D-15-00268.1.

G. Boeloeni, Y.-H. Kim, S. Borchert, and U. Achatz. Toward Transient Subgrid-Scale Gravity Wave Representation in Atmospheric Models. Part I: Propagation Model Including Nondissipative Wave–Mean-Flow Interactions. *J. Atmos. Sci.*, 78:1317–1338, 2021. doi: 10.1175/JAS-D-20-0065.1.

T. Bradbury. Wind shear and waves. *Sailplane and Gliding. August-September*, pages 178–182, 1991.

M. Bramberger, A. Dörnbrack, H. Wilms, S. Gemsa, K. Raynor, and R. Sharman. Vertically propagating mountain waves — a hazard for high flying aircraft? *J. Appl. Met. Clim.*, 57, 2018. doi: 10.1175/JAMC-D-17-0340.1.

O. Buehler and M. E. McIntyre. Remote recoil: a new wave-mean interaction effect. *J. Fluid Mech.*, 492:207–230, 2003. doi: 10.1017/S0022112003005639.

O. Buehler, M. McIntyre, and J. Scinocca. On shear-generated gravity waves that reach the mesosphere. part I: Wave generation. *J. Atmos. Sci.*, 56:3749–3773, 1999. doi: 10.1175/1520-0469(1999)056<3749:OSGGWT>2.0.CO;2.

S. Buss, A. Hertzog, C. Hostettler, T. Bui, D. Luthi, and H. Wernli. Analysis of a jet stream induced gravity wave associated with an observed stratospheric ice cloud over Greenland. *Atmos. Chem. Phys.*, 4:1183–1200, AUG 3 2004. doi: 10.5194/acp-4-1183-2004.

M. Charron and E. Manzini. Gravity waves from fronts: Parameterization and middle atmosphere response in a general circulation model. *J. Atmos. Sci.*, 59:923–941, 2002.

C. Chen and X. Chu. Two-dimensional morlet wavelet transform and its application to wave recognition methodology of automatically extracting two-dimensional wave packets from lidar observations in antarctica. *J. Atm. Sol.-Terr. Phys.*, 162:12,737–12,750, 2017. doi: 10.1016/j.jastp.2016.10.016.

C.-C. Chen, D. Durran, and G. Hakim. Mountain-wave momentum flux in an evolving synoptic-scale flow. *J. Atmos. Sci.*, 62(9):3213 – 3231, 2005. doi: 10.1175/JAS3543.1.

H.-J. Choi, H.-Y. Chun, J. Gong, and D. L. Wu. Comparison of gravity wave temperature variances from ray-based spectral parameterization of convective gravity wave drag with AIRS observations. *J. Geophys. Res.*, 117, MAR 8 2012. doi: 10.1029/2011JD016900.

H.-Y. Chun and J.-J. Baik. momentum flux by thermally induced internal gravity waves and its approximation fpr large-scale models. *J. Atmos. Sci.*, 55:3299–3310, 1998.

T. L. Clark, T. Hauf, and J. P. Kuettner. Convectively forced internal gravity waves: Results from two-dimensional numerical experiments. *Quart. J. Roy. Meteorol. Soc.*, 112(474):899–925, 1986. doi: 10.1002/qj.49711247402.

Copernicus Climate Change Service (C3S). Era5: Fifth generation of ecmwf atmospheric reanalyses of the global climate., 2017. URL `https://cds.climate.copernicus.eu/cdsapp#!/home`.

T. Crouch. Encyclopedia britannica: Sir george cayley, n.d. URL `https://www.britannica.com/biography/Sir-George-Cayley`. last access: 26 April 2022.

S. De Angelis, S. R. McNutt, and P. W. Webley. Evidence of atmospheric gravity waves during the 2008 eruption of Okmok volcano from seismic and remote sensing observations. *Geophys. Res. Lett.*, 38, MAY 18 2011. doi: 10.1029/2011GL047144.

A. de la Camara, F. Lott, and A. Hertzog. Intermittency in a stochastic parameterization of nonorographic gravity waves. *J. Geophys. Res. Atmos.*, 119(21):11905–11919, NOV 16 2014a. doi: 10.1002/2014JD022002.

A. de la Camara, F. Lott, and A. Hertzog. Intermittency in a stochastic parameterization of nonorographic gravity waves. *J. Geophys. Res. Atmos.*, 119(21):11905–11919, NOV 16 2014b. doi: 10.1002/2014JD022002.

A. de la Camara, F. Lott, V. Jewtoukoff, R. Plougonven, and A. Hertzog. On the gravity wave forcing during the southern stratospheric final warming in LMDZ. *J. Atmos. Sci.*, 73(8):3213–3226, AUG 2016. ISSN 0022-4928. doi: 10.1175/JAS-D-15-0377.1.

DLR. Halo website, 2022a. URL `https://halo-research.de/sience/previous-missions/polstracc/`. Retrieved on 2022-03-03.

DLR. Halo website, 2022b. URL `https://halo-research.de/about/background/`. Retrieved on 2022-03-03.

A. Dörnbrack, T. Gerz, and U. Schumann. Turbulent breaking of overturning gravity waves below a critical level. *Applied Scientific Research*, 54:163–176, 1995. doi: 10.1007/BF00849114.

A. Dörnbrack, S. Eckermann, B. Williams, and J. Haggerty. Stratospheric gravity waves excited by a propagating Rossby wave train – a DEEPWAVE case study. *J. Atmos. Sci.*, 2021. doi: 10.1175/JAS-D-21-0057.1.

J. Doyle, V. Grunisic, W. Brown, S. De Wekker, A. Dörnbrack, Q. Jiang, S. Mayor, and M. Weissmann. Observations and numerical simulations of subrotor vortices during t-rex. *Journal of Atmospheric Sciences*, 66:1229–1249, 2009. doi: 10.1175/2008JAS2933.1.

P. Drobinski, J. Dusek, and C. Flamant. Diagnostics of hydraulic jump and gap flow in stratified flows over topography. *Boundary-Layer Meteorology*, 98:475–495, 2001. doi: 10.1023/A:1018703428762.

S. Dunlop. *Oxford Dictionary of Weather*. Oxford University Press, second edition, 2012.

D. Durran. Comments on “gravity wave refraction by three-dimensionally varying winds and the global transport of angular momentum”. *J. Atmos. Sci.*, 66(7):2150 – 2152, 2009. doi: 10.1175/2008JAS3013.1.

D. R. Durran. Lee Waves and Mountain Waves. *University of Washington, Seattle, USA*, 2003. URL `https://www.atmos.washington.edu/2010Q1/536/2003AP_lee_waves.pdf`.

A. Dörnbrack, B. Kaifler, N. Kaifler, M. Rapp, N. Wildmann, M. Garhammer, K. Ohlmann, J. M. Payne, M. Sandercock, and E. J. Austin. Unusual appearance of mother-of-pearl clouds above el calafate, argentina (50°21's, 72°16'w). 75(12):378–388, 2020. doi: 10.1002/wea.3863.

S. Eckermann. On the observed morphology of gravity-wave and equatorial-wave variance in the stratosphere. *J. Atm. Terr. Phys.*, 57(2):105–134, 1995. doi: 10.1016/0021-9169(93)E0027-7.

S. D. Eckermann and C. J. Marks. GROGRAT: a new model of the global propagation and dissipation of atmospheric gravity waves. *Adv. Space Res.*, 20:1253–1256, 1997.

S. D. Eckermann and P. Preusse. Global measurements of stratospheric mountain waves from space. *Science*, 286(5444):1534–1537, 1999. doi: 10.1126/science.286.5444.1534.

S. D. Eckermann, I. Hirota, and W. K. Hocking. Gravity wave and equatorial wave morphology of the stratosphere derived from long-term rocket soundings. *Quart. J. Roy. Meteorol. Soc.*, 121 (521):149–186, 1995.

ECMWF. *PART IV: DYNAMICS ANDNUMERICAL PROCEDURES*, chapter 5, pages 1–210. Number 4 in IFS Documentation. ECMWF, 2015. doi: 10.21957/p50qmwprw.

ECMWF. European Centre for Medium-Range Weather Forecasts: Summary of cycle 45r1, 2022. URL `https://www.ecmwf.int/en/forecasts/documentation-and-support/evolution-ifs/cycles/summary-cycle-45r1`. Retrieved on 2022-03-04.

B. Ehard, B. Kaifler, A. Dörnbrack, P. Preusse, S. Eckermann, M. Bramberger, S. Gisinger, N. Kaifler, B. Liley, J. Wagner, and M. Rapp. Horizontal propagation of large amplitude mountain waves in the vicinity of the polar night jet. *J. Geophys. Res. Atmos.*, pages 1423–1436, 2017. doi: 10.1002/2016JD025621.

M. K. Ejiri, T. Nakamura, T. T. Tsuda, T. Nishiyama, M. Abo, C.-Y. She, M. Nishioka, A. Saito, T. Takahashi, K. Tsuno, T. D. Kawahara, T. Ogawa, and S. Wada. Observation of synchronization between instabilities of the sporadic e layer and geomagnetic field line connected f region medium-scale traveling ionospheric disturbances. *J. Geophys. Res. Space*, 124(6):4627–4638, 2019. doi: 10.1029/2018JA026242.

M. Ern. personal communication, February 2022.

M. Ern, P. Preusse, M. J. Alexander, and C. D. Warner. Absolute values of gravity wave momentum flux derived from satellite data. *J. Geophys. Res. Atmos.*, 109(D20), 2004. doi: 10.1029/2004JD004752.

M. Ern, P. Preusse, and C. D. Warner. Some experimental constraints for spectral parameters used in the Warner and McIntyre gravity wave parameterization scheme. *Atmos. Chem. Phys.*, 6(12):4361–4381, 2006. doi: 10.5194/acp-6-4361-2006.

M. Ern, M. Diallo, P. Preusse, M. G. Mlynczak, M. J. Schwartz, Q. Wu, and M. Riese. The semiannual oscillation (SAO) in the tropical middle atmosphere and its gravity wave driving in reanalyses and satellite observations. *Atmos. Chem. Phys.*, 21:13763–13795, 2021. doi: 10.5194/acp-21-13763-2021.

M. Ern, P. Preusse, and M. Riese. Driving of the SAO by gravity waves as observed from satellite. *Ann. Geophys.*, 33(4):483–504, 2015. doi: 10.5194/angeo-33-483-2015.

M. Ern, Q. T. Trinh, M. Kaufmann, I. Krisch, P. Preusse, J. Ungermann, Y. Zhu, J. C. Gille, M. G. Mlynczak, J. M. Russell, III, M. J. Schwartz, and M. Riese. Satellite observations of middle atmosphere gravity wave absolute momentum flux and of its vertical gradient during recent stratospheric warmings. *Atmos. Chem. Phys.*, 16(15):9983–10019, AUG 9 2016. doi: 10.5194/acp-16-9983-2016.

R. Ford, M. McIntyre, and W. Norton. Balance and the slow quasimanifold: Some explicit results. *J. Atmos. Sci.*, 57:1236–1254, 2000. doi: 10.1175/1520-0469(2000)057<1236:BATSQS.2.0.CO;2.

R. Fovell, D. Durran, and J. R. Holton. Numerical simulations of convectively generated stratospheric gravity waves. *J. Atmos. Sci.*, 49:1427–1442, 1992.

F. Friedl-Vallon, T. Gulde, F. Hase, A. Kleinert, T. Kulessa, G. Maucher, T. Neubert, F. Olschewski, C. Piesch, P. Preusse, H. Rongen, C. Sartorius, H. Schneider, A. Schönfeld, V. Tan, N. Bayer, J. Blank, R. Dapp, A. Ebersoldt, H. Fischer, F. Graf, T. Guggenmoser, M. Höpfner, M. Kaufmann, E. Kretschmer, T. Latzko, H. Nordmeyer, H. Oelhaf, J. Orphal, M. Riese, G. Schardt, J. Schillings, M. K. Sha, O. Sumińska-Ebersoldt, and J. Ungermann. Instrument concept of the imaging Fourier transform spectrometer GLORIA. *Atmos. Meas. Tech.*, 7(10):3565–3577, 2014. doi: 10.5194/amt-7-3565-2014.

D. Fritts and M. Alexander. Gravity wave dynamics and effects in the middle atmosphere. *Rev. Geophys.*, 41(1), APR 16 2003. doi: 10.1029/2001RG000106.

D. Fritts and P. Rastogi. Convective and dynamical instabilities due to gravity wave motions in the lower and middle atmosphere: Theory and observations. *Radio Sci.*, 20(6):1247–1277, 1985a. doi: 10.1029/RS020i006p01247.

D. C. Fritts and P. K. Rastogi. Convective and dynamical instabilities due to gravity wave motions in the lower and middle atmosphere: theory and observations. *Radio Sci.*, 20:1247–1277, 1985b.

D. C. Fritts, R. B. Smith, M. J. Taylor, J. D. Doyle, S. D. Eckermann, A. Doernbrack, M. Rapp, B. P. Williams, P. D. Pautet, K. Bossert, N. R. Criddle, C. A. Reynolds, P. A. Reinecke, M. Uddstrom, M. J. Revell, R. Turner, B. Kaifler, J. S. Wagner, T. Mixa, C. G. Kruse, A. D. Nugent, C. D. Watson, S. Gisinger, S. M. Smith, R. S. Lieberman, B. Laughman, J. J. Moore, W. O. Brown, J. A. Haggerty, A. Rockwell, G. J. Stossmeister, S. F. Williams, G. Hernandez, D. J. Murphy, A. R. Klekociuk, I. M. Reid, and J. Ma. The deep propagating gravity wave experiment (DEEPWAVE): An airborne and ground-based exploration of gravity wave propagation and effects from their sources throughout the lower and middle atmosphere. *Bull. Amer. Meteor. Soc.*, 97(3):425–453, MAR 2016. doi: 10.1175/BAMS-D-14-00269.1.

S. Gabersek and D. Durran. Gap flows through idealized topography. part 1: Forcing by large-scale winds in the nonrotating limit. *J. Atmos. Sci.*, 61:2846–2862, 2004. doi: 10.1175/JAS-3340.1.

A. Gabriel. Ozone-gravity wave interaction in the upper stratosphere/lower mesosphere. *Atmos. Chem. Phys. Discuss.*, 2022:1–24, 2022. doi: 10.5194/acp-2021-1066.

R. Garcia and M. Salby. Transient-response to localized episodic heating in the tropics. 2. far-field behavior. *J. Atmos. Sci.*, 44(2):499–530, JAN 15 1987. doi: {10.1175/1520-0469(1987)044<0499:TRTLEH>2.0.CO;2}.

R. R. Garcia, A. K. Smith, D. E. Kinnison, A. de la Camara, and D. J. Murphy. Modification of the gravity wave parameterization in the whole atmosphere community climate model: Motivation and results. *J. Atmos. Sci.*, 74(1):275–291, 2017. doi: 10.1175/JAS-D-16-0104.1.

R. Gelaro, W. McCarty, M. J. Suárez, R. Todling, A. Molod, L. Takacs, C. A. Randles, A. Darmenov, M. G. Bosilovich, R. Reichle, K. Wargan, L. Coy, R. Cullather, C. Draper, S. Akella, V. Buchard, A. Conaty, A. M. da Silva, W. Gu, G.-K. Kim, R. Koster, R. Lucchesi, D. Merkova, J. E. Nielsen, G. Partyka, S. Pawson, W. Putman, M. Rienecker, S. D. Schubert, M. Sienkiewicz, and B. Zhao.

The modern-era retrospective analysis for research and applications, version 2 (MERRA-2). 30 (14):5419 – 5454, 2017. doi: 10.1175/JCLI-D-16-0758.1.

M. Geldenhuys. *Blocking, gap flow and mountain wave interaction along the coastal escarpment of South Africa*. University of Pretoria, Department of Geography, Geo-informatics and Meteorology, University of Pretoria, Lynnwood Road, Pretoria, Hillcrest, 2018. doi: hdl.handle.net/2263/68011. MSc dissertation.

M. Geldenhuys. On gravity wave parameterisation in vicinity of low-level blocking. *Atmospheric Science Letters*, 2022. doi: 10.1002/asl.1084.

M. Geldenhuys, L. Dyson, and D. van der Mescht. Blocking, gap flow and mountain wave interaction along the coastal escarpment of South Africa. *Theoretical and Applied Climatology*, 139: 1291–1303, 2019. doi: 10.1007/s00704-019-03030-4.

M. Geldenhuys, P. Preusse, I. Krisch, C. Zülicke, J. Ungermann, M. Ern, F. Friedl-Vallon, and M. Riese. Orographically induced spontaneous imbalance within the jet causing a large-scale gravity wave event. *Atmos. Chem. Phys.*, 2021. doi: 10.5194/acp-21-10393-2021.

M. Geldenhuys, B. Kaifler, P. Preusse, J. Ungermann, P. Alexander, L. Krasauskas, S. Rhode, W. Woiwode, M. Ern, M. Rapp, and M. Riese. Observations of gravity wave refraction and its causes and consequences. *J. Geophys. Res.*, 2022. Submitted.

V. Grubisic. Bora-driven potential vorticity banners over the adriatic. *Quart. J. Roy. Meteorol. Soc.*, 130:2571–2603, 2004. doi: 10.1256/qj.03.71.

V. Grubisic and J. Lewis. Sierra wave project revisited. *Bull. Amer. Meteor. Soc.*, pages 1127–1142, 2004. doi: 10.1175/BAMS-85-8-1127.

F. Guest, M. Reeder, C. Marks, and D. Karoly. Inertia-gravity waves observed in the lower stratosphere over Macquarie Island. *J. Atmos. Sci.*, 57(5):737–752, 2000.

D. Harkrider. Theoretical and observed acoustic-gravity waves from explosive sources in the atmosphere. *J. Geophys. Res.*, 69(24):5295–5321, 1964. doi: 10.1029/JZ069i024p05295.

A. Hasha, O. Bühler, and J. Scinocca. Gravity wave refraction by three-dimensionally varying winds and the global transport of angular momentum. *J. Atmos. Sci.*, 65:2892–2906, 2008.

A. Hauchecorne and M.-L. Chanin. Density and temperature profiles obtained by lidar between 35 and 70 km. *Geophys. Res. Lett.*, 7(8):565–568, 1980. doi: 10.1029/GL007i008p00565.

C. J. Heale, K. Bossert, S. L. Vadas, L. Hoffmann, A. Dörnbrack, G. Stober, J. B. Snively, and C. Jacobi. Secondary gravity waves generated by breaking mountain waves over europe. *J. Geophys. Res.*, 125, 2020. doi: 10.1029/2019JD031662.

V. Hegai, V. Kim, and J. Liu. The ionospheric effect of atmospheric gravity waves excited prior to strong earthquake. *Adv. Space Res.*, 37(4):653–659, 2006. doi: 10.1016/j.asr.2004.12.049.

H. Hersbach, B. Bell, P. Berrisford, S. Hirahara, A. Horanyi, J. Munoz-Sabater, J. Nicolas, C. Peubey, R. Radu, D. Schepers, A. Simmons, C. Soci, S. Abdalla, X. Abellan, G. Balsamo, P. Bechtold, G. Biavati, J. Bidlot, M. Bonavita, G. De Chiara, P. Dahlgren, D. Dee, M. Diamantakis, R. Dragani, J. Flemming, R. Forbes, M. Fuentes, A. Geer, L. Haimberger, S. Healy, R. J. Hogan, E. Holm, M. Janiskova, S. Keeley, P. Laloyaux, P. Lopez, C. Lupu, G. Radnoti, P. de Rosnay, I. Rozum, F. Vamborg, S. Villaume, and J.-N. Thepaut. The ERA5 global reanalysis. *Quart. J. Roy. Meteorol. Soc.*, 146(730):1999–2049, JUL 2020. doi: {10.1002/qj.3803}.

A. Hertzog, G. Boccara, R. A. Vincent, F. Vial, and P. Cocquerez. Estimation of gravity wave momentum flux and phase speeds from quasi-Lagrangian stratospheric balloon flights. part ii: Results from the vorcore campaign in antarctica. *J. Atmos. Sci.*, 65(10):3056–3070, 2008. doi: 10.1175/2008JAS2710.1.

A. Hertzog, C. Souprayen, and A. Hauchecorne. Observation and backward trajectory of an inertio-gravity wave in the lower stratosphere. *Ann. Geophys.*, 19(9):1141–1155, SEP 2001. ISSN 0992-7689.

P. Hirschberg and J. Fritsch. Tropopause undulations and the development of extratropical cyclones. Part II: Diagnostic analysis and conceptual model. *Mon. Weath. Rev.*, 119(2):518 – 550, 1991. doi: 10.1175/1520-0493(1991)119<0518:TUATDO>2.0.CO;2.

L. H. Holthuijsen. *Waves in oceanic and coastal waters*. Cambridge University Press, 2007. 1st edition.

J. R. Holton. *An introduction to dynamic meteorology*. Academic Press Limited, 2004. 3rd edition.

K. Huang, S. Zhang, and F. Yi. Reflection and transmission of atmospheric gravity waves in a stably sheared horizontal wind field. *J. Geophys. Res.*, 115, 2010. doi: 10.1029/2009JD012687.

ICAO. *Manual on Low-level Wind Shear*. International Civil Aviation Organization, 2005.

ICAO. *Annex3 to the convention on international civil aviation*. International Civil Aviation Organisation, 16th edition edition, 2007.

ISSI. International space science institute, 2022. URL `http://www.issibern.ch/teams/consonorogravity`. last access: 5 April 2022.

J. Jiang, B. Wang, K. Goya, K. Hocke, S. Eckermann, J. Ma, D. Wu, and W. Read. Geographical distribution and interseasonal variability of tropical deep convection: UARS MLS observations and analyses. *J. Geophys. Res. Atmos.*, 109(D3), FEB 13 2004. doi: 10.1029/2003JD003756.

B. Kaifler and N. Kaifler. A compact rayleigh autonomous lidar (CORAL) for the middle atmosphere. 14:1715–1732, 2021. doi: 10.5194/amt-14-1715-2021.

N. Kaifler, B. Kaifler, B. Ehard, S. Gisinger, A. Dornbrack, M. Rapp, R. Kivi, A. Kozlovsky, M. Lester, and B. Liley. Observational indications of downward-propagating gravity waves in middle atmosphere lidar data. *J. Atm. Sol.-Terr. Phys.*, 162(SI):16–27, SEP 2017. doi: 10.1016/j.jastp.2017.03.003.

S. Kalisch, P. Preusse, M. Ern, S. D. Eckermann, and M. Riese. Differences in gravity wave drag between realistic oblique and assumed vertical propagation. *J. Geophys. Res. Atmos.*, 119: 10,081–10,099, 2014. doi: 10.1002/2014JD021779.

J. Kidston, A. A. Scaife, S. C. Hardiman, D. M. Mitchell, N. Butchart, M. P. Baldwin, and L. J. Gray. Stratospheric influence on tropospheric jet streams, storm tracks and surface weather. *Nature Geosci.*, 8:433–440, 2015. doi: 10.1038/ngeo2424.

Y. H. Kim, A. C. Bushell, D. R. Jackson, and H.-Y. Chun. Impacts of introducing a convective gravity-wave parameterization upon the QBO in the met office unified model. *Geophys. Res. Lett.*, 40(9):1873–1877, MAY 16 2013. doi: 10.1002/grl.50353.

Y.-H. Kim, G. Boeloeni, S. Borchert, H. Chun, and U. Achatz. Toward Transient Subgrid-Scale Gravity Wave Representation in Atmospheric Models. Part II: Wave Intermittency Simulated with Convective Sources. *J. Atmos. Sci.*, 78:1339–1357, 2021. doi: 10.1175/JAS-D-20-0066.1.

Y.-J. Kim and A. Arakawa. Improvement of orographic gravity wave parameterization using a mesoscale gravity wave model. *Journal of Atmospheric Sciences*, 52:11875–1902, 1995. doi: 10.1175/1520-0469(1995)052<1875:IOOGWP>2.0.CO;2.

Y.-J. Kim and J. D. Doyle. Extension of an orographic-drag parameterization scheme to incorporate orographic anisotropy and flow blocking. *Quart. J. Roy. Meteorol. Soc.*, 131:1893–1921, 2005. doi: 10.1256/qj.04.160.

Y.-J. Kim, S. D. Eckermann, and H.-Y. Chun. An overview of the past, present and future of gravity-wave drag parameterization for numerical climate and weather prediction models. *Atmosphere-Ocean*, 41:65–98, 2003.

A. Kleinert, F. Friedl-Vallon, T. Guggenmoser, M. Höpfner, T. Neubert, R. Ribalda, M. K. Sha, J. Ungermann, J. Blank, A. Ebersoldt, E. Kretschmer, T. Latzko, H. Oelhaf, F. Olschewski, and P. Preusse. Level 0 to 1 processing of the imaging fourier transform spectrometer GLORIA: generation of radiometrically and spectrally calibrated spectra. *Atmos. Meas. Tech.*, 7(12): 4167–4184, 2014. doi: 10.5194/amt-7-4167-2014.

S. E. Koch, B. Jamison, C. Lu, T. Smith, E. Tollerud, C. Girz, N. Wang, T. Lane, M. Shapiro, D. Parrish, and O. Cooper. Turbulence and gravity waves within an upper-level front. *Journal of the Atmospheric Sciences*, 62:3885–3908, 2005. doi: 10.1175/JAS3574.1.

L. Krasauskas, J. Ungermann, S. Ensmann, I. Krisch, E. Kretschmer, P. Preusse, and M. Riese. 3-d tomographic limb sounder retrieval techniques: irregular grids and laplacian regularisation. *Atmos. Meas. Tech.*, 12(2):853–872, 2019. doi: 10.5194/amt-12-853-2019.

I. Krisch. *Tomographic observations of gravity waves with the infrared limb imager GLORIA*. Bergischen Universität Wuppertal: Fachbereich C - Mathematik und Naturwissenschaften, Bergische Universität Wuppertal, Gaußstraße 20, D-42119 Wuppertal, 2018. Dr. rer. nat. dissertation.

I. Krisch, P. Preusse, J. Ungermann, A. Dörnbrack, S. D. Eckermann, M. Ern, F. Friedl-Vallon, M. Kaufmann, H. Oelhaf, M. Rapp, C. Strube, and M. Riese. First tomographic observations of gravity waves by the infrared limb imager gloria. *Atmos. Chem. Phys.*, 17(24):14937–14953, 2017. doi: 10.5194/acp-17-14937-2017.

I. Krisch, J. Ungermann, P. Preusse, E. Kretschmer, and M. Riese. Limited angle tomography of mesoscale gravity waves by the infrared limb-sounder gloria. *Atmos. Meas. Tech.*, 11(7): 4327–4344, 2018. doi: 10.5194/amt-11-4327-2018.

I. Krisch, M. Ern, L. Hoffmann, P. Preusse, C. Strube, J. Ungermann, W. Woiwode, and M. Riese. Superposition of gravity waves with different propagation characteristics observed by airborne

and space-borne infrared sounders. *Atmos. Chem. Phys. Discuss.*, 2020:1–31, 2020. doi: 10.5194/acp-2020-327.

J. Küttner. Moazagotl und föhnwelle. *Beitr. Phys. Freien Atmos.*, 25:79–114, 1938.

T. P. Lane and J. C. Knievel. Some effects of model resolution on simulated gravity waves generated by deep mesoscale convection. *J. Atmos. Sci.*, 62:3408–3419, 2005.

S. T. Lang, A. Dawson, M. Diamantakis, P. Dueben, S. Hatfield, M. Leutbecher, T. Palmer, F. Prates, C. D. Roberts, I. Sandu, and N. Wedi. More accuracy with less precision. *Quart. J. Roy. Meteorol. Soc.*, 2021. doi: 10.1002/qj.4181. Accepted, In print.

N. Lareau and J. Horel. Dynamically Induced Displacements of a Persistent Cold-Air Pool. *Bound.-Layer Meteorol.*, 154:291–316, 2014. doi: 10.1007/s10546-014-9968-5.

R. Leighton and R. Feynman. *"Surely You're Joking, Mr. Feynman!": Adventures of a curious character*. W. W. Norton, 1985.

M. J. Lighthill. On sound generated aerodynamically, i. general theory. *Proc. Roy. Soc. London*, 211:564–587, 1952. doi: 10.1098/rspa.1952.0060.

M. J. Lighthill. Waves in fluids. *Cambridge University Press*, page 504pp, 1978.

K. A. Loescher, G. S. Young, B. A. Colle, and N. S. Winstead. Climatology of Barrier Jets along the Alaskan Coast. Part I: Spatial and Temporal Distributions. *Mon. Weath. Rev.*, 134:437–453, 2006. doi: 10.1175/MWR3037.1.

F. Lott. The transient emission of propagating gravity waves by a stably stratified shear layer. *Quart. J. Roy. Meteorol. Soc.*, 123(542):1603–1619, 1997. doi: 10.1002/qj.49712354208.

F. Lott and M. J. Miller. A new subgrid scale orographic drag parameterization: Its formulation and testing. *Quart. J. Roy. Meteorol. Soc.*, 123:101–127, 1997.

F. Lott, L. Guez, and P. Maury. A stochastic parameterization of non-orographic gravity waves: Formalism and impact on the equatorial stratosphere. *Geophys. Res. Lett.*, 39, MAR 31 2012. doi: 10.1029/2012GL051001.

R. Luna-Nino and T. Cavazos. Formation of a coastal barrier jet in the Gulf of Mexico due to the interaction of cold fronts with the Sierra Madre Oriental mountain range. *Quart. J. Roy. Meteorol. Soc.*, 144:115–128, 2017. doi: 10.1002/qj.3188.

C. Mallaun, A. Giez, and R. Baumann. Calibration of 3-d wind measurements on a singe engine research aircraft. *Atmos. Meas. Tech.*, 8:3177–3196, 2015. doi: 10.5194/amt-8-3177-2015.

E. Manzini, N. A. McFarlane, and C. McLandress. Impact of the doppler spread parameterization on the simulation of the middle atmosphere circulation using the ma/echam4 general circulation model. *J. Geophys. Res.*, 102:25751–25762, 1997.

C. J. Marks and S. D. Eckermann. A three-dimensional nonhydrostatic ray-tracing model for gravity waves: Formulation and preliminary results for the middle atmosphere. *J. Atmos. Sci.*, 52(11): 1959–1984, 1995. doi: 10.1175/1520-0469(1995)052<1959:ATDNRT>2.0.CO;2.

R. M. May, S. C. Arms, P. Marsh, E. Bruning, J. R. Leeman, K. Goebbert, J. E. Thielen, and Z. S. Bruick. Metpy: A Python package for meteorological data, 2008 - 2020. URL `https://github.com/Unidata/MetPy`.

M. McIntyre. Spontaneous imbalance and hybrid vortex– gravity structures. *J. Atmos. Sci.*, 66: 1315–1326, 2009. doi: 10.1175/2008JAS2538.1.

C. McLandress, M. J. Alexander, and D. L. Wu. Microwave Limb Sounder observations of gravity waves in the stratosphere: A climatology and interpretation. *J. Geophys. Res.*, 105(D9):11947–11967, 2000.

C. McLandress, T. G. Shepherd, S. Polavarapu, and S. R. Beagley. Is Missing Orographic Gravity Wave Drag near 60 degrees S the Cause of the Stratospheric Zonal Wind Biases in Chemistry Climate Models? *J. Atmos. Sci.*, 69(3):802–818, MAR 2012. doi: 10.1175/JAS-D-11-0159.1.

M. Mirzaei, C. Zülicke, A. Mohebalhojeh, F. Ahmad-Givi, and R. Plougonven. Structure, energy and parameterization of inertia-gravity waves in dry and moist simulations of a baroclinic wave life cycle. *J. Atmos. Sci.*, 71:2390–2414, 2014.

T. Mixa, A. Dörnbrack, and M. Rapp. Nonlinear simulations of gravity wave tunneling and breaking over auckland island. *J. Atmos. Sci.*, 78(5):1567 – 1582, 2021. doi: 10.1175/JAS-D-20-0230.1.

D. Nath and W. Chen. Investigating the dominant source for the generation of gravity waves during indian summer monsoon using ground-based measurements. *Adv. Atmos. Sci.*, 30(1): 153 – 166, 2013. doi: 10.1007/s00376-012-1273-y.

P. Neiman, E. Sukovich, F. Ralph, and M. Hughes. A Seven-Year Wind Profiler-Based Climatology of the Windward Barrier Jet along California's Northern Sierra Nevada. *Mon. Weath. Rev.*, 138, 2010. doi: 10.1175/2009MWR3170.1.

H. Oelhaf, B. Sinnhuber, W. Woiwode, H. Bo"nisch, H. Bozem, A. Engel, A. Fix, F. Friedl-Vallon, J. Grooß, P. Hoor, S. Johansson, T. Jurkat-Witschas, S. Kaufmann, M. Krämer, J. Krause, E. Kretschmer, D. Lörks, A. Marsing, J. Orphal, K. Pfeilsticker, M. Pitts, L. Poole, P. Preusse, M. Rapp, M. Riese, C. Rolf, J. Ungermann, C. Voigt, C. Volk, M. Wirth, A. Zahn, and H. Ziereis. Polstracc: Airborne experiment for studying the polar stratosphere in a changing climate with the high altitude and long range research aircraft (HALO). *Bull. Amer. Meteor. Soc.*, 100:2634–2664, 2019. doi: 10.1175/BAMS-D-18-0181.1.

A. Orr, P. Bechtold, J. Scinocca, M. Ern, and M. Janiskova. Improved middle atmosphere climate and forecasts in the ECMWF model through a nonorographic gravity wave drag parameterization. *J. Clim.*, 23:5905–5926, 2010. doi: 10.1175/2010JCLI3490.1.

D. O'Sullivan and T. J. Dunkerton. Generation of inertia-gravity waves in a simulated life cycle of baroclinic instability. *J. Atmos. Sci.*, 52(21):3695–3716, 1995. doi: {10.1175/1520-0469(1995)052<3695:GOIWIA>2.0.CO;2}.

J. Overland and N. Bond. Observations and Scale Analysis of Coastal Wind Jets. *Mon. Weath. Rev.*, 123:2934–2941, 1995. doi: 10.1175/1520-0493(1995)123<2934:OASAOC>2.0.CO;2.

T. R. Parish. Barrier Winds Along the Sierra Nevada Mountains. *J. Appl. Meteorol. Climatol. (1962-1982)*, 21(7):925–930, 1982. URL `http://www.jstor.org/stable/26180227`.

L. Pfister, S. Scott, M. Loewenstein, S. Bowen, and M. Legg. Mesoscale disturbances in the tropical stratosphere excited by convection: Observations and effects on the stratospheric momentum budget. *J. Atmos. Sci.*, 50(8):1058–1075, 1993.

R. Pierrehumbert. An essay on the parameterization of orographic gravity wave drag. In *Seminar/Workshop on Observation, Theory and Modelling of Orographic effects. Seminar: 15-19 September 1986, Workshop: 19-20 September 1986*, volume 1, pages 251–282, Shinfield Park, Reading, 1986. ECMWF, ECMWF. URL `https://www.ecmwf.int/node/11673`.

R. Plougonven and F. Zhang. Internal gravity waves from atmospheric jets and fronts. *Rev. Geophys.*, 52(1):33–76, MAR 2014. doi: 10.1002/2012RG000419.

R. Plougonven, A. de la Camara, A. Hertzog, and F. Lott. How does knowledge of atmospheric gravity waves guide their parametrizations? *Quart. J. Roy. Meteorol. Soc.*, pages 1529–1543, 2020. doi: DOI:10.1002/qj.3732.

I. Polichtchouk and R. K. Scott. Spontaneous inertia-gravity wave emission from a nonlinear critical layer in the stratosphere. *Quart. J. Roy. Meteorol. Soc.*, 146(728, A):1516–1528, APR 2020. doi: 10.1002/qj.3750.

I. Polichtchouk, T. G. Shepherd, and N. J. Byrne. Impact of Parametrized Nonorographic Gravity Wave Drag on Stratosphere-Troposphere Coupling in the Northern and Southern Hemispheres. *Geophys. Res. Lett.*, 45(16):8612–8618, AUG 28 2018a. doi: 10.1029/2018GL078981.

I. Polichtchouk, T. G. Shepherd, R. J. Hogan, and P. Bechtold. Sensitivity of the Brewer-Dobson Circulation and Polar Vortex Variability to Parameterized Nonorographic Gravity Wave Drag in a High-Resolution Atmospheric Model. *J. Atmos. Sci.*, 75(5):1525–1543, MAY 2018b. doi: 10.1175/JAS-D-17-0304.1.

M. Pramitha, M. Venkat Ratnam, A. Taori, B. V. Krishna Murthy, D. Pallamraju, and S. Vijaya Bhaskar Rao. Evidence for tropospheric wind shear excitation of high-phase-speed gravity waves reaching the mesosphere using the ray-tracing technique. *Atmos. Chem. Phys.*, 15: 2709–2721, 2015. doi: 10.5194/acp-15-2709-2015.

P. Preusse, A. Dörnbrack, S. D. Eckermann, M. Riese, B. Schaeler, J. T. Bacmeister, D. Broutman, and K. U. Grossmann. Space-based measurements of stratospheric mountain waves by CRISTA, 1. sensitivity, analysis method, and a case study. *J. Geophys. Res.*, 107(D23)(8178), 2002. doi: 10.1029/2001JD000699.

P. Preusse, S. D. Eckermann, and M. Ern. Transparency of the atmosphere to short horizontal wavelength gravity waves. *J. Geophys. Res.*, 113(D24104), 2008. doi: 10.1029/2007JD009682.

P. Preusse, S. D. Eckermann, M. Ern, J. Oberheide, R. H. Picard, R. G. Roble, M. Riese, J. M. Russell III, and M. G. Mlynczak. Global ray tracing simulations of the SABER gravity wave climatology. *J. Geophys. Res. Atmos.*, 114, 2009. doi: 10.1029/2008JD011214.

P. Preusse, M. Ern, P. Bechtold, S. D. Eckermann, S. Kalisch, Q. T. Trinh, and M. Riese. Characteristics of gravity waves resolved by ECMWF. *Atmos. Chem. Phys.*, 14(19):10483–10508, 2014. doi: 10.5194/acp-14-10483-2014.

F. Ralph, P. Neiman, and T. Keller. Deep-tropospheric gravity waves created by leeside cold fronts. *J. Atmos. Sci.*, 56:2986–3009, 1999. doi: 10.1175/1520-0469(1999)056<2986:DTGWCB>2.0.CO;2.

M. Rapp, B. Kaifler, A. Dörnbrack, S. Gisinger, T. Mixa, R. Reichert, N. Kaifler, S. Knobloch, R. Eckert, N. Wildmann, A. Giez, L. Krasauskas, P. Preusse, M. Geldenhuys, M. Riese, W. Woiwode, F. Friedl-Vallon, B.-M. Sinnhuber, A. de la Torre, P. Alexander, J. L. Hormaechea, D. Janches, M. Garhammer, J. L. Chau, J. F. Conte, P. Hoor, and A. Engel. SOUTHTRAC-GW: An Airborne Field Campaign to Explore Gravity Wave Dynamics at the World's Strongest Hotspot. *Bull. Amer. Meteor. Soc.*, 102(4), 2021. doi: 10.1175/BAMS-D-20-0034.1.

R. Reichert, B. Kaifler, N. Kaifler, M. Rapp, P. Pautet, M. Taylor, A. Kozlovsky, M. Lester, and R. Kivi. Retrieval of intrinsic mesospheric gravity wave parameters using lidar and airglow temperature and meteor radar wind data. *Atmos. Meas. Tech.*, 12:5997–6015, 2019. doi: 10.5194/amt-12-5997-2019.

B. Ribstein and U. Achatz. The interaction between gravity waves and solar tides in a linear tidal model with a 4-d ray-tracing gravity-wave parameterization. *J. Geophys. Res. Space*, 121(9): 8936–8950, 2016. doi: 10.1002/2016JA022478.

J. H. Richter, F. Sassi, and R. R. Garcia. Toward a physically based gravity wave source parameterization in a general circulation model. *J. Atmos. Sci.*, 67:136–156, 2010.

M. Riese, H. Oelhaf, P. Preusse, J. Blank, M. Ern, F. Friedl-Vallon, H. Fischer, T. Guggenmoser, M. Höpfner, P. Hoor, M. Kaufmann, J. Orphal, F. Plöger, R. Spang, O. Suminska-Ebersoldt, J. Ungermann, B. Vogel, and W. Woiwode. Gimballed limb observer for radiance imaging of the atmosphere (gloria) scientific objectives. *Atmos. Meas. Tech.*, 7(7):1915–1928, 2014. doi: 10.5194/amt-7-1915-2014.

L. Rothman, I. Gordon, Y. Babikov, A. Barbe, D. C. Benner, P. Bernath, M. Birk, L. Bizzocchi, V. Boudon, L. Brown, A. Campargue, K. Chance, E. Cohen, L. Coudert, V. Devi, B. Drouin, A. Fayt, J.-M. Flaud, R. Gamache, J. Harrison, J.-M. Hartmann, C. Hill, J. Hodges, D. Jacquemart, A. Jolly, J. Lamouroux, R. L. Roy, G. Li, D. Long, O. Lyulin, C. Mackie, S. Massie, S. Mikhailenko, H. Müller, O. Naumenko, A. Nikitin, J. Orphal, V. Perevalov, A. Perrin, E. Polovtseva, C. Richard, M. Smith, E. Starikova, K. Sung, S. Tashkun, J. Tennyson, G. Toon, V. Tyuterev, and G. Wagner. The HITRAN2012 molecular spectroscopic database. *J. Quant.*

Spectrosc. Radiat. Transfer, 130(0):4 – 50, 2013. doi: 10.1016/j.jqsrt.2013.07.002. HITRAN2012 special issue.

S. Rowe and M. Hitchman. On the role of inertial instability in stratosphere–troposphere exchange near midlatitude cyclones. *J. Atmos. Sci.*, 72(5):2131 – 2151, 2015. doi: 10.1175/JAS-D-14-0210.1.

M. L. Salby and R. R. Garcia. Transient response to localized episodic heating in the tropics. Part I: Excitation and short-time near-field behavior. *J. Atmos. Sci.*, 44(2):458–498, 1987. doi: 10.1175/1520-0469(1987)044<0458:TRTLEH>2.0.CO;2.

N. Samtleben, A. Kuchař, P. Šácha, P. Pišoft, and C. Jacobi. Impact of local gravity wave forcing in the lower stratosphere on the polar vortex stability: effect of longitudinal displacement. *Ann. Geophys.*, 38(1):95–108, 2020. doi: 10.5194/angeo-38-95-2020.

I. Sandu, P. Bechtold, A. Beljaars, A. Bozzo, F. Pithan, T. G. Shepherd, and A. Zadra. Impacts of parameterized orographic drag on the northern hemisphere winter circulation. *J. Adv. Model. Earth Syst.*, 8(1):196–211, MAR 2016. doi: 10.1002/2015MS000564.

K. Sato and S. Hirano. The climatology of the Brewer-Dobson circulation and the contribution of gravity waves. *Atmos. Chem. Phys.*, 19, 2019. doi: 10.5194/acp-19-4517-2019.

K. Sato, S. Watanabe, Y. Kawatani, Y. Tomikawa, K. Miyazaki, and M. Takahashi. On the origins of mesospheric gravity waves. *Geophys. Res. Lett.*, 36, OCT 7 2009. doi: 10.1029/2009GL039908.

K. Sato, S. Tateno, S. Watanabe, and Kawatani. Gravity wave characteristics in the Southern Hemisphere revealed by a high-resolution middle-atmosphere general circulation model. *J. Atmos. Sci.*, 69, 2012. doi: 10.1175/JAS-D-11-0101.1.

A. Savitzky and M. J. E. Golay. Smoothing and differentiation of data by simplified least squares procedures. *Analytical Chemistry*, 36(8):1627–1639, 1964. doi: 10.1021/ac60214a047.

A. A. Scaife, A. Y. Karpechko, M. P. Baldwin, A. Brookshaw, A. H. Butler, R. Eade, M. Gordon, C. MacLachlan, N. Martin, N. Dunstone, and D. Smith. Seasonal winter forecasts and the stratosphere. *Atmospheric Science Letters*, 17(1):51–56, 2016. doi: 10.1002/asl.598.

S. Serafin, M. Rotach, M. Arpagaus, I. Colfescu, J. Cuxart, S. De Wekker, M. Evans, V. Grubišic, N. Kalthoff, D. L. M. Karl, T. amd Kirshbaum, S. Mobbs, A. Paci, E. Palazzi, A. Bailey, J. Schmidli,

G. Wohlfahrt, and D. Zardi. *Multi-scale transport and exchange processes in the atmosphere over mountains*. Innsbruck University Press, First edition, 2020. doi: 10.15203/99106-003-1.

X. Shen, L. Wang, and S. Osprey. tropospheric forcing of the 2019 Antarctic sudden stratospheric warming. *Geophys. Res. Lett.*, 47:e2020GL089343, 2020. doi: 10.1029/2020GL089343.

S. Siedersleben and A. Gohm. The missing link between terrain-induced potential vorticity banners and banded convection. *Mon. Weath. Rev.*, 144:4063–4080, 2016. doi: 10.1175/MWR-D-16-0042.1.

R. Smith. 100 Years of Progress on Mountain Meteorology Research. *Meteorol. monogr.*, 59: 20.1–20.73, 2019. doi: 10.1175/AMSMONOGRAPHS-D-18-0022.1.

R. B. Smith. Synoptic observations and theory of orographically disturbed wind and pressure. *J. Atmos. Sci.*, 39:60–17, 1982. doi: 10.1175/1520-0469(1982)039<0060:SOATOO>2.0.CO;2.

R. B. Smith and C. G. Kruse. Broad-Spectrum Mountain Waves. *J. Atmos. Sci.*, 74:1381–1402, MAY 2017. doi: 10.1175/JAS-D-16-0297.1.

C. Snyder, W. Skamarock, and R. Rotunno. Frontal dynamics near and following frontal collapse. *J. Atmos. Sci.*, 50(18):3194–3211, 1993. doi: 10.1175/1520-0469(1993)050<3194:FDNAFF>2.0.CO;2.

C. Snyder, D. J. Muraki, R. Plougonven, and F. Zhang. Inertia-gravity waves generated within a dipole vortex. *J. Atmos. Sci.*, 64(12):4417–4431, 2007. doi: 10.1175/2007JAS2351.1.

I. S. Song, H. Y. Chun, and T. P. Lane. Generation mechanisms of convectively forced internal gravity waves and their propagation to the stratosphere. *J. Atmos. Sci.*, 60(16):1960 – 1980, 2003. doi: 10.1175/1520-0469(2003)060<1960:GMOCFI>2.0.CO;2.

C. Strube, M. Ern, P. Preusse, and M. Riese. Removing spurious inertial instability signals from gravity wave temperature perturbations using spectral filtering methods. *Atmos. Meas. Tech.*, 13(9):4927–4945, 2020. doi: 10.5194/amt-13-4927-2020.

C. Strube, P. Preusse, M. Ern, and M. Riese. Propagation paths and source distributions of resolved gravity waves in ecmwf-ifs analysis fields around the southern polar night jet. *Atmos. Chem. Phys.*, 21(24):18641–18668, 2021. doi: 10.5194/acp-21-18641-2021.

L. Thomas, R. M. Worthington, and M. A. McDonald. Inertia-gravity waves in the troposphere and lower stratosphere associated with a jet stream exit region. *Annales Geophysicae*, 17:115–121, 1999.

M. Tollinger, A. Gohm, and M. O. Jonassen. Unravelling the March 1972 northwest Greenland windstorm with high-resolution numerical simulations. *Quart. J. Roy. Meteorol. Soc.*, 145:3409–3431, 2019. doi: 10.1002/qj.3627.

C. Torrence and G. P. Compo. A practical guide to wavelet analysis. *Bull. Amer. Meteor. Soc.*, 79 (1):61 – 78, 1998. doi: 10.1175/1520-0477(1998)079<0061:APGTWA>2.0.CO;2.

F. Trey. Ein beitrag zum studium der luftwogen. *Meteorol. Zeitschrift*, 36:25–28, 1919.

Q. T. Trinh, S. Kalisch, P. Preusse, M. Ern, H.-Y. Chun, S. D. Eckermann, M.-J. Kang, and M. Riese. Tuning of a convective gravity wave source scheme based on hirdls observations. *Atmos. Chem. Phys.*, 16:7335–7356, 2016. doi: 10.5194/acp-16-7335-2016.

J. Trüb and H. Davies. Flow over a mesoscale ridge: pathways to regime transition. *Tellas A: Dynamic Meteorology and Oceanography*, 47(4):502–524, 1995. doi: 10.3402/tellusa.v47i4.11542.

L. W. Uccellini and S. E. Koch. The synoptic setting and possible energy sources for mesoscale wave disturbances. *Mon. Weath. Rev.*, 115(3):721–729, 1987.

J. Ungermann. *Tomographic reconstruction of atmospheric volumes from infrared limb-imager measurements*. Forschungszentrum Jülich, Jülich, 2011. URL `http://hdl.handle.net/2128/4385`. Ph.D. thesis, Wuppertal University.

J. Ungermann, M. Kaufmann, L. Hoffmann, P. Preusse, H. Oelhaf, F. Friedl-Vallon, and M. Riese. Towards a 3-D tomographic retrieval for the air-borne limb-imager GLORIA. *Atmos. Meas. Tech.*, 3(6):1647–1665, 2010. doi: 10.5194/amt-3-1647-2010.

J. Ungermann, A. Kleinert, G. Maucher, I. Bartolomé, F. Friedl-Vallon, S. Johansson, L. Krasauskas, and T. Neubert. Quantification and mitigation of the airborne limb imaging ftir gloria instrument effects and uncertainties. *Atmos. Meas. Tech. Discuss.*, 2021:1–69, 2021. doi: 10.5194/amt-2021-293.

S. L. Vadas and E. Becker. Numerical modeling of the generation of tertiary gravity waves in the mesosphere and thermosphere during strong mountain wave events over the Southern

Andes. *J. Geophys. Res. Space*, 124(9):7687–7718, SEP 2019. ISSN 2169-9380. doi: {10.1029/2019JA026694}.

S. L. Vadas and D. C. Fritts. The importance of spatial variability in the generation of secondary gravity waves from local body forces. *Geophys. Res. Lett.*, 29, 2002. doi: 10.1029/2002GL015574.

S. L. Vadas, J. Zhao, X. Chu, and E. Becker. The excitation of secondary gravity waves from body forces: Theory and observation. *J. Geophys. Res. Atmos.*, 0(ja), 2018. doi: 10.1029/2017JD027970.

D. Van der Mescht. *Mountain wave turbulence in the lee of the Hex River Mountains*. University of Stellenbosch: Department of Geography and Environmental studies, University of Stellenbosch, Western Cape, South Africa, 2013. MSc. thesis, University of Stellenbosch.

D. Van der Mescht and M. Geldenhuys. Observations of mountain waves with interference generated by coastal mountains in South Africa. *Meteorol. Appl.*, 26(3):409–415, 2019. doi: 10.1002/met.1771.

A. Van Niekerk and S. Vosper. Towards a more "scale-aware" orographic gravity wave drag parametrization: Description and initial testing. *Quart. J. Roy. Meteorol. Soc.*, 147:3243–3262, 2021. doi: 10.1002/qj.4126.

E. Vignon, G. Picard, C. Durán-Alarcón, S. Alexander, H. Gallée, and A. Berne. Gravity Wave Excitation during the Coastal Transition of an Extreme Katabatic Flow in Antarctica. *J. Atmos. Sci.*, 77:1295–1312, April 2020. doi: 10.1175/JAS-D-19-0264.1.

R. Vincent and M. Alexander. Gravity waves in the tropical lower stratosphere: An observational study of seasonal and interannual variability. *J. Geophys. Res. Atmos.*, 105(D14):17971–17982, JUL 27 2000. doi: 10.1029/2000JD900196.

T. von Clarmann, C. De Clercq, M. Ridolfi, M. Höpfner, and J.-C. Lambert. The horizontal resolution of MIPAS. *Atmos. Meas. Tech.*, 2:47–54, 2009. doi: 10.5194/amt-2-47-2009.

J. M. Wallace and P. V. Hobbs. *Atmospheric Science: An introductory survey*. International Geophysics Series. Academic Press Limited, 2006. 2nd edition.

S. Watanabe, K. Sato, and M. Takahashi. A general circulation model study of the orographic gravity waves over antarctica excited by katabatic winds. *J. Geophys. Res.*, 111, 2006. doi: 10.1029/2005JD006851.

A. Wegener. Studien über luftwogen. *Beitr. Physik Freien Atmos.*, 4:23–25, 1906.

N. Wildmann, R. Eckert, A. Dörnbrack, S. Gisinger, M. Rapp, K. Ohlmann, and A. van Niekerk. In situ measurements of wind and turbulence by a motor glider in the andes. *Journal of Atmospheric and Oceanic Technology*, 38(4):921 – 935, 2021. doi: 10.1175/JTECH-D-20-0137.1.

W. Woiwode, A. Dörnbrack, M. Bramberger, F. Friedl-Vallon, F. Haenel, M. Höpfner, S. Johansson, E. Kretschmer, I. Krisch, T. Latzko, H. Oelhaf, J. Orphal, P. Preusse, B.-M. Sinnhuber, and J. Ungermann. Mesoscale fine structure of a tropopause fold over mountains. *Atmos. Chem. Phys. Discuss.*, 18:15643–15667, 2018. doi: 10.5194/acp-18-15643-2018.

J. Xie, M. Zhang, Z. Xie, H. Liu, Z. Chai, J. He, and H. Zhang. An Orographic-Drag Parametrization Scheme Including Orographic Anisotropy for All Flow Directions. *J. Adv. Model. Earth Syst.*, 12, 2019. doi: 10.1029/2019MS001921.

J. Xie, M. Zhang, Z. Xie, H. Liu, Z. Chai, J. He, and H. Zhang. An orographic-drag parametrization scheme including orographic anisotropy for all flow directions. *Journal of Advances in Modeling Earth Systems*, 12, 2020. doi: 10.1029/2019MS001921.

Y. Yu and X. Cai. Structure and dynamics of katabatic flow jumps: Idealised simulations. *Bound.-Layer Meteorol.*, 118:527–555, 2006. doi: 10.1007/s10546-005-6433-5.

X. Zhou, J. Holton, and G. Mullendore. Forcing of secondary waves by breaking of gravity waves in the mesosphere. *J. Geophys. Res.*, 107(D7):4058, 2002. doi: 10.1029/2001JD001204.

X. Zhu. Radiative damping revisited - Parametrization of damping rate in the middle atmosphere. *J. Atmos. Sci.*, 50(17):3008–3021, SEP 1 1993. doi: 10.1175/1520-0469(1993)050<3008:RDRPOD>2.0.CO;2.

C. Zülicke and D. Peters. Simulation of inertia-gravity waves in a poleward-breaking Rossby wave. *J. Atmos. Sci.*, 63(12):3253–3276, DEC 2006. doi: 10.1175/JAS3805.1.